SINGLE ION TRAPPING IN A BUFFER GAS AND LIQUID XE ENERGY RESOLUTION STUDIES FOR THE EXO EXPERIMENT

A DISSERTATION
SUBMITTED TO THE DEPARTMENT OF PHYSICS
AND THE COMMITTEE ON GRADUATE STUDIES
OF STANFORD UNIVERSITY
IN PARTIAL FULFILLMENT OF THE REQUIREMENTS
FOR THE DEGREE OF
DOCTOR OF PHILOSOPHY

Jesse Wodin
February 2007

I certify that I have read this dissertation and that, in my opinion, it is fully adequate in scope and quality as a dissertation for the degree of Doctor of Philosophy.

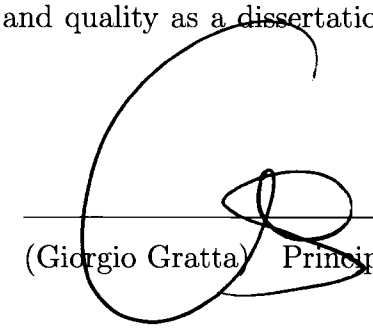

(Giorgio Gratta) Principal Adviser

I certify that I have read this dissertation and that, in my opinion, it is fully adequate in scope and quality as a dissertation for the degree of Doctor of Philosophy.

Sarah E Church

(Sarah Church)

I certify that I have read this dissertation and that, in my opinion, it is fully adequate in scope and quality as a dissertation for the degree of Doctor of Philosophy.

Ralph DeVoe

(Ralph DeVoe)

Approved for the University Committee on Graduate Studies.

Abstract

Recent neutrino oscillation results provide experimental proof that neutrinos are massive particles. These measurements, however, reveal information about neutrino mass differences, as opposed to the absolute mass values themselves. Observation of a rare nuclear transition called neutrinoless double beta decay ($0\nu\beta\beta$) would constitute an absolute neutrino mass measurement. This decay requires that neutrinos are massive Majorana particles, and that lepton number conservation is violated. Observation of this decay will undoubtedly reveal physics beyond the current Standard Model of particle physics. Current limits on the half-life of $0\nu\beta\beta$ are $> 10^{25}$ yr, providing a formidable experimental challenge. The Enriched Xenon Observatory (EXO) is a double beta decay experiment poised to improve upon this limit, using ^{136}Xe as both a source and detector of this decay. $0\nu\beta\beta$ of ^{136}Xe produces a detectable energy deposition, in addition to a single $^{136}Ba^{++}$ decay daughter which can be used to tag this rare process. This thesis deals with the details of energy deposition in liquid Xenon (LXe), as well as the first observation of single Ba ions in a high pressure buffer-gas filled RF Paul trap.

Acknowledgements

Thanks to everyone who kept my mind from melting into a pile of goo. To my M.I.T. friends, who have always encouraged me, and never judged. To everyone in lab, who pretend to ask me questions about stuff so that I can feel good about myself. To my former and current professors, who seem to see something worthwhile in me, besides to cheap labor. And finally, but most importantly, to my parents, sister, girlfriend, cat, and dogs, who are the center of my life.

Contents

List of Tables

List of Figures

Chapter 1

Introduction

Results of recent pioneering neutrino oscillation experiments, such as SuperK [8], SNO [9], and KamLAND [10], provide evidence that neutrinos are massive particles. The Standard Model (SM) of particle physics had assumed, until this discovery, that neutrinos were massless particles. This discovery therefore offers new possibilities to explore physics beyond the SM. In particular a measurement of the absolute neutrino mass, which cannot be measured by oscillation experiments, will have profound implications for fields such as particle physics, cosmology, astrophysics, and string theory.

One possible method of measuring the neutrino mass is by observation of a rare, as of yet unseen, second-order electroweak process called neutrinoless double beta decay ($0\nu\beta\beta$). The Enriched Xenon Observatory for neutrinoless double beta decay (EXO) is designed to search for this decay in ^{136}Xe. In the standard version of this process (two neutrino double beta decay, or $2\nu\beta\beta$), a ^{136}Xe decays to a $^{136}Ba^{++}$, emitting two electrons and two electron anti-neutrinos. This process has been observed in various nuclei, but does not allow for a measurement of absolute neutrino mass. The $0\nu\beta\beta$ process emits two electrons and a neutrino which is reabsorbed during the decay.

Current limits on the half-life of this decay, $T_{1/2}^{0\nu\beta\beta} > 1.6 \times 10^{25}$ yr, yield neutrino mass limits < 0.35 eV. Improving on this value requires substantially larger quantities of the target isotope, in addition to new techniques to further decrease radioactive backgrounds, which currently limit the experimental sensitivity to $0\nu\beta\beta$. Enhancing

the ability to detect these decays, by maximizing the experimental energy resolution, is one key goal. In addition, tagging the decay daughter of $0\nu\beta\beta$ provides a means of eliminating all radioactive backgrounds [11]. $0\nu\beta\beta$ of ^{136}Xe, in particular, provides a unique opportunity in this sense, as the resulting $^{136}Ba^{+}$ is observable via resonance fluorescence. The trapping and observation of single $^{136}Ba^{+}$ is described in the first half of this thesis. The second half of this thesis studies energy resolution enhancement in a liquid Xe detector.

In ch. 2, the current status of neutrino mass measurements is briefly reviewed. The physics of $0\nu\beta\beta$ is introduced, along with a basic description of the EXO-200 and second generation EXO experiments. The EXO-200 experiment is under construction as of the writing of this thesis. In ch. 3-4, the physics of resonance fluorescence and trapping of a single $^{136}Ba^{+}$ are discussed. The theory and measurements presented here, as well as in [3], lay the foundation for tagging of the decay daughter of ^{136}Xe in the second generation EXO experiment. A single $^{136}Ba^{+}$ is trapped and observed in a buffer-gas filled RF Paul trap, for the first time to the author's knowledge. In ch. 5-6, the detection of energy deposition in a liquid Xe detector is studied, by simultaneously collecting ionization and scintillation signals produced by a ^{207}Bi β^{-}/γ source. This leads to an enhancement in the energy resolution [12], with respect to previously published results, and plays an important role in the design of both EXO-200 and the second generation EXO experiment.

Chapter 2

Massive neutrinos

The recent observation of flavor conversion of solar, atmospheric, and reactor neutrinos naturally implies the existence of three massive neutrinos, labeled m_1, m_2, m_3 [9, 8, 10, 13]. These mass eigenstates are related to the weak eigenstates, m_e, m_μ, m_τ, via a mixing matrix, U_{ij}, similar to to the CKM mixing matrix for quarks. In particular, for the electron neutrino ν_e,

$$\nu_e = \sum_j^N U_{ej} m_j \tag{2.1}$$

where N is the number of light neutrinos. The Standard Model of particle physics (SM) does not require neutrinos to be massive particles, implying that mixing is explained by new physics beyond the SM.

Measurements of flavor oscillations reveals information about neutrino mass differences, $\Delta m_{ij} = m_i^2 - m_j^2$, though much less is known about the absolute neutrino masses themselves. The measured mass splitting primarily responsible for atmospheric oscillations $|\Delta m_{32}^2| = (2.4 \pm 0.3) \times 10^{-3}$ eV^2 implies a lower limit on the heaviest neutrino mass, $m_h > 0.04$ eV [13]. Whether or not this mass is m_1, m_2, or m_3 depends on the hierarchy of these three mass states. The current experimentally

allowed hierarchy models are

$$\text{normal} : \quad m_1 \sim m_2 \ll m_3 \tag{2.2}$$

$$\text{inverted} : \quad m_3 \ll m_1 \sim m_2 \tag{2.3}$$

$$\text{degenerate} : \quad m_1 \sim m_2 \sim m_3 \tag{2.4}$$

Given each of these models, other limits can be set from solar and reactor experiments, such as SNO, Super-Kamiokande and KamLand [2].

Non-oscillation experiments, such as β-decay, cosmological observations, and neutrinoless double beta decay ($0\nu\beta\beta$) yield complementary information in the neutrino sector. β-decay is the simplest method of making an absolute neutrino mass measurement. The Mainz experiment [14] measures the β-decay energy spectrum in the vicinity of the tritium β-decay endpoint

$$^3\mathrm{H} \rightarrow {}^3\mathrm{He} + e^- + \bar{\nu}_e \tag{2.5}$$

setting a limit $m_{\nu_e} < 2.0 - 2.2$ eV [13]. The KATRIN experiment plans to improve on this kinematic method, with a planned sensitivity of ~ 0.2 eV [15]. Cosmological observations, such as WMAP, put a bound on the sum of neutrino masses $\sum_{i=1}^{3} m_i <$ 0.17 eV (95% C.L.) [16]. Combining cosmological and oscillation results, at least one neutrino mass should be in the range $m_\nu = (0.04 - 0.10)$ eV. The cosmological limit, in addition, disfavors a strongly degenerate mass spectrum [13].

$0\nu\beta\beta$ has the potential to probe mass limits in the meV range, provided neutrinos are Majorana particles, and lepton number conservation is violated. Currently, the best limit on the Majorana mass due to $0\nu\beta\beta$ is $\langle m_{\beta\beta} \rangle < (0.35 - 0.50)$ eV, as measured by the Heidelberg-Moscow experiment using ^{76}Ge as a source material [17]. In this case, $\langle m_{\beta\beta} \rangle$ is the effective Majorana mass, described in §2.1. A portion of the Heidelberg-Moscow collaboration claims a positive signal at $\langle m_{\beta\beta} \rangle \sim 0.4$ eV. If this positive signal is confirmed, and $0\nu\beta\beta$ is due to the exchange of light Majorana neutrinos, the neutrino mass spectrum is strongly degenerate [18].

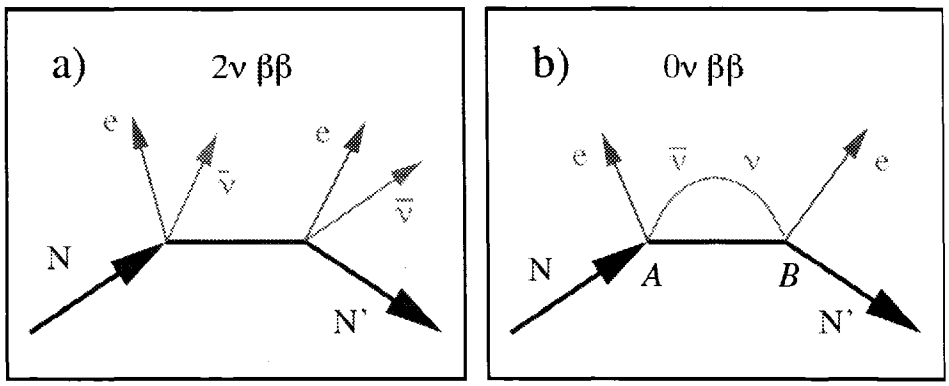

Figure 2.1: Feynman diagrams for (a) (standard) two-neutrino double beta decay ($2\nu\beta\beta$) and (b) neutrinoless double beta decay ($0\nu\beta\beta$). N and N' are the initial and final nuclei.

2.1 Double beta decay

Two neutrino double beta decay ($2\nu\beta\beta$) is a standard second-order electroweak process, whereby a nucleus with charge Z and mass number A decays to a nucleus with charge $Z+2$ and mass A,

$$(Z, A) \rightarrow (Z+2, A) + e_1^- + e_2^- + \bar{\nu}_{e1} + \bar{\nu}_{e2} \tag{2.6}$$

where both Z and A are even. In this process, two neutrons decay to two protons, two electrons, and two electron antineutrinos, shown schematically in fig. 2.1a. The total energy difference (usu. just mass) between the initial and final nuclei is called the Q-value. In $2\nu\beta\beta$, this energy is distributed among the emitted electrons, neutrinos, and nuclear recoil of the daughter nucleus. This process occurs in various "even-even" nuclei, with a rate $\sim (G_F \cos\theta_C)^4$, where G_F is the Fermi coupling constant and θ_C is the Cabbibo angle. This rate would be dwarfed by the single β-decay rate, if it were not for a peculiarity in the nuclear mass function of certain even-even nuclei. This is shown for the case of ^{136}Xe in fig. 2.2 where single β-decay to ^{136}Cs is energetically disfavored over $2\nu\beta\beta$ to ^{136}Ba^{++}. This is a common situation, though only a few nuclei exist with a decay endpoint large enough (Q >2 MeV) such that the decay occurs with an experimentally observable rate. $2\nu\beta\beta$ has been observed in

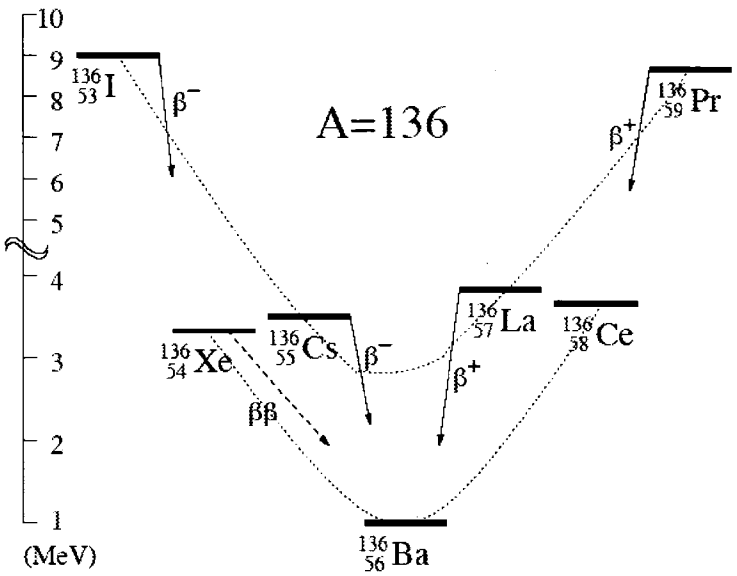

Figure 2.2: Nuclei with $A = 136$. Parabolae connecting "odd-odd" and "even-even" nuclei are shown. Single β-decay of ^{136}Xe to ^{136}Cs is energetically forbidden.

10 nuclei, and is useful in verifying second-order nuclear matrix element calculations. This process is observed experimentally via the sum electron energy spectrum (K_e in fig. 2.3 at 5 % detector energy resolution). The electron energy spectrum of $2\nu\beta\beta$ is continuous, as the neutrino can be emitted with a kinetic energy between 0 and Q. Current experimentally measured $2\nu\beta\beta$ half-lives are listed in table 2.1 [1].

Neutrinoless double beta decay,

$$(Z, A) \rightarrow (Z + 2, A) + e_1^- + e_2^- \tag{2.7}$$

violates lepton number conservation, and is therefore forbidden in the standard electroweak theory. The Feynman diagram for this process is shown in fig. 2.1b. $0\nu\beta\beta$ requires that neutrinos are both massive and equivalent to their own antiparticles (Majorana, as opposed to Dirac neutinos), since the right-handed antineutrino emitted at vertex A in fig. 2.1b must become a left-handed neutrino to be absorbed at vertex B. This assumes standard electroweak interactions at both vertices, requiring left-handed neutrino currents. In this case, the sum electron energy spectrum is a

Isotope	$T_{1/2}^{2\nu\beta\beta}$ [yr]
^{48}Ca	$(4.2 \pm 1.2) \times 10^{19}$
^{76}Ge	$(1.3 \pm 0.1) \times 10^{21}$
^{82}Se	$(9.2 \pm 1.0) \times 10^{19}$
^{96}Zr	$1.4^{+3.5}_{-0.5} \times 10^{19}$
^{100}Mo	$(8.0 \pm 0.6) \times 10^{18}$
^{116}Cd	$(3.2 \pm 0.3) \times 10^{19}$
^{128}Te	$(7.2 \pm 0.3) \times 10^{24}$
^{130}Te	$(2.7 \pm 0.1) \times 10^{21}$
^{136}Xe	$> 8.1 \times 10^{20}$ (90% CL)
^{150}Nd	$7.0^{+11.8}_{-0.3} \times 10^{18}$
^{238}U	$(2.0 \pm 0.6) \times 10^{21}$

Table 2.1: Summary of experimentally measured $2\nu\beta\beta$ half lives [1].

delta-function, centered at Q. The $0\nu\beta\beta$ sum electron spectrum is shown magnified and convolved with a 5 % detector energy resolution in fig. 2.3.

If $0\nu\beta\beta$ occurs, a superposition of the three mass eigenstates participate in the decay. The effective Majorana mass, $\langle m_{\beta\beta} \rangle$, is defined as

$$\langle m_{\beta\beta} \rangle = \left| \sum_j U_{ej}^2 m_j \right| = \left| \sum_j \left| U_{ej}^2 \right| e^{\alpha_j} m_j \right|^2 \tag{2.8}$$

The matrix elements U_{ej} (see eqn. 2.1) contain Majorana phases, α_j, which are unknown. If CP is conserved, $\alpha_j = k\pi$ (where k is an integer) but generally any values of α_j are allowed. Since the effective mass contains the term $|U_{ej}^2|$ (as opposed to $|U_{ej}|^2$), these phases can cause cancellations in the sum, leading to an uncertainty in the neutrino mass.

The effective Majorana neutrino mass is related to the half-life of the decay, $T_{1/2}^{0\nu\beta\beta}$, via

$$\langle m_{\beta\beta} \rangle = \left(T_{1/2}^{0\nu\beta\beta} G^{0\nu\beta\beta}(Q, Z) \left| M_{GT}^{0\nu\beta\beta} - \frac{g_V^2}{g_A^2} M_F^{0\nu\beta\beta} \right|^2 \right)^{-1} \tag{2.9}$$

where $G^{0\nu\beta\beta}(Q, Z)$ is a phase-space factor depending on the endpoint energy Q and nuclear charge Z, $M_{GT}^{0\nu\beta\beta}$ and $M_F^{0\nu\beta\beta}$ are the Gamow-Teller and Fermi matrix elements,

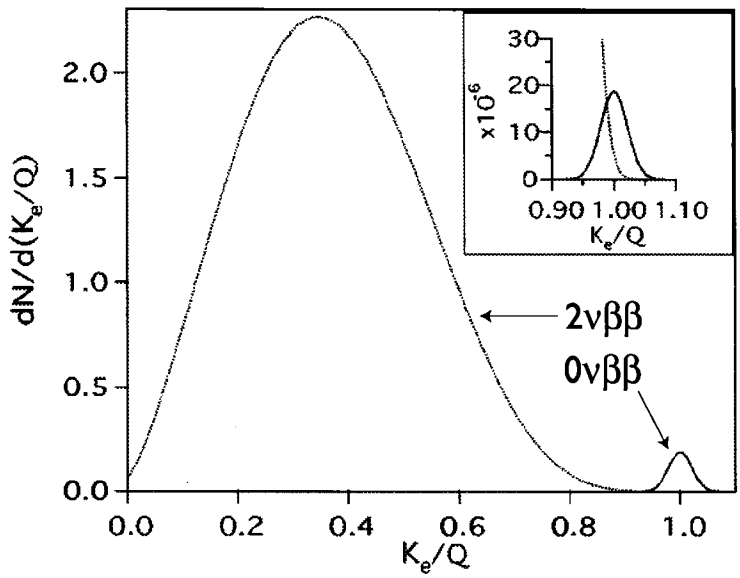

Figure 2.3: Spectra of the sum of electron energies, K_e, from $2\nu\beta\beta$ (dotted) and $0\nu\beta\beta$ (solid) decay, normalized by the decay endpoint Q [1]. The $2\nu\beta\beta$ spectrum is normalized to 1, and the $0\nu\beta\beta$ spectrum is normalized to 10^{-2} (10^{-6} inset). All spectra are convolved with an energy resolution of 5 %.

and $g_{V,A}$ are the vector and axial-vector coupling constants [1]. Current experimental limits on $T_{1/2}^{0\nu\beta\beta}$ are listed in table 2.2. The combination of β-decay, cosmological observation, oscillation, and $0\nu\beta\beta$ results are required to elucidate the nature of these phases [1].

Whereas the effective Majorana mass $\langle m_{\beta\beta}\rangle$ depends on (currently) unknown Majorana phases, the lower and upper bounds on this mass, $\langle m_{\beta\beta}\rangle_{\min}$ and $\langle m_{\beta\beta}\rangle_{\max}$ are determined by absolute values of the mixing angles [19],

$$\langle m_{\beta\beta}\rangle_{\max} = \sum_j |U_{ej}|^2 m_j \tag{2.10}$$

$$\langle m_{\beta\beta}\rangle_{\min} = \max\left[\left(2\,|U_{ej}|^2 m_j - \langle m_{\beta\beta}\rangle_{\max}\right), 0\right] \tag{2.11}$$

Therefore, if $0\nu\beta\beta$ is observed and the value of $\langle m_{\beta\beta}\rangle$ is measured, and at the same time the mixing angles U_{ej} and mass-squared differences Δm_{ij}^2 known from oscillation experiments, a range of absolute neutrino masses can be deduced [1]. This range is

Isotope	$T_{1/2}^{0\nu\beta\beta}$ [$\times 10^{21}$ yr]	Experiment
^{130}Te	>1800	CUORICINO
^{100}Mo	>460	NEMO-3
^{82}Se	>100	NEMO-3
^{76}Ge	11900^{+29900}_{-5000}	Heidelberg-Moscow
^{48}Ca	>14	ELEGANT VI
^{116}Cd	>170	Solotvina
^{76}Ge	>15700	Heidelberg-Moscow
^{134}Xe	>58	DAMA
^{136}Xe	>1200	DAMA
^{160}Gd	>1.3	Solotvina
^{96}Zr	>1.0	NEMO-2

Table 2.2: Summary of experimental limits on $0\nu\beta\beta$ decay half lives [2]. Results are arranged according to publication data. All limits are 90 % CL.

illustrated in fig. 2.4, where the $\langle m_{\beta\beta}\rangle$ is plotted against the lightest neutrino mass. In this figure, $N = 3$ massive interacting neutrinos, large solar neutrino mixing (LMA oscillation solution), and maximal atmospheric neutrinos mixing between ν_τ and ν_μ are assumed. Evidently, $0\nu\beta\beta$ experiments with a sensitivity in the 10 meV range are required to make a strong statement about the neutrino hierarchy question.

2.2 Experimental considerations for $0\nu\beta\beta$

Advances in low background experimental techniques over the last thirty years have allowed for the observation of the $2\nu\beta\beta$ decay mode in various nuclei, as listed in table 2.1. $0\nu\beta\beta$ is the next challenge, identified by the sum electron energy spectrum at the decay endpoint (see fig. 2.3). Experimentally, this search is reduced to a counting experiment, where the goal is to maximize the $0\nu\beta\beta$ rate while miminizing all background rates ($2\nu\beta\beta$ decay, radioactive impurities, etc.) that can mimic a $0\nu\beta\beta$ signal . Given the current limits on the $0\nu\beta\beta$ half lives (see table 2.2), the requirements to push the experimental sensitivity to $\langle m_{\beta\beta}\rangle \sim 50$ meV, as indicated by oscillation results, are challenging.

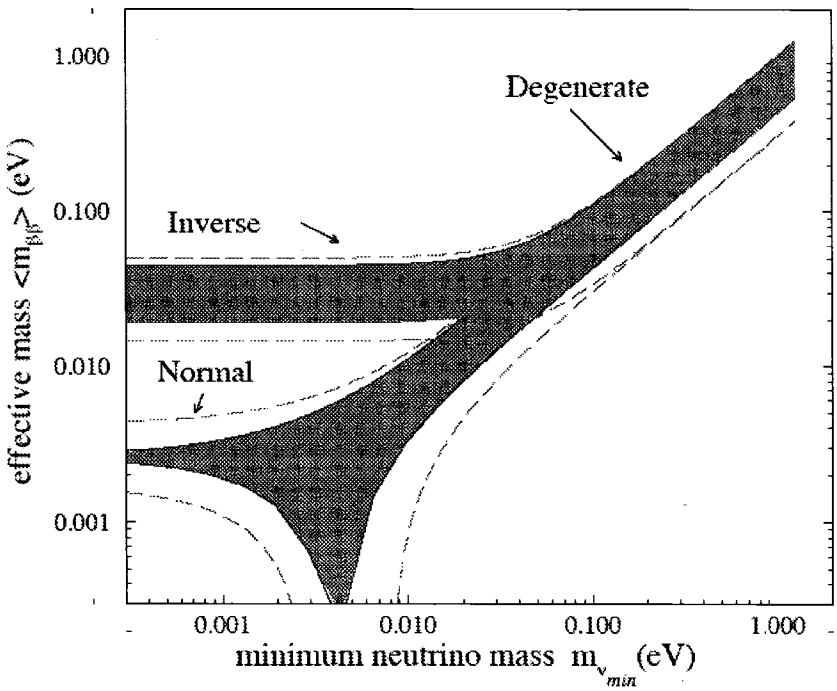

Figure 2.4: Effective mass $\langle m_{\beta\beta} \rangle$ as a function of the smallest neutrino mass, m_{min}, adapted from [3]. The solid region indicates the range of allowed $0\nu\beta\beta$ masses, related to the unknown Majorana phases, while the dashed lines indicate the 1σ errors from oscillation results.

The effective Majorana mass sensitivity depends on experimental parameters as

$$\langle m_{\beta\beta}\rangle = (2.50\times10^{-8}\text{eV})\left[\frac{W}{fx\epsilon G^{0\nu}|M^{0\nu}|^2}\right]^{1/2}\left[\frac{b\Delta E}{MT}\right]^{1/4} \quad (2.12)$$

$$\langle m_{\beta\beta}\rangle = (2.67\times10^{-8}\text{eV})\left[\frac{W}{fx\epsilon G^{0\nu}|M^{0\nu}|^2}\right]^{1/2}\times\frac{1}{\sqrt{MT}} \quad (2.13)$$

where W is the molecular weight of the source material, f is the isotopic abundance, x is the number of double beta decay candidate atoms per molecule, ϵ is the detector efficiency, b is the number of background events per (kg·yr·keV), ΔE is the energy window for $0\nu\beta\beta$ decay in keV, M is the mass of isotope in kg, T is the live time of the experiment in yr., and $|M^{0\nu}|$ represents the $0\nu\beta\beta$ nuclear matrix elements [1]. The first case is for a background-rate limited experiment, whereas the second is for a background-free experiment.

In the first case, the $\langle m_{\beta\beta}\rangle$ sensitivity is determined by the statistical fluctuations in the background rate, where a simple Poisson scaling with the detector mass and exposure time is assumed. In this case, $\langle m_{\beta\beta}\rangle \propto \sqrt{T_{1/2}^{0\nu\beta\beta}} \propto (MT)^{-1/4}$. This is the case for an experiment with trace radioactive impurities present in the source material and detector housing, for example. The count rate due to these impurities will increase linearly with time and source mass. $\langle m_{\beta\beta}\rangle$ scales with the square root of the half-life, and hence the fourth root of the product MT.

If, on the other hand, backgrounds due to radioactive impurities are eliminated, the sensitivity is purely a function of the statistical fluctuations of the $0\nu\beta\beta$ count rate itself. In this case, $\langle m_{\beta\beta}\rangle \propto (MT)^{-1/2}$. It is clear that background rate reduction is one of the primary design criteria for all next-generation $0\nu\beta\beta$ experiments. This requires a high degree of source material radio-purity, low-background handling techniques of all materials close to the detector, special material selection and shielding throughout construction (minimization of cosmogenic activation), local detector shielding during data-taking (e.g. a lead shield between the detector and all other components), and a deep experimental site (cosmic-ray shielding), to name just a few considerations.

A few criteria other than background reduction are obvious from eqns. 2.12-2.13

[1]. A large amount of source material is needed; approximately 1 ton is required to reach $\langle m_{\beta\beta} \rangle \sim 50$ meV, whereas current experiments use ~ 10 kg. High detector energy resolution is essential; this is required to be able to separate the $0\nu\beta\beta$ peak from the $2\nu\beta\beta$ continuum (see fig. 2.3), or any other radioactive backgrounds present near the endpoint. An isotope with a large Q-value and matrix element is preferable; this improves the $\langle m_{\beta\beta} \rangle$ sensitivity for a given half life. Finally, the magnitude of the $2\nu\beta\beta$ rate must be considered; certain elements (e.g. ^{100}Mo) have a high $2\nu\beta\beta$ rate compared to the expected $0\nu\beta\beta$ rate, which can bleed counts into the energy window around the Q-value.

Satisfying all of these criteria reduces backgrounds, but cannot eliminate them entirely. Two isotopes in particular provide a means of eliminating radioactive backgrounds. First, $0\nu\beta\beta$ of ^{150}Nd is accompanied by a 30 keV X-ray, which can be detected in coincidence with the two electrons emitted. Second, $0\nu\beta\beta$ of ^{136}Xe produces $^{136}Ba^{++}$ (which becomes $^{136}Ba^{+}$ by capturing an electron from the LXe conduction band) which can be identified via resonance fluorescence immediately after the decay. The EXO-200 and EXO experiments, described below, look for $0\nu\beta\beta$ using ^{136}Xe.

2.3 EXO-200

The first phase of the Enriched Xe Observatory (EXO-200) is a double beta decay experiment currently under construction, employing 200 kg of liquid Xe (LXe), isotopically enriched to 80 % ^{136}Xe. Xe is an ideal material for a large scale double beta decay experiment for the following reasons

- it is one of the easiest isotopes to enrich
- it serves as both the source and detector, with good energy resolution
- energy deposition creates electrons and scintillation photons, which can be used for event localization and energy determination
- it has no long lived isotopes to activate
- it can be continuously purified while the experiment is running

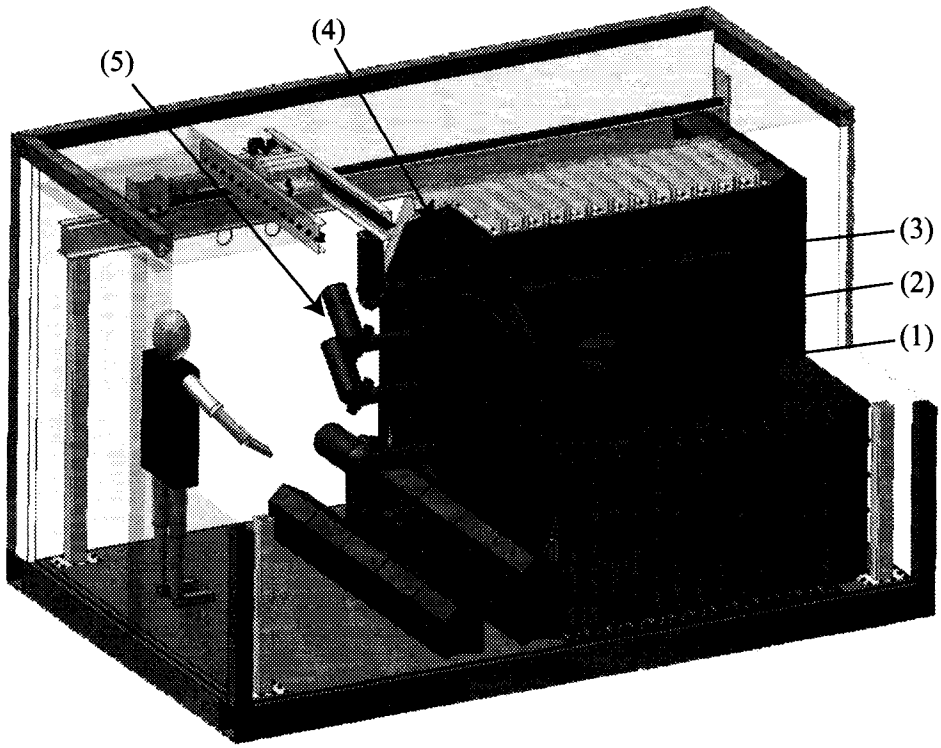

Figure 2.5: Schematic of the EXO-200 detector assembly. (1) Ultra-low activity copper LXe chamber. (2) HFE volume. (3) Double-walled, vacuum insulated cryostat. (4) Pb shielding. (5) Plumbing/instrumentation feedthroughs.

- it produces a final state, $^{136}Ba^{++}$, which can be identified via optical spectroscopy after conversion to $^{136}Ba^{+}$

The EXO-200 detector is shown in fig. 2.5. The LXe will be housed in a low-background copper cryostat (1), shielded by a low-background, high-density heat transfer fluid (2) used to keep the LXe at a nominal temperature of 160 K. This fluid also serves as radiation shielding, from any radioactive contaminates in the outer layers of the detector. The heat transfer fluid is in turn housed in a double-walled, vacuum insulated cryostat (3). Refrigerators (not shown), circulate 160 K refrigerant through heat exchangers, which are welded onto the outside of the cryostat. The cryostat is housed in a 25 cm thick, low-background lead shielding structure (4), again used for radiation shielding. A 6 ft. schematic person is shown in the figure for reference. This entire apparatus is housed in a class 100 clean room, which will be installed

at a the Waste Isolation Pilot Plant (WIPP), under $\sim$ 1700 meters water-equivalent of rock. This serves as the primary shielding against cosmic rays. All materials used in the detector construction are put through a low-background approval process, involving neutron activation at the MIT nuclear reactor, and subsequent Monte-Carlo studies.

The natural abundance of ^{136}Xe is < 10 %, requiring substantial enrichment. All next generation $0\nu\beta\beta$ experiments will require enrichment, which will be the largest single cost item in all cases. Hence, the ease and cost of enrichment should be considered in a $0\nu\beta\beta$ experiment. ^{136}Xe enrichment is particularly suited to ultra-centrifuge separation, and is a relatively simple process for two reasons. First, Xe is an inert gas at the standard operating temperatures and pressures of ultra-centrifuges. Second, ^{136}Xe is the heaviest Xe isotope, allowing the enrichment to be done in a single pass through cascaded centrifuges. In contrast, ^{76}Ge and ^{130}Te require complex chemistry during enrichment.

The LXe itself acts as both the source of $0\nu\beta\beta$, and the detector, as shown schematically in fig. 2.6. A $0\nu\beta\beta$ decay (item (1) in fig. 2.6) produces a cloud of ionization electrons (2) in the LXe. Recombination of these electrons with Xe ions produces scintillation (3), which is collected by avalanche photodiodes (6). A drift field is set up by grids (4) and (5), which drifts electrons across the LXe volume for collection. The energy and spatial position of the event is determined by pulse height/shape/timing analysis on the electron and scintillation photon signals, as described in ch. 6-7 of this thesis. The physics of the ionization and scintillation processes in LXe is therefore central to measuring $0\nu\beta\beta$ in this detector, and is the subject of the second half of this thesis.

2.4 EXO

EXO is the second generation experiment, proposed to follow EXO-200. EXO will employ 1-10 tons of enriched ^{136}Xe to search for $0\nu\beta\beta$. The general principles described in §2.3 are the same, with one exception: in EXO, the Ba daughter (item (1) in fig. 2.6) will be spectroscopically identified, immediately after a $0\nu\beta\beta$ event has

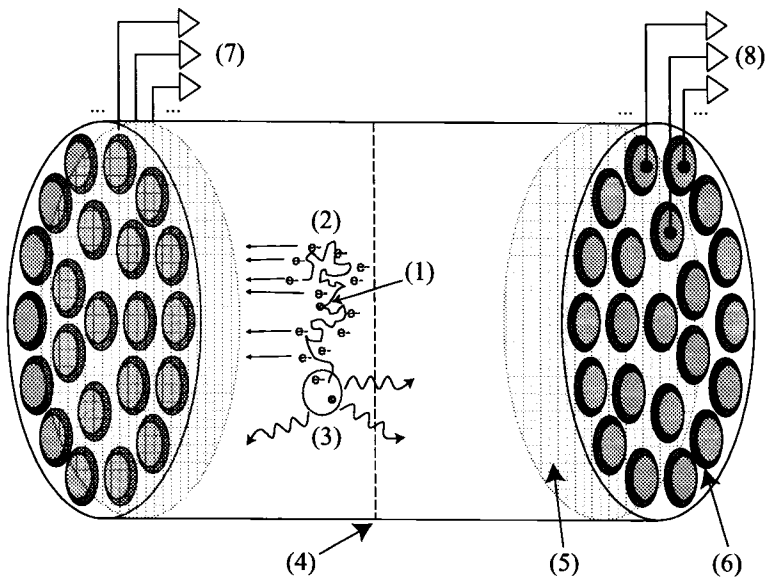

Figure 2.6: Event detection in EXO-200. (1) A $0\nu\beta\beta$ decay event, producing ionization electrons, (2), and scintillation photons (3). (4) Center grid (-75 kV). (5) Ionization collection wires. (6) APD plane for scintillation collection. (7) Ionization readout electronics. (8) Scintillation readout electronics.

occurred. This requires knowledge of the location of the $0\nu\beta\beta$, but will eliminate all radioactive backgrounds that do not produce a Ba ion in the detector. The $2\nu\beta\beta$ mode, in this case, is still a possible background.

Given the electronic band structure of LXe, the $^{136}Ba^{++}$ should capture an electron, and become $^{136}Ba^{+}$. The lowest lying electronic levels of $^{136}Ba^{+}$ are then easily accessible via resonance fluorescence (using 650 nm and 493 nm lasers) as described in ch. 3. The identification of $^{136}Ba^{+}$, resulting from $0\nu\beta\beta$, can be implemented in multiple ways. One possibility is to excite the $^{136}Ba^{+}$ in the LXe with resonant lasers, and observe the fluorescence of the single Ba ion. It is possible, in this case, that the interaction between the ion and the LXe will broaden the ion's resonances to the point where it cannot be detected reliably. This method is currently under development. Another possibility is to extract the ion with a probe, and inject it into an ion trap (a separate entity from the detector shown in fig. 2.6) for spectroscopic observation. The ion trap must be able to accept ions injected from an external source (the probe) and trap them with high efficiency. In addition, a single $^{136}Ba^{+}$ ion must

be observable in the trap, via resonance fluorescence. Various probes, used to extract a single $^{136}Ba^{+}$ from the detector, are currently under development. Details of these probes are out of the scope of this work. However, one promising design utilizes a small amount of Xe ice as the tip of the probe. This method, in particular, requires that an ion trap function in the presence of a small amount of Xe. Ch. 3-4 present the theory and construction of a single-ion trap, designed to satisfy these criteria. Single $^{136}Ba^{+}$ ions are trapped and observed with high signal to noise in the presence of He, Ar, and He/Xe mixtures as buffer gases.

Chapter 3

Resonance fluorescence

Laser fields, resonant with the $6S_{1/2} \rightarrow 6P_{1/2}$ and $6P_{1/2} \rightarrow 5D_{3/2}$ transitions of a Ba^+ (fig. 3.1), are used to induce fluorescence at 493 nm and 650 nm. The fluorescence intensity is proportional to the number of ions under interrogation, for low ion number. This allows for the detection of individual Ba ions via quantization of the fluorescence rate. This technique is presented here as a means of spectroscopically tagging the $^{136}Ba^+$ produced by the $0\nu\beta\beta$ of ^{136}Xe.

The interaction of an ion with a laser field is described using the density matrix formulation, leading to the optical Bloch equations. These equations are solved in the steady state case, and the fluorescence spectra are derived. The effects of power broadening and ion motion due to collisions with a buffer gas on the fluorescence spectrum are also discussed.

3.1 Resonance fluorescence of Ba^+

The lowest lying Ba^+ electronic levels are shown in fig. 3.1. The experiments presented in this work involve a single trapped Ba^+ in a buffer gas, with a negligible external magnetic field. Therefore, any optical pumping between magnetic sublevels is undone by gas collsions. For this reason, the density matrix formulation described here only involves the eigenstates of J^2, assuming that the eigenstates of J_z are degenerate. This analysis is in principle easily extended to an n-level system where

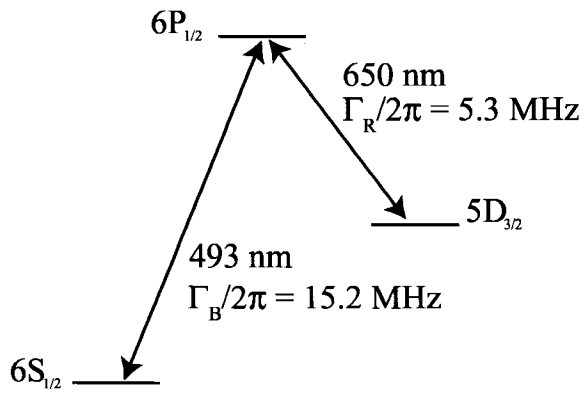

Figure 3.1: Ba^+ level diagram. Only the lowest lying levels used in this experiment are shown.

the J_z eigenstates are non-degenerate [20], though the number of coupled differential equations to be solved increases as n^2. The theory of resonance fluorescence presented here is taken from Corney [20].

3.1.1 Density matrix formalism

The quantum mechanical state of the ion at time t is a linear superposition of eigenstates with time-dependent coefficients

$$|\Psi(t)\rangle = \sum_j a_j(t)\,|j\rangle \tag{3.1}$$

where the index $j = 1, 2, 3$ and the following identification is made

$$|1\rangle = |6S_{1/2}\rangle \tag{3.2}$$

$$|2\rangle = |6P_{1/2}\rangle \tag{3.3}$$

$$|3\rangle = |5D_{3/2}\rangle \tag{3.4}$$

The expectation value of an operator $\mathcal{M}$ is then

$$\langle\Psi(t)|\,\mathcal{M}\,|\Psi(t)\rangle = \sum_{j,k} \rho_{jk}\,\langle k|\,\mathcal{M}\,|j\rangle \tag{3.5}$$

where

$$\rho_{jk} = a_j(t)a_k(t)^* = \langle j|\,\rho\,|k\rangle \tag{3.6}$$

The state of the atomic system as a function of time is therefore encoded in the coefficients ρ_{jk}, which are the elements of the density matrix ρ. The elements ρ_{jj} can be interpreted as the time dependent probability that an atom is in a state $|j\rangle$. The off-diagonal elements ρ_{jk}, where $j \neq k$, are the probabilities of the atom being in a linear superposition of states $|j\rangle$ and $|k\rangle$. These are called *coherences.*

Two important additional properties of the density matrix are conservation of probability,

$$\text{Tr } \rho = 1 \tag{3.7}$$

and Hermiticity

$$\rho_{ij} = \rho_{ji}^* \tag{3.8}$$

3.1.2 The Liouville equation

The time derivative of the density matrix, from eqn. 3.6, is evidently

$$\frac{\partial \rho_{jk}}{\partial t} = \frac{\partial a_j}{\partial t}a_k^* + a_j\frac{\partial a_k^*}{\partial t} \tag{3.9}$$

whereas the development of the atomic wavefunction $|\Psi(t)\rangle$ is determined by the Schrödinger equation

$$i\hbar\frac{\partial}{\partial t}|\Psi(t)\rangle = \mathcal{H}\,|\Psi(t)\rangle \tag{3.10}$$

once the Hamiltonian operator $\mathcal{H}$ is specified. Substituting eqn. 3.1 into the Schrödinger equation yields

$$\frac{\partial a_j}{\partial t} = \frac{1}{i\hbar}\sum_k \langle j|\,\mathcal{H}\,|k\rangle\, a_k \tag{3.11}$$

Inserting this result into eqn. 3.9, and using the definition of the density matrix elements (eqn. 3.6), as well as the Hermitian property of $\mathcal{H}$ gives

$$\frac{\partial \rho_{jk}}{\partial t} = \frac{1}{i\hbar}\sum_m (\mathcal{H}_{jm}\rho_{mk} - \rho_{jm}\mathcal{H}_{mk}) \tag{3.12}$$

This is the Liouville equation describing the time evolution of the density matrix, given a Hamiltonian $\mathcal{H}$. In operator form, eqn. 3.12 becomes

$$\frac{\partial \rho}{\partial t} = \frac{1}{i\hbar}[\mathcal{H}, \rho] \tag{3.13}$$

The theory of resonance fluorescence of $^{136}Ba^{+}$ is described by the solutions of the Liouville equation, with an appropriate choice of Hamiltonian $\mathcal{H}$.

3.1.3 The Ba^{+} system

The wavefunction of the atom is initially represented in the time-independent basis $\{|0\rangle, |1\rangle, |2\rangle\}$ as

$$|\psi\rangle = \begin{pmatrix} |1\rangle \\ |2\rangle \\ |3\rangle \end{pmatrix} \tag{3.14}$$

where the basis states correspond to the the eigenstates of J^2 as depicted in fig. 3.1 and §3.1.1. The time-dependent Hamiltonian for a three level system coupled with resonant laser fields is,

$$\mathcal{H} = \begin{pmatrix} \hbar\omega_0 & \hbar\Omega_B e^{i\omega_B t} & 0 \\ \hbar\Omega_B^* e^{-i\omega_B t} & \hbar\omega_1 & \hbar\Omega_R e^{-i\omega_R t} \\ 0 & \hbar\Omega_R^* e^{i\omega_R t} & \hbar\omega_2 \end{pmatrix} \tag{3.15}$$

The diagonal terms are the energies of the basis states $\{|1\rangle, |2\rangle, |3\rangle\}$, respectively, while the off-diagonal terms couple these states via laser fields at frequencies $\omega_{B,R}$. Quantum mechanically, the exponential factors in these off diagonal entries represent the absorption/emission of a photon of energy $\hbar\omega_{B,R}$. The amplitudes of the laser fields are proportional to $\Omega_{B,R}$, called the Rabi (after Isaac Isidor Rabi) frequencies. In addition, notice that $\rho_{13} = 0$, as there is no dipole transition between $|1\rangle$ and $|2\rangle$ in the Ba^{+} system.

The Liouville equation (eqn. 3.13) involves ρ and $\mathcal{H}$, but not the atomic wavefunction $|\psi\rangle$. The mathematics of the Liouville equation are therefore simplified if $\mathcal{H}$

is transformed to a time-independent form via some choice of unitary transformation U. By inspection,

$$U = \begin{pmatrix} e^{i\omega_0 t} & 0 & 0 \\ 0 & e^{it(\omega_1+\Delta_B)} & 0 \\ 0 & 0 & e^{it(\Delta_B-\Delta_R+\omega_2)} \end{pmatrix} \tag{3.16}$$

where $\Delta_{B,R}$ are the detunings of the lasers fields from resonance, defined as

$$\Delta_B = \omega_B - (\omega_1 - \omega_0) \tag{3.17}$$

$$\Delta_R = \omega_R - (\omega_1 - \omega_2) \tag{3.18}$$

To preserve the equations of motion, the Hamiltonian, density matrix, and wavefunction are transformed

$$\mathcal{H}' = U\mathcal{H}U^{-1} - i\hbar\frac{\partial U^{-1}}{\partial t} \tag{3.19}$$

$$\rho' = U\rho U^{-1} \tag{3.20}$$

$$|\psi\rangle' = U|\psi\rangle \tag{3.21}$$

The time dependence is therefore entirely transferred from $\mathcal{H}$ to ρ' and $|\psi\rangle'$. The Hamiltonian becomes

$$\mathcal{H}' = \begin{pmatrix} 0 & \hbar\Omega_B & 0 \\ \hbar\Omega_B^* & -\hbar\Delta_B & \hbar\Omega_R \\ 0 & \hbar\Omega_R^* & \hbar(\Delta_R - \Delta_B) \end{pmatrix} \tag{3.22}$$

At this point, eqn. 3.13 can be evaluated, which gives five independent equations for

the time derivatives of the density matrix elements, called the optical Bloch equations

$$\frac{\partial \rho_{11}}{\partial t} = i\frac{\Omega_B}{2}(\rho_{12} - \rho_{21}) + \Gamma_B \rho_{22} \tag{3.23}$$

$$\frac{\partial \rho_{33}}{\partial t} = i\frac{\Omega_R}{2}(\rho_{32} - \rho_{23}) + \Gamma_R \rho_{22} \tag{3.24}$$

$$\frac{\partial \rho_{13}}{\partial t} = i\left[(\Delta_R - \Delta_B)\rho_{13} + \frac{\Omega_R}{2}\rho_{12} - \frac{\Omega_B}{2}\rho_{23}\right] \tag{3.25}$$

$$\frac{\partial \rho_{12}}{\partial t} = i\left[\frac{\Omega_B}{2}(\rho_{11} - \rho_{22}) + \frac{\Omega_R}{2}\rho_{13} - \Delta_B \rho_{12}\right] - \frac{\Gamma}{2}\rho_{12} \tag{3.26}$$

$$\frac{\partial \rho_{32}}{\partial t} = i\left[\frac{\Omega_R}{2}(\rho_{33} - \rho_{22}) + \frac{\Omega_B}{2}\rho_{31} - \Delta_R \rho_{32}\right] - \frac{\Gamma}{2}\rho_{32} \tag{3.27}$$

where the spontaneous decay widths

$$\Gamma_B = 2\pi \times 15.2\text{MHz} \qquad \Gamma_R = 2\pi \times 5.28\text{MHz} \tag{3.28}$$

have been added in by hand, and $\Gamma = \Gamma_R + \Gamma_B$ [21]. Using eqns. 3.7-3.8, the steady-state population density is found by setting the optical Bloch equations equal to zero. The population density in the $6P_{1/2}$ state, ρ_{22} is [21]

$$\rho_{22} = \frac{4(\Delta_B - \Delta_R)^2 \Omega_B^2 \Omega_R^2 \Gamma}{Z} \tag{3.29}$$

where,

$$\begin{aligned} Z = \quad & 8(\Delta_B - \Delta_R)^2 \Omega_B^2 \Omega_R^2 \Gamma + 4(\Delta_B - \Delta_R)^2 \Gamma^2 Y \\ & +16(\Delta_B - \Delta_R)^2 (\Delta_B^2 \Omega_R^2 \Gamma_B + \Delta_R^2 \Omega_B^2 \Gamma_R) \\ & -8\Delta_B(\Delta_B - \Delta_R)\Omega_R^4 \Gamma_B + 8\Delta_R(\Delta_B - \Delta_R)\Omega_B^4 \Gamma_R \\ & +(\Omega_B^2 + \Omega_R^2)^2 Y \end{aligned} \tag{3.30}$$

and

$$Y = \Omega_B^2 \Gamma_R + \Omega_R^2 \Gamma_B \tag{3.31}$$

The blue and red fluorescence rates are given by $\Gamma_{B,R}\rho_{22}$. The blue fluorescence rates at various fixed blue detunings, as a function of red detuning, are plotted in fig.

3.2. Though the expression governing these lineshapes is complicated, a few features are worth mentioning. First, the *two-photon resonance* (the dip in the fluorescence to zero, close to the resonance peak) occurs when the detunings of both transitions are equal. In this case, the population is coherently transferred between the $6S_{1/2}$ and $5D_{3/2}$ states, with no residence time in the $6P_{1/2}$ state. The second feature of note is that the fluorescence width and peak height depend on the amplitude of the laser fields, proportional to $\Omega_{B,R}$. The scaling of the width of the distribution with the laser intensities is called power broadening. In practice, the fluorescence yield as a function of laser power is measured, from which the power broadening can be deduced. This phenomenon is described in detail in §3.2.

3.2 Power Broadening

The steady-state $6P_{1/2}$ population density will increase as a function of both laser powers, but cannot exceed 50% occupation (assuming no stimulated emission). As either laser intensity is increased, the peak fluorescence rate will saturate. At this point, the wings of the $6P_{1/2}$ spectral distribution will grow as the laser power is further increased, leading to a broadening of the natural linewidth Γ.

Consider the simple case of a two level atom with an energy splitting $\Delta E = \hbar\omega_0$ between two states $|1\rangle$ and $|2\rangle$. Using the density matrix methods presented in §3.1, the population density of the upper state, ρ_{22}, in the presence of a laser field at frequency ω and intensity I is

$$\rho_{22}(\omega) = \frac{s_0/2}{1 + s_0 + (2\Delta/\Gamma)^2} \tag{3.32}$$

where Γ is the natural linewidth of the upper state, $s_0 = I/I_{sat}$ is the saturation parameter, I_{sat} is the saturation intensity of the transition and $\Delta = \omega - \omega_0$ is the detuning of the laser frequency from resonance [22]. Evidently, the spectral profile of the emitted radiation is a Lorentzian with a broadened linewidth

$$\Gamma_P = \Gamma\sqrt{1 + s_0} \tag{3.33}$$

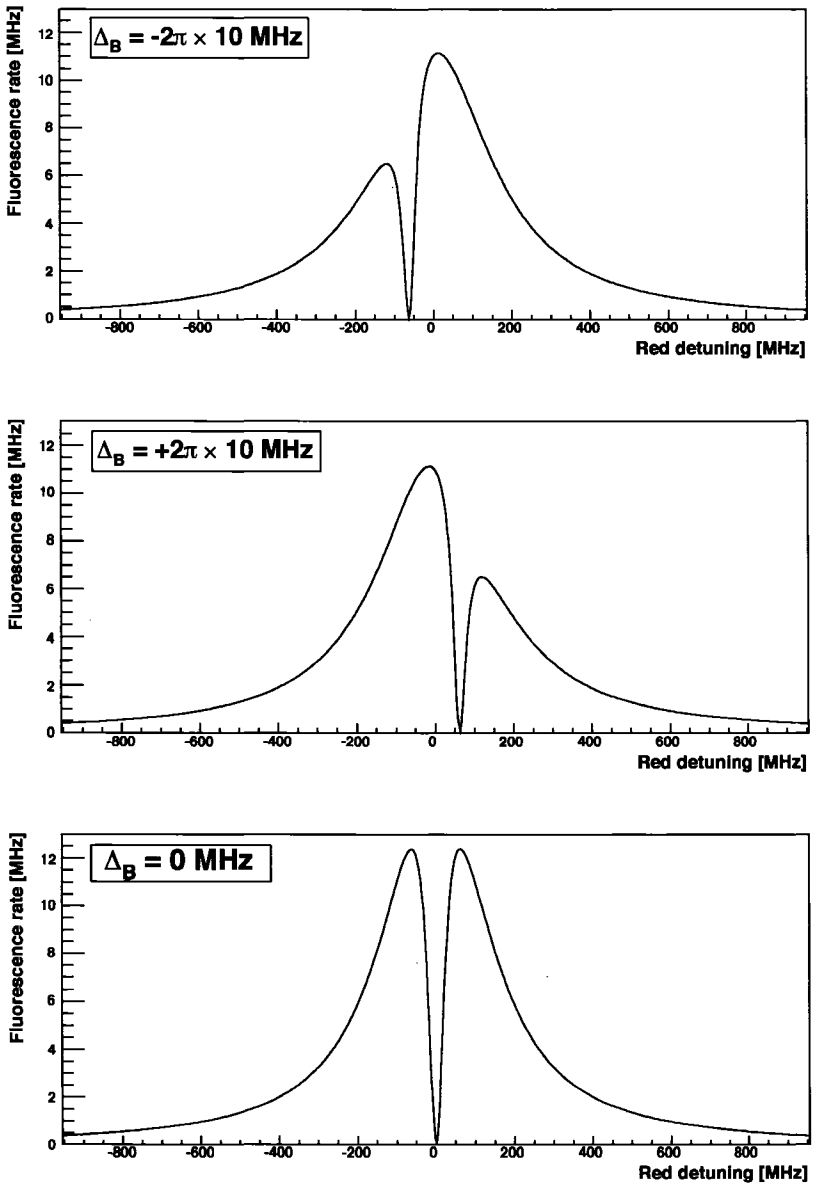

Figure 3.2: Lineshape, or blue fluorescence rate $\Gamma_B \rho_{22}$, for the $^{136}Ba^+$ $6P_{1/2} \leftrightarrow 6S_{1/2}$ transition at different blue detunings ($\Omega_R = \Omega_B = 2\pi \times 10$ MHz).

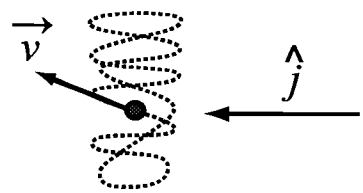

Figure 3.3: Doppler broadening of laser induced fluorescence due to distribution of ion velocity in the direction of the laser, $\vec{v} \cdot \hat{j}$.

For this two-level atom, the fluorescence from the excited state on resonance (from eqn. 3.32) is

$$\Gamma\rho_{22}(\omega_0) = \frac{\Gamma}{2}\frac{s_0}{(1+s_0)} \tag{3.34}$$

The two limiting cases are

$$\begin{aligned} s_0 &\ll 1: \quad \Gamma\rho_{22}(\omega_0) \sim \frac{\Gamma}{2}s_0 \\ s_0 &\gg 1: \quad \Gamma\rho_{22}(\omega_0) \sim \frac{\Gamma}{2} \end{aligned} \tag{3.35}$$

The fluorescence is linear in laser intensity for low powers, and saturates for high powers. It can be shown that this behavior applies to the individual Ba^+ transitions as well [23].

3.3 Doppler Broadening

Consider an ion at rest emitting radiation at frequency ω_0, driven by a resonant laser field incident in a direction, $\hat{j}$. If the ion is instead moving at an instantaneous velocity $\vec{v}$, as in fig. 3.3, the laser field appears Doppler shifted to the ion. In the ion's rest frame, the laser field is shifted to a frequency ω_0', given by the classical Doppler shift formula

$$\omega_0' = \omega_0\left(1 - \frac{\vec{v}\cdot\hat{j}}{c}\right) \tag{3.36}$$

assuming $|\vec{v}| \ll c$. This leads to a broadening of the ion's absorption profile, and hence fluorescence emission profile. This broadening can then be calculated if the

ion's velocity distribution in the $\hat{j}$ direction, v_j, is known.

In the case of a Maxwell-Boltzman velocity distribution, the probability of an ion of mass m with kinetic energy k_BT, having a velocity between v_j and $v_j + dv_j$ is

$$P(v_j)dv_j = \sqrt{\frac{m}{2\pi k_B T}} \exp\left(-\frac{mv_j^2}{2k_B T}\right) dv_j \tag{3.37}$$

Using eqn. 3.36, the absorption profile of the ion between ω_0' and $\omega_0' + d\omega_0'$ is

$$P(\omega_0')d\omega_0' = \frac{2}{\sigma_D\sqrt{\pi}} \exp\left(-\frac{4\left(\omega_0 - \omega_0'\right)^2}{\sigma_D^2}\right) d\omega_0' \tag{3.38}$$

where the Doppler linewidth parameter is

$$\sigma_D = \frac{\omega_0}{c}\sqrt{\frac{8k_BT}{m}} \tag{3.39}$$

The full-width at half-max Doppler linewidth, Γ_D, of this distribution is

$$\Gamma_D = \sigma_D\sqrt{\ln 2} = \frac{\omega_0}{c}\sqrt{\frac{8k_BT\ln 2}{m}} \tag{3.40}$$

3.4 Experimentally measured linewidth

The experimentally observed fluorescence intensity spectrum of a trapped ion is a convolution of the ion's natural linewidth and any other processes that affect the ion's absorption (and hence emission) profile. In the specific case of an ion in thermal equilibrium with a 293 K buffer gas, the dominant process affecting the absorption of resonant laser photons is the ion's Doppler velocity profile along the laser axis (see §3.3). A 293 K ($\sim$ 0.03 eV) ion, for example, has a broadened absorption profile of $\sim$ 500 MHz. Other effects, such as collisional broadening, are small perturbations compared to this broadening. The convolution of the natural lineshape, $\mathcal{L}(\omega)$, and

the Doppler velocity profile, $P(\omega)$, is then

$$I(\omega) = I_0 \int_0^\infty P(\omega_0' - \omega_0)\mathcal{L}(\omega - \omega_0')d\omega_0' \tag{3.41}$$

where I_0 is an overall scaling of the fluorescence intensity and ω_0 is the frequency of the observed transition.

If the natural lineshape is a Lorentzian, and the velocity profile is Maxwellian (see eqn. 3.38), then eqn. 3.41 is called a Voigt profile, which can be expressed in terms of the real part of the complex error function with a complex argument [20]. In practice this function is available in most numerical packages, so performing the actual convolution is unnecessary. In a 3-level system, $\mathcal{L}(\omega)$ is a complicated function (see eqn. 3.29). However, if the width of the velocity profile is much larger than the natural linewidth (as is the case here), and the power broadening is small, $\mathcal{L}(\omega)$ can be approximated as a Lorentzian. In ch. 5, the fluorescence spectrum of a single Ba^+ is measured. The ion's Doppler temperature is calculated by fitting the measured spectrum to a Voigt profile.

Chapter 4

The theory of single ion trapping

Ion traps were invented and tested by multiple groups in the early 1950s [24, 25]. According to W. Paul [26], ion traps "grew out of molecular beam physics, mass spectrometry, and particle accelerator physics" during the early to mid 1950s. According to Wuerker, Shelton, and Langmuir [27], the idea of containing charged particles with RF (radio-frequency) fields grew out of "studies in the laboratory on the electrical charging in vacuum of small dust particles." All authors emphasize the early connection between the strong focusing principle and ion trapping as a fundamental starting point. The trapping of ion clouds in RF Paul traps, and later single ions [28, 29, 30], laid the groundwork for such modern fields as laser cooling [29], quantum computation [31], mass spectrometry [32], and improved atomic frequency standards [33], to name a few. Ultra-high vacuum (UHV) linear ion traps are currently being pursued as a means of confining laser cooled ions for quantum computing [34]. Buffer gas cooled linear ion traps, a specific type of RF Paul trap, have proven useful as ion coolers and bunchers for heavy ion accelerator facilities [35], and as microwave frequency standards [36].

RF Paul traps confine ions in a quadrupole (or higher order) RF field [26]. Hyperbolic Paul traps have a closed geometry, and use this principle to confine ions in three dimensions by creating a potential minimum at the center of the trap. Linear ion traps, on the other hand, are cylindrical structures that allow ion injection/ejection access from either end of the trap. The RF field confines ions radially only, whereas a

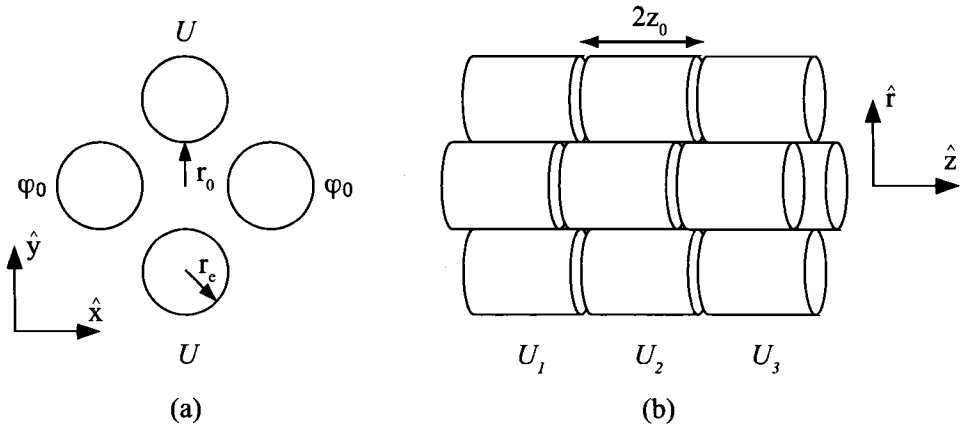

Figure 4.1: Three segments of a quadrupole linear ion trap. U is a DC potential, and $\varphi_0 = U + V\cos\Omega t$.

DC potential gradient applied along the cylindrical axis of the trap is used to confine or transport ions.

The linear ion trap used in this work is a buffer gas cooled, segmented linear RF Paul trap. Single ions are created at one end of the trap, and transported along a DC gradient to a trapping region for spectroscopic observation. The ion is trapped radially along the entire length of the trap via an RF field, while the longitudinal trapping region corresponds to the minimum of the DC gradient. During transport, the ion is cooled via collisions with a light buffer gas (e.g. He, Ar), such that it will settle at the DC minimum. The dynamics of a single ion in a linear ion trap, including both the electrodynamics and buffer gas cooling, are reviewed.

4.1 Ion confinement by RF and DC fields

The linear ion trap used in this work is described in detail in ch. 5. The trap consists of sixteen segments, each electrically isolated from each other. A segment, in turn, consists of four cylindrical electrodes with radius r_e, as shown in fig. 4.1a. Ions are confined radially at the center of the four electrodes (the "trapping region") by an RF field applied to two opposing electrodes, while the other two electrodes are held at RF ground. A longitudinal DC field, U, confines ions along the z-axis of the trap.

For example, to trap an ion in the middle segment in fig. 4.1b, the DC potentials must satisfy

$$U_2 < U_1, U_3 \tag{4.1}$$

In order to understand the radial trapping by the RF, consider the case of no longitudinal DC field. The potential inside the electrodes is then independent of z, and given by

$$\Phi = \frac{\varphi_0}{2}\left(1 + \frac{x^2 - y^2}{r_0^2}\right) \tag{4.2}$$

where

$$\varphi_0 = U + V\cos\Omega t \tag{4.3}$$

and r_0 is the distance from the center of the segment to the inner edge of an electrode in fig. 4.1a. The electric field $\mathbf{E}$ in the trapping region is the gradient of the potential Φ,

$$\mathbf{E} = -\nabla\Phi = -\frac{\varphi_0}{r_0^2}\left[x\hat{i} - y\hat{j}\right] \tag{4.4}$$

The equations of motion, in the x-y plane, of an ion of mass m and charge e are then

$$m\begin{pmatrix}\ddot{x}\\ \ddot{y}\end{pmatrix} = \frac{e\varphi_0}{r_0^2}\begin{pmatrix}-x\\ +y\end{pmatrix} = \frac{e}{r_0^2}(U + V\cos\Omega t)\begin{pmatrix}-x\\ +y\end{pmatrix} \tag{4.5}$$

The four dimensionless parameters a_x, a_y, q_x, and q_y,

$$\begin{aligned} a_x &= +\frac{4eU}{mr_0^2\Omega^2} \quad a_y = -\frac{4eU}{mr_0^2\Omega^2} \\ q_x &= +\frac{2eV}{mr_0^2\Omega^2} \quad q_y = -\frac{2eV}{mr_0^2\Omega^2} \end{aligned} \tag{4.6}$$

and a dimensionless time parameter

$$\xi = \frac{\Omega t}{2} + \phi \tag{4.7}$$

where ϕ is an arbitrary RF phase, are introduced do simplify (and symmetrize) eqn. 4.5. Substituting these parameters in eqn. 4.5, the ion's motion along the x and y

axes is described by the Mathieu equation,

$$\frac{d^2u}{d\xi^2} + (a_u + 2q_u \cos 2\xi)\, u = 0 \tag{4.8}$$

where u represents either x or y, and the subscript u on any variable corresponds to either x or y. This notation is used from this point onwards.

General properties and solutions to the Mathieu equation are described in detail in many books [37]. There is no general closed-form solution to this equation. Rather, the equations of motion along x and y can be expressed as a series expansion,

$$u(\xi) = A_u e^{\mu_u \xi} \sum_{n=-\infty}^{\infty} C_{u,2n} e^{2in\xi} + B_u e^{-\mu_u \xi} \sum_{n=-\infty}^{\infty} C_{u,2n} e^{-2in\xi} \tag{4.9}$$

In general, μ_u is a complex number that can differ for x and y,

$$\mu_u = \alpha_u + i\beta_u \tag{4.10}$$

The parameters μ_u and $C_{2n,u}$ are functions of a_u and q_u only, independent of initial conditions. If μ_u is real or complex the amplitude increases exponentially and the ion is not stably bound. The motion is bound if and only if μ_u is purely complex, and β_u is bound,

$$\mu_u = i\beta_u \qquad 0 \leq \beta_u \leq 1 \tag{4.11}$$

In this stable regime, the solution becomes

$$u(\xi) = A_u \sum_{n=-\infty}^{\infty} C_{u,2n} e^{i\xi(2n+\beta_u)} + B_u \sum_{n=-\infty}^{\infty} C_{u,2n} e^{-i\xi(2n+\beta_u)} \tag{4.12}$$

Expanding the exponentials and gathering like terms,

$$u(\xi) = A'_u \sum_{n=-\infty}^{\infty} C_{u,2n} \cos\left[\xi\,(2n+\beta_u)\right] + B'_u \sum_{n=-\infty}^{\infty} C_{u,2n} \sin\left[\xi\,(2n+\beta_u)\right] \tag{4.13}$$

where $C_{u,2n}$ are coefficients that can be calculated for arbitrary n using recursive

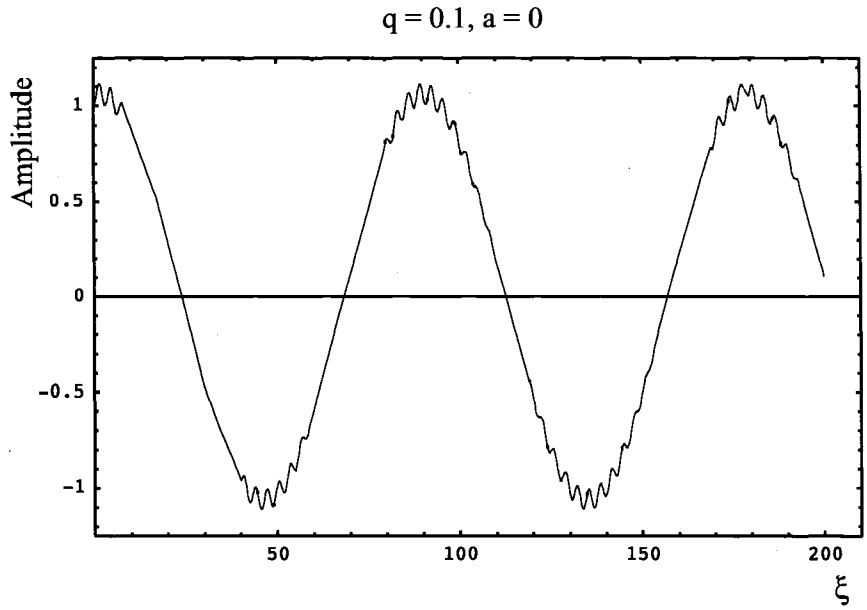

Figure 4.2: Numerical solution to eqn. 4.8 for $a = 0$, $q = 0.1$ in terms of the dimensionless time parameter ξ. The large, slow oscillation is the macromotion of the ion (due to the $n = 0$ term in eqn. 4.13), while the small fast oscillation is the micromotion (due to the $n > 0$ terms in eqn. 4.13).

relations derived in [37], and are functions of a_u and q_u only. $A'_u = A_u + B_u$ and $B'_u = i(A_u + B_u)$ are integration constants that depend on the initial conditions (ion position, ion velocity, and the RF phase at $t = 0$).

By inspection of eqn. 4.13, the ion trajectories are a superposition of oscillations in x and y at frequencies

$$\omega_u = (2n + \beta_u)\frac{\Omega}{2} \tag{4.14}$$

This relation connects the parameter β_u to the oscillation frequencies of the ion. For small β_u, it can be shown that the $n = 0, 1$ terms dominate [37] . The $n = 0$ term is responsible for the large scale oscillation of the ion, called the *macromotion*. The $n = 1$ term, as well as the higher order terms, are responsible for the small amplitude, higher frequency motion of the ion. This is called the *micromotion*. A numerical solution to eqn. 4.8 is shown in fig. 4.2, for $q = 0.1$, $a = 0$. The micromotion is clearly visible on top of the larger scale macromotion.

The values of a_u and q_u corresponding to experimental parameters such as mass,

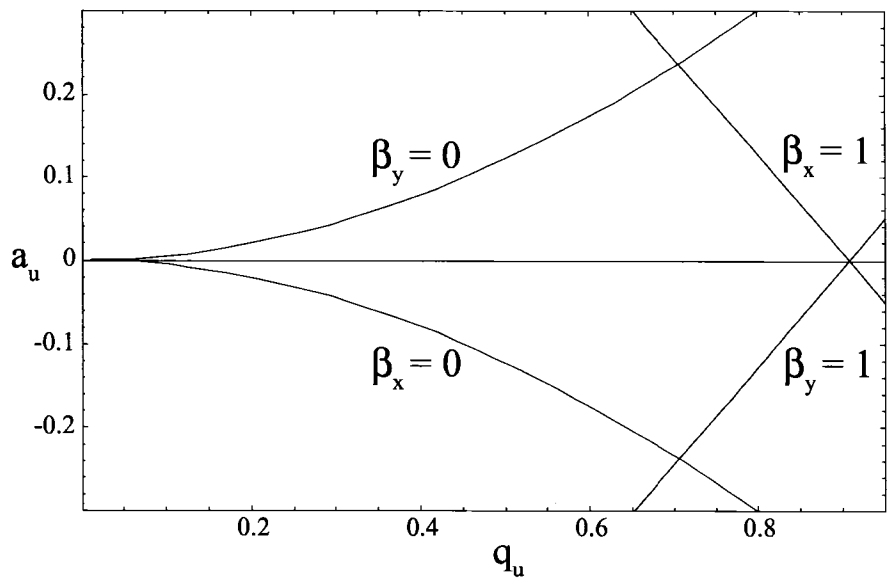

Figure 4.3: Stability diagram for the Mathieu equation (eqn. 4.8). $u(\xi)$ (eqn. 4.9) is stable for values of a and q inside the region defined by the solid curves.

charge, and voltage (eqn. 4.6), along with initial conditions fully determine the value of β_u via eqn. 4.12. Since the stability criterion (eqn. 4.11) is given in terms of β_u, it is of practical importance to invert this relationship, so that the values of a_u and q_u corresponding to stable solutions are known. This inversion is performed in detail in [37], and the result is a series expansion of the form

$$a_u = \sum_{n=0}^{\infty} \lambda_n (\beta_u) q_u^n \tag{4.15}$$

where λ_n are functions of β_u, calculable from a series expansion in [37]. These functions are called the *characteristic numbers* of the Mathieu equation, and are plotted in fig. 4.3 for a few values of β_u. Values of a_u and q_u within the area bounded by the solid lines correspond to stable ion trajectories. For $a_u = 0$, the largest value of q_u for which the ion's orbit is stable is 0.908.

4.2 RF trap depth (the psuedopotential)

The psuedopotential formulation, found in [28, 38, 27], utilizes a set of simplifying assumptions in order to qualitatively understand the motion of a single ion in an RF trap. This derivation is valid for the axes in which the ion is confined by the RF (x-y plane, in a linear trap). It is shown that to first order, a trapped ion undergoes simple harmonic motion in a parabolic potential.

Consider the ion's motion along one axis, such as x. For small values of β and q, the ion's displacement along x can be separated into two components,

$$x = X + \delta \tag{4.16}$$

Where X is the average value of the displacement over a complete period of the RF drive (the macromotion, due to the $n = 0$ term in eqn. 4.13), and δ is a fast small amplitude displacement (the micromotion, due to the $n > 0$ terms in eqn. 4.13), so that

$$\delta \ll X \qquad \frac{d\delta}{d\xi} \gg \frac{dX}{d\xi} \tag{4.17}$$

Substituting eqn. 4.16 into eqn. 4.8 and applying these assumptions, the Mathieu equation becomes

$$\frac{d^2\delta}{d\xi^2} = -\left(a - 2q\cos 2\xi\right)x \tag{4.18}$$

Assuming there is no DC field ($a = 0$, for simplicity), eqn. 4.18 becomes integrable

$$\int \left[\int \frac{d^2\delta}{d\xi' d\xi} d\xi'\right] d\xi = 2qX \int \left[\int \cos 2\xi' d\xi'\right] d\xi \tag{4.19}$$

Which yields for the small displacement,

$$\delta = -\frac{qX}{2}\cos 2\xi \tag{4.20}$$

Note that due to the minus sign, the micromotion of the ion is 180° out of phase with the driving RF field when the particle is stably bound. Plugging eqns. 4.16 and 4.20

back into the Mathieu equation (eqn. 4.8), the acceleration of the ion is

$$\frac{d^2x}{d\xi^2} = -aX + \frac{aqX}{2}\cos 2\xi + 2qx\cos 2\xi - X\left(q\cos 2\xi\right)^2 \tag{4.21}$$

Whereas this is the instantaneous acceleration, the average acceleration of the ion over one RF cycle is

$$\left\langle \frac{d^2x}{d\xi^2} \right\rangle = \frac{1}{\pi}\left(\int_0^\pi \frac{d^2X}{d\xi d\xi'}d\xi' + \int_0^\pi \frac{d^2\delta}{d\xi d\xi'}d\xi'\right) \tag{4.22}$$

The micromotion averages to zero over one RF cycle, so that the average acceleration becomes

$$\left\langle \frac{d^2X}{d\xi^2} \right\rangle = \frac{1}{\pi}\int_0^\pi \left(-aX + \frac{aqX}{2}\cos 2\xi' + 2qx\cos 2\xi' - X\left(q\cos 2\xi'\right)^2\right)d\xi' \tag{4.23}$$

which integrates to

$$\left\langle \frac{d^2X}{d\xi^2} \right\rangle = -\left(a + \frac{q^2}{2}\right)X \tag{4.24}$$

or, in terms of time t,

$$\left\langle \frac{d^2X}{dt^2} \right\rangle = -\left(a + \frac{q^2}{2}\right)\frac{X\Omega^2}{4} \tag{4.25}$$

This is the equation of a simple harmonic oscillator with frequency

$$\omega_0 = \sqrt{\left(a + \frac{q^2}{2}\right)\frac{\Omega^2}{4}} \tag{4.26}$$

For simplicity, assuming no DC field ($a = 0$), and substituting eqn. 4.6 into eqn. 4.25, the average acceleration becomes

$$\left\langle \frac{d^2X}{dt^2} \right\rangle = -\left(\frac{e^2V^2}{2m^2\Omega^2r_0^4}\right)X \tag{4.27}$$

By mechanical analogy, this corresponds to simple harmonic motion in a parabolic

well, with a characteristic depth

$$D_{RF} = \frac{eV^2}{4m\Omega^2 r_0^2} = \frac{qV}{8} \tag{4.28}$$

This RF pseudopotential formulation is valid in the transverse (x-y) plane only (see fig. 5.1a). Eqn. 4.28 is the radial trap depth, but is altered by the presence of a DC potential applied along the z-axis of the trap. The complete trap depth, in the presence of both RF and DC fields, is derived in the next section. In addition, an alternate derivation of D_{RF} using the characteristic numbers of the Matheiu equation is presented in appendix A.

4.3 Effect of a DC field on trap depth

In a linear trap, a DC field U applied as described in §4.1 creates a longitudinal confining potential (see eqn. 4.1). Whereas this potential has a longitudinal trap depth D_z, analogous to D_{RF} derived in §4.2, U also contributes to the radial trap depth by Laplace's equation.

Assuming the longitudinal confinement criterion (eqn. 4.1), the DC potential along z at $r = 0$ for the three segments shown in fig. 4.1b can be approximated by a potential well

$$V_{DC}(r = 0, z) = \left(\frac{U_{DC}}{z_0^2}\right) z^2 \tag{4.29}$$

where $U_1 = U_3$ and $U_{DC} = |U_1 - U_2|$. Laplace's equation in this region is

$$\nabla^2 V_{DC} = 0 \tag{4.30}$$

In cylindrical coordinates, Laplace's equation becomes

$$\frac{1}{r}\frac{\partial}{\partial r}\left(r\frac{\partial V_{DC}}{\partial r}\right) + \frac{1}{r^2}\left(\frac{\partial^2 V_{DC}}{\partial \phi^2}\right) + \frac{\partial^2 V_{DC}}{\partial z^2} = 0 \tag{4.31}$$

V_{DC} has no dependence on ϕ, so the second term vanishes. The third term, using

eqn. 4.29, becomes

$$\left.\frac{\partial^2 V_{DC}}{\partial z^2}\right|_{r=0} = \frac{2U_{DC}}{z_0^2} \tag{4.32}$$

Laplace's equation is then integrable. Integrating once,

$$\int \frac{\partial}{\partial r}\left(r\frac{\partial V_{DC}}{\partial r}\right)dr = -\int \frac{2U_{DC}}{z_0^2} r dr \tag{4.33}$$

Rearranging, and integrating again,

$$\int \frac{\partial V_{DC}}{\partial r} dr = -\int \frac{U_{DC}}{z_0^2} r dr \tag{4.34}$$

so that the radial component of the DC potential is

$$V_{DC}(r) = -\frac{U_{DC}}{2z_0^2} r^2 \tag{4.35}$$

Laplace's equation therefore requires that the DC potential given by eqn. 4.29 has a radial component. Physically, this is because the electric field lines originating on the inside faces of the center electrodes in fig. 4.1b cannot converge at the center of the trapping region; rather, they must curve outwards.

The full trap depth, in the case of a linear trap, has two components: radial and longitudinal. The radial depth D_r has contributions from both the RF and DC fields (eqns. 4.28 and 4.35), while the longitudinal trap depth D_z is created by the DC fields only. The full expressions are

$$D_r = \frac{qV}{8} - \frac{U_{DC} r_0^2}{2z_0^2} \tag{4.36}$$

$$D_z = U_{DC} \tag{4.37}$$

Increasing the DC trap depth for stronger confinement in z necessarily decreases the radial confinement.

4.4 Buffer gas cooling

In the absence of any collisions between a trapped ion and any other species (neutral or charged), the ion's motion is completely described by the Mathieu equation (eqn. 4.8). In this case, the ion is neither heated nor cooled (assuming no external influences, such as laser heating or cooling). Collisions between the ion and a background (buffer) gas, on the other hand, can either heat or cool the ion, possibly leading to ejection from the trap. The interaction of a trapped ion with a neutral buffer gas was first treated in detail analytically by Major and Dehmelt [38], and subsequently by many others [39, 40, 35, 41, 42, 3]. This problem has also been treated numerically [43, 40, 41, 44, 3] to name a few places. In general, the following cases are examined,

1. $m_I \gg m_B$

2. $m_I \sim m_B$

3. $m_I \ll m_B$

where m_I is the mass of the trapped ion, and m_B is the mass of the neutral buffer gas atom. Though the methods and assumptions vary in these studies, the qualitative results are consistent with each other: in the first case, ion-neutral collisions thermalize the ion with the buffer gas (cooling), while in the second and third case, ion-neutral collisions tend to heat the ion such that it is ejected from the trap. For this reason, buffer-gas cooled ion traps are usually operated with $m_I \gg m_B$.

A fairly complete explanation of cooling and heating is presented in [28, 40, 41]. Briefly, there always exists a region of phase space (defined in terms of the ion's secular phase and the RF phase) such that a buffer gas collision will cause an ion to absorb energy from the RF field, thereby heating it. This process is called RF heating, and is one of the main reasons responsible for an ion leaving the trap.

If $m_I \gg m_B$, the volume of "heating" phase space as compared to "cooling" phase space is very small. In addition, each collision can only add or subtract a small amount of energy (purely from kinematic arguments) from the ion, so on average the ion loses energy with each collision until it thermalizes with the buffer gas. If $m_I \sim m_B$, the volume of heating phase space is larger. In addition, collisions tend to alter the ion's

energy by a substantial amount, in contrast to the first case. Combining these two effects, this case exhibits optimal cooling , at the expense of a higher probability (per collision) of an ion ejecting from the trap [40]. If $m_I \ll m_B$, the heating phase space is substantial. Collisions therefore cause the ion to absorb energy from the RF field, which heats and ejects the ion quickly. In general, the conditions for optimal cooling ($m_I \sim m_B$) and long storage time ($m_I \gg m_B$) cannot be simultaneously satisfied. In the case of $^{136}Ba^+$, Ar is a good compromise between these two cases.

In practice, collisional cooling under a specific set of experimental circumstances needs to be simulated in order to find the optimal operating parameters (RF frequency, RF amplitude, DC voltages, buffer gas pressure, buffer gas type, etc.). Therefore, the basic scattering kinematics required for Monte Carlo simulation of a single ion in this linear trap, as developed in [41, 3] are briefly reviewed.

4.5 Ion-neutral scattering kinematics

Kim [41] discusses four models for collisions between trapped ions and neutral atoms for Monte Carlo purposes: classic hard sphere (HS), hard sphere variable size 1 (HS1), hard sphere variable size 2 (HS2), and realistic potential (RP). HS1 is shown [41] to be applicable in the case of noble buffer gases, and is used in this work.

HS is the simplest and most commonly used model, consisting of hard sphere scattering with a classical collisional cross section computed from the atomic radii of the ion and buffer gas atoms. This method reproduces the qualitative results discussed in §4.4 for a noble buffer gas, but fails to produce the correct scattering angle distribution when compared to other methods. HS predicts a flat angular distribution of scattering angles in the center of mass frame of the ion-neutral collision due to the "hard-wall" interaction potential assumed, whereas this is explicitly not true.

HS2 and RP use realistic scattering potentials for ion-neutral scattering, and are useful when the buffer gas is non-inert (such as cooling with N_2 [41]). These models are discussed and compared to experiment in [41]. HS2 and RP are computationally intensive, and unnecessary in the case of ba^+ in He or Ar. HS1 is based on the Langevin collision theory for inert gases, which uses a velocity dependent cross section

to account for the induced electric dipole moment in the neutral atom [45]. This results in a net attractive force between the ion and the neutral buffer gas atom. The basic results of this theory are presented here.

Langevin uses the interaction potential

$$V(r) = \begin{cases} -\frac{\alpha e^2}{2r^4} & r > S \\ \infty & r \leq S \end{cases} \tag{4.38}$$

where r is the distance between the atom and the ion, α is the polarizability of the buffer gas, e is the charge of the ion, and S is the "hard sphere" radius of the atom. The three dimensional scattering of an ion with a neutral atom, given the interaction potential $V(r)$ is solved in [6, 46], so only the relevant results are given here. The scattering angle $\theta(b, E)$ of the ion off a neutral atom in the center of mass coordinate system is

$$\theta(b, E) = \pi - 2b \int_{r_0}^{\infty} \frac{1}{r^2} \left[1 - \left(\frac{b}{r}\right)^2 - \frac{V(r)}{E_{Tot}} \right]^{-\frac{1}{2}} dr \tag{4.39}$$

where b is the impact parameter, r_0 is the distance of closest approach, and E_{Tot} is the total conserved energy of the system. The orbit of the ion is determined by two parameters, the relative initial velocity u and the impact parameter b. For these orbits, there is a critical value of b,

$$b_0 = \left(\frac{4e^2\alpha}{\mu u^2} \right)^{\frac{1}{4}} \tag{4.40}$$

where μ is the ion-neutral reduced mass

$$\mu = \frac{m_I m_B}{m_I + m_B} \tag{4.41}$$

If $b < b_0$, the ion and atom form a short lived compound before scattering randomly into 4π. If $b \geq b_0$, the ion comes no closer to the atom center than $b_0/\sqrt{2}$, and scatters at an angle θ given by eqn. 4.39. For the case $b < b_0$, a hard-sphere depolarization

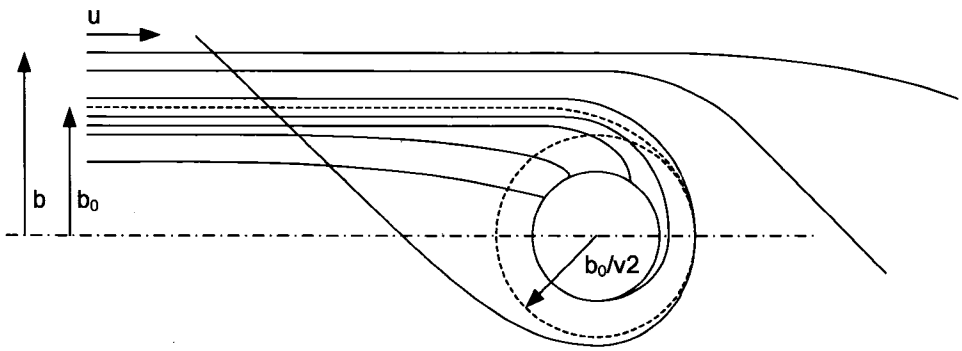

Figure 4.4: A typical family of trajectories of an ion scattering off of a neutral atom, assuming the Langevin collision theory described here [6]. If $b < b_0$, the ion and atom form a short lived compound before scattering randomly. If $b \geq b_0$, the ion scatters with at an angle θ given by eqn. 4.39.

cross section is defined [6],

$$\sigma_L(u) = \pi b_0^2 = \frac{\pi}{u}\sqrt{\frac{4e^2\alpha}{\mu}} \tag{4.42}$$

Assuming the buffer gas atoms have a Maxwellian velocity distribution with a temperature T, and that the ion is thermalized with the buffer gas, the average relative velocity is

$$u = \sqrt{\frac{3k_BT}{\mu}} \tag{4.43}$$

The average time between randomizing collisions (i.e. when $b \leq b_0$) is therefore

$$\tau_L = \frac{1}{n\sigma_L u} = \frac{k_BT}{2\pi P}\sqrt{\frac{\mu}{\alpha e^2}} \tag{4.44}$$

where n is the number density of the buffer gas, P is the pressure, and the ideal gas law has been assumed. Combining eqns. 4.43 and 4.44, the Langevin mean free path is

$$\lambda_L = u\tau_L = \frac{1}{2\pi P}\sqrt{\frac{3k^3T^3}{\alpha e^2}} \tag{4.45}$$

Gas	α [$\AA^3$]	λ_L [cm]	τ_L [sec]	λ_{HS} [cm]
Helium	0.205	7.7×10^{-3}	5.65×10^{-8}	11.3×10^{-3}
Argon	1.64	2.7×10^{-3}	5.64×10^{-8}	8.4×10^{-3}
Krypton	2.48	2.2×10^{-3}	5.94×10^{-8}	7.4×10^{-3}
Xenon	4.04	1.7×10^{-3}	5.29×10^{-8}	6.5×10^{-3}

Table 4.1: Table of polarizability [3], Langevin mean free path λ_L, and average time between collisions τ_L calculated for a Ba^+ interacting with noble gases listed. The values of λ_L and τ_L are calculated using eqns. 4.44 and 4.45 at T = 239.15 K and $P = 1$ torr. The hard-sphere mean free path, λ_{HS} is shown for comparison.

which is independent of the relative velocity u. Values of α [3], λ_L, τ_L, and the standard hard-sphere mean free paths, λ_{HS}, are listed in table 4.1. These values are used in a hard-sphere scattering Monte Carlo in ch. 5 in order to qualitatively understand heating and cooling of a single trapped Ba^+. A full Monte Carlo implementation of the Langevin theory is presented in [41].

Chapter 5

Single ion trapping experimental results

A linear ion trap, optimized for external ion loading, and the trapping/observation of individual ions via resonance fluorescence is described. This ion trap is based on the principles discussed in ch. 4, utilizing buffer gas cooling to thermalize ions into a potential well for observation. First, the construction and experimental details of the trap are discussed. Second, individual ions are trapped in He, Ar, and He/Xe mixtures, and their quantized fluorescence observed. Third, the temperature of single trapped ions cooled by He is measured via spectroscopic techniques (see §3.3). Finally, the unloading rate of individual ions cooled by He, in the presence of small concentrations of Xe, is measured. A model explaining this behavior is presented and fit to experimental data. This system fulfills the major design goals of a future EXO ion trap, as discussed in ch. 1.

5.1 Experimental setup

The linear trap ion trap system consists of the following sub-systems:

- Linear ion trap
- Ion loading system

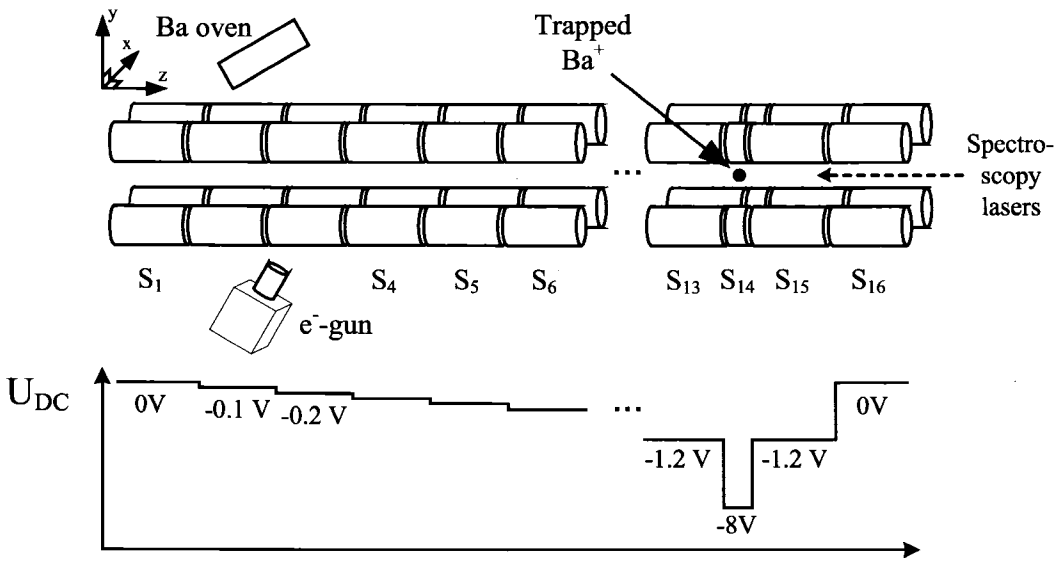

Figure 5.1: Schematic of the linear ion trap used in this work to observe single ions. Ions are loaded at S_3 and observed at S_{14} via resonance fluorescence.

- Vacuum system housing the trap
- Buffer gas system
- 493 nm and 650 nm lasers for creating resonance fluorescence
- Fluorescence collection system for observing trapped ions

5.1.1 The linear ion trap

The linear ion trap, shown schematically in fig. 5.1, consists of sixteen segments placed back to back as described in §4.1. Segments are labeled S_i, where $i = 1$ is the first segment. Each segment consists of four stainless steel electrodes in a quadrupole configuration, as in fig. 4.1. Ions are confined inside the trap by applying a sinusoidial voltage with a DC offset (eqn. 4.3) to two diagonal electrodes, while keeping the other two electrodes at RF ground, with the same DC offset. Each segment is electrically isolated from all other segments by small insulating spacers[1], as shown in a cutaway view in fig. 5.2. The electrodes interlock with each spacer as shown, which are held

[1]Vespel® polyimide, by DuPont

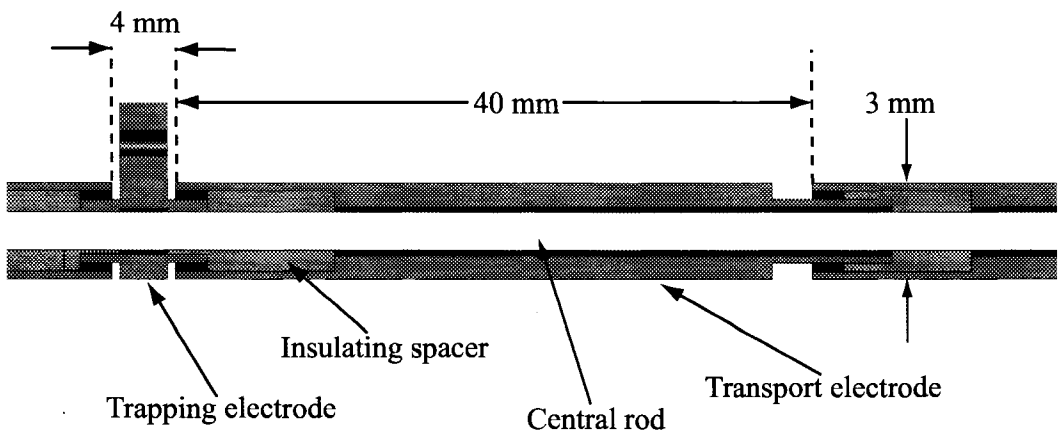

Figure 5.2: Cutaway view of electrodes 12-14, showing internal construction and electrical isolation by insulating spacers.

in place on a central rod. The central rod is structural, minimizing sagging along the length of the trap. A DC gradient along the z-axis of the trap transports and traps ions longitudinally at S_{14}. The DC gradient is created by placing the following DC potentials on the segments

$$U_{DC} = \{0\text{V}, -0.1\text{V}, -0.2\text{V}, ... - 1.3\text{V}, -1.4\text{V}, -8.0\text{V}, -1.4\text{V}, 0\text{V}\} \quad (5.1)$$

where the first element corresponds to S_1 in fig. 5.1. Ions are loaded at S_3 (see §5.1.3) and transported to S_{14} for observation via resonance fluorescence.

The ideal RF trapping potential is hyperbolic (eqn. 4.2). Creating a purely hyperbolic potential requires hyperbolically shaped electrodes, whereas the rods used in this trap have a circular cross section for ease of construction. In this case, constraining the electrode radius r_e, and trap radius r_0, (see fig. 4.1) such that

$$r_e = 1.148 r_0 \quad (5.2)$$

yields the best approximation to an ideal quadrupole field at the trap center [47].

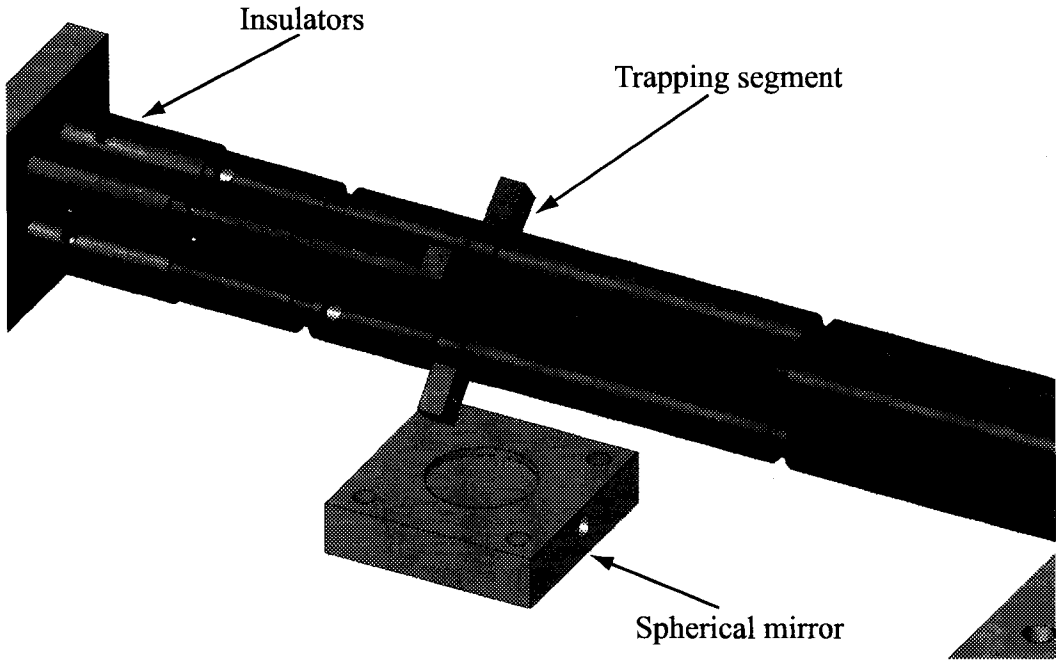

Figure 5.3: Closeup of $S_{12} - S_{16}$, including the spherical mirror used for increasing the fluorescence yield (see §5.1.6).

In this trap, $r_e = 3$ mm and $r_0 = 2.61$ mm. All electrodes have the same radial dimensions. The longitudinal dimension of each segment, in contrast, varies in length. $S_1 - S_{13}$,and $S_{15} - S_{16}$ (*transport segments*) are each 40 mm long, whereas S_{14} (*trapping segment*) is 4 mm long, as illustrated in figs. 5.1-5.3.

Whereas the transport segments are used to move an ion along the trap, the trapping segment confines an ion to as small a spatial region possible. This concentrates the single ion fluorescence signal, while minimizing the scattered light accepted by the fluorescence collection optics. S_{14} cannot be made arbitrarily short, though, due to the constraint posed by eqn. 4.36: reducing z_0 simultaneously decreases the longitudinal potential well size and radial potential well depth. This defocusing is a consequence of Laplace's equation, and cannot be avoided. The trapping segment is chosen to be 4 mm in length, which is a compromise between these factors. The trapping and neighboring segments are shown in fig. 5.3. The tabs on S_{14} are used for electrical connections.

Parameter	Value
V_{RF}	300 V_{pp}
Ω	1.2 MHz
D_r	3.8 V
D_z	6.8 V
r_0	2.61 mm
r_e	3 mm
z_0	2 mm
q	0.52
a	0.05

Table 5.1: Linear ion trap standard operating and geometric parameters.

The total trap length is 604 mm. This is chosen such that an ion with $\sim$ eV of kinetic energy, entering the trap at S_1 will collide with enough buffer gas atoms (see §4.4) to thermalize at S_{14} without ejecting back out of the trap entrance. The trap can be made arbitrarily longer or shorter by adding or removing segments. In addition, an aperture mount (see fig. 5.5) can be used to separate a high pressure section of the trap from a low pressure section, if necessary. This can be used to slow down a high energy ion.

The standard operating and essential geometric parameters of the linear ion trap described here are listed in table 5.1.

5.1.2 Electrical system

Diagonal electrodes in each segment are shorted to each other inside of the vacuum system, as illustrated in fig. 5.4, in order to create the electrical configuration shown in fig. 4.1. Each segment therefore requires two external electrical feeds: RF+DC and DC only. The RF is supplied by a programmable function generator[2], coupled to a high-power, wide-band RF amplifier[3], A_1, which is internally back-terminated with 50 Ω. The RF is run at at an amplitude of 150 V (300 V_{pp}), at 1.2 MHz, which is attainable directly out of this amplifier. The amplified RF is sent through the

[2]HP-8656B
[3]ENI-A150

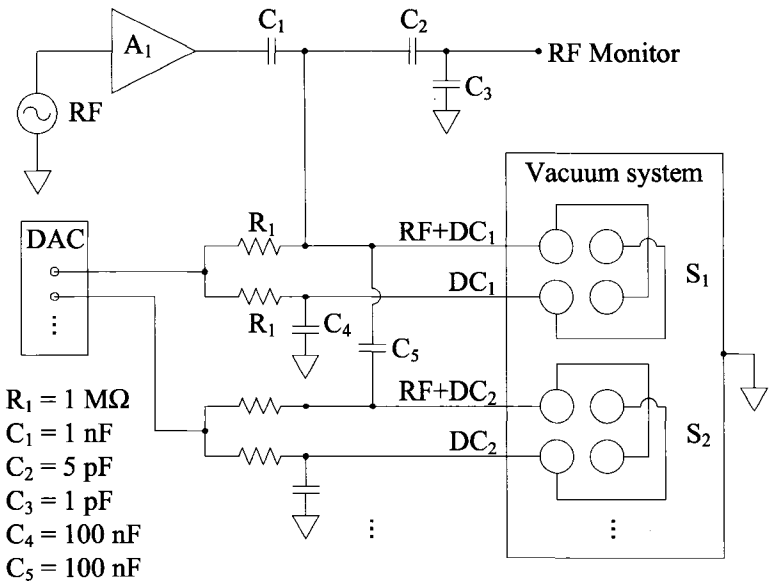

Figure 5.4: Linear ion trap RF and DC electrical system. Only two of sixteen identical segments are shown.

DC blocking capacitor C_1, and reduced for external monitoring through a capacitive divider formed by C_2 and C_3. Sixteen independent DC channels are supplied by a computer controlled 16-bit DAC. The DC is combined with the RF through resistors R_1, which form bias-tees. These resistors have a precision of 0.1%, and are chosen to be large to prevent the RF from passing backwards into the DAC. The RF power flows through the trap, which is purely capacitive ($\sim$ 18 pF per segment), and to ground through C_4. This circuit is repeated for each segment. The total capacitive load on the amplifier is measured to be $\sim$ 600 pF, or 221 Ω at 1.2 MHz.

5.1.3 Ion loading system

The ion loading system is composed of a Ta foil, a Ba wire, and an electron gun (e-gun). The 1 cm^2 Ta foil, labelled *Ba Oven* in fig. 5.1, is oriented such that it's flat surface is visible through S_3. It is placed $\sim$ 1 cm from the edge of the electrodes, and is outfitted with electrical leads at each end for heating, as well as a K-type thermocouple for temperature readout. The e-gun is placed on the other side of S_3, also pointing inwards. The Ba wire, not shown, faces the Ta oven. After the vacuum

system is pumped down and baked, a current of 6 A is run through the Ba wire which plates the Ta oven with atomic Ba. Ohmically heating the Ta foil produces a neutral Ba vapor in the region of S_3, which is ionized by CW or pulsed e^- emission from the e-gun. For loading a small number of ions (< 10), the oven is run at $\sim$ 100 °C, and the e-gun is pulsed for $\sim$ 10 s at 5 μA emission current. For loading many ions, the oven is run at $\sim$ 300 °C and the e-gun is run CW at 5 μA emission current.

5.1.4 Vacuum and buffer gas systems

The linear ion trap is housed in a rectangular, electropolished UHV vacuum chamber, shown in fig. 5.5. The internal dimensions of the chamber are 83.82 cm $\times$ 15.24 cm $\times$ 22.86 cm, or 29202 cm^3. Conflat flanges allow for electrical, optical, and pumping access to the chamber. The trap is mounted vertically inside of the chamber, such that S_1 is at the top. The pressure is measured at the top and bottom of the system by two dual gauges[4]. A 8" all-metal gate valve separates the chamber from a 520 ℓ/s turbo pump[5], backed by a scroll pump[6]. An RGA[7] is attached to the system, which serves two purposes. First, it is used to measure the quality of the vacuum after a bakeout. Second, it is used to measure partial pressures of buffer gases, used in §5.3. The entire system shown in fig. 5.5 is bakeable up to 150 °C in an external oven that fits over the vacuum chamber. This is necessary after the system has been exposed to air, in order to get rid of any electronegative impurities (e.g. O_2, CO_2, NO_2, oils, etc.). These impurities react with Ba and Ba^+, causing neutralization or a molecule to form which cannot be trapped and observed in this system. A three day bakeout is sufficient to remove these impurities to partial pressures $\lesssim 10^{-9}$ torr (as measured on the RGA), with a total system base pressure $\leq 3 \times 10^{-9}$ torr.

A buffer gas is used to cool the ion into the trap minimum at S_{14}. The buffer gas system, shown in fig. 5.6 connected to the main vacuum system, is composed of

[4]Pfeiffer Dual Gauge model PKR-251 (combination Pirani gauge and cold cathode gauge, with an accessible pressure range $3 \times 10^{-9} - 760$ Torr)

[5]Pfeiffer TMU-xxx

[6]Edwards XD-5

[7]Stanford Research Systems RGA-300

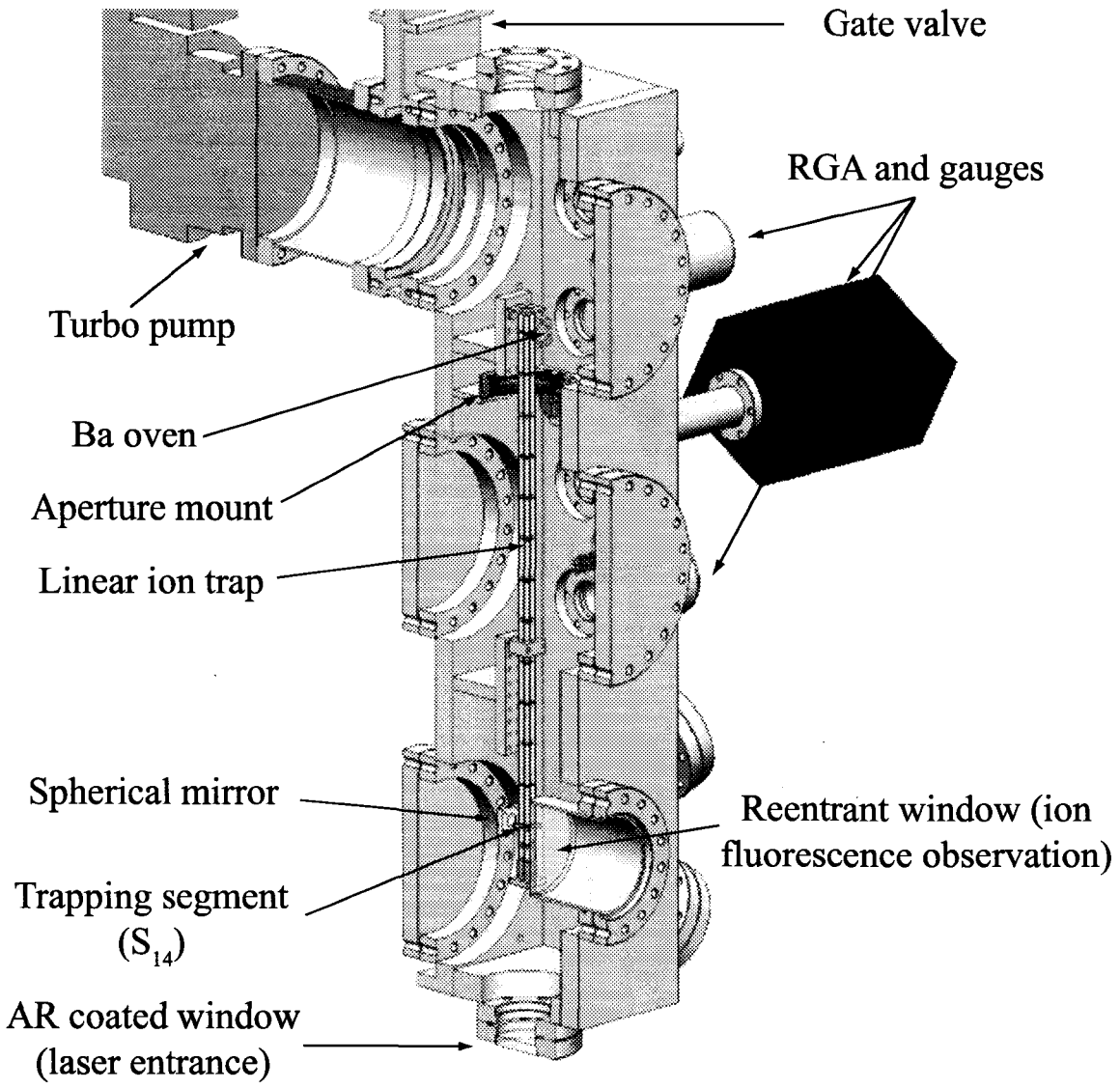

Figure 5.5: Cutaway view of the linear ion trap housed inside the vacuum system.

gas bottles, pressure gauges, a 70 ℓ/s turbo pump[8], mixing chambers, a gas purifier[9], and a flowmeter with pressure-feedback control[10]. All components are all-metal, and bakeable to 150 °C. Three gas bottles (He, Ar, Xe) are plumbed together along a manifold via all-metal valves[11] (V_1-V_3). This manifold is connected to regulator R_1, which drops the upstream pressure down to $\leq$ 760 Torr. The downstream pressure is read out on gauge G_2[12]. At this point, the system can be run in one of two modes: single buffer gas injection or mixed buffer gas injection. In the first mode, a single buffer gas (e.g. He only) is passed through the gas purifier (labelled "Getter" in fig. 5.6) and into the main vacuum system via valve V_{10}. The gas is continuously pumped out by the 520 ℓ/s turbo pump P_2 on the main chamber. A specific buffer gas pressure is maintained in the linear trap vacuum system by flowmeter F_1, which adjusts the gas flow-rate according to the pressure at gauge G_3. Absolute pressure stability of $<$ 1 % is achieved.

In mixed buffer gas mode, mixing chambers T_1 and T_2 are individually filled with different buffer gases while recording the pressure on gauge G_3. In this manner, various buffer gas mixtures can be created before injection into the main vacuum system. The same procedure outlined above is then followed for injecting the gas into the system. In all of these procedures, valves V_7 and V_9 are left closed. P_1 is used for pumping the system down during bakeout, or for removing excess gas from the system after a mixture has been made.

5.1.5 Spectroscopy lasers

Spectroscopy of the lowest lying states of $^{136}Ba^+$ (see fig. 3.1) requires frequency stabilized lasers at 493 nm and 650 nm. External cavity diode lasers (ECDL)[13] are used for both of these wavelengths. The details of ECDL construction are beyond the scope of this thesis, and are discussed elsewhere [3]. The 650 nm laser is a TEC cooled

[8]Varian V70-LP
[9]SAES hot Zr alloy getter, model xxxx
[10]Pfeiffer RVC-300
[11]Nupro, bellows-sealed
[12]MKS baratron model xxx
[13]TOptica Photonics

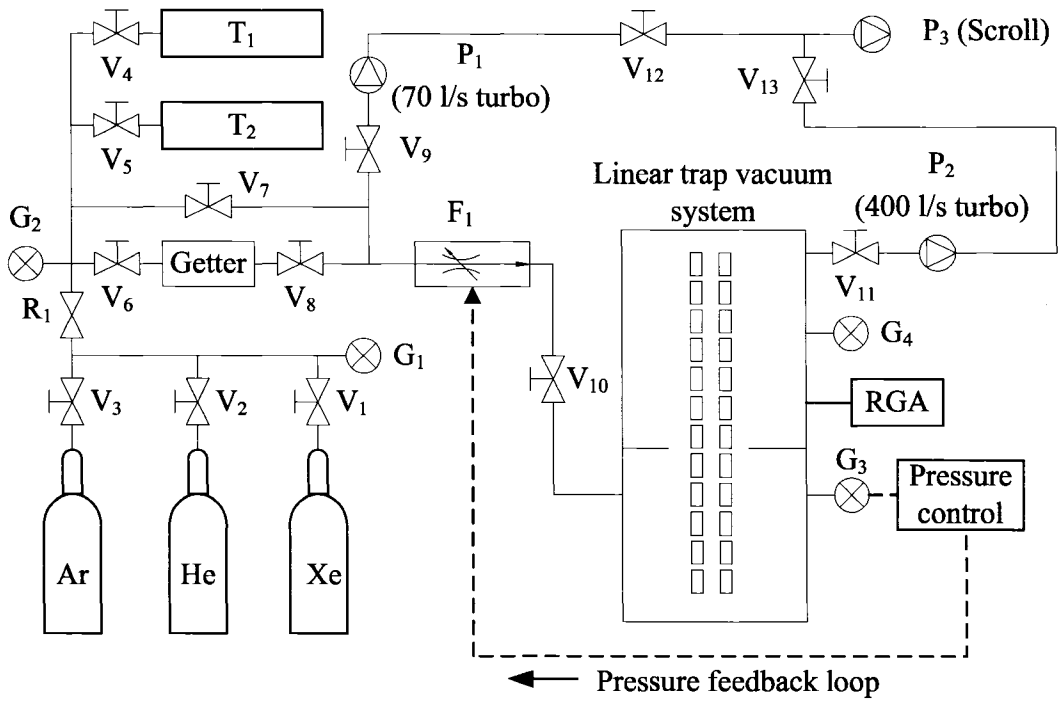

Figure 5.6: Schematic view of the buffer gas injection and control system.

20 mW diode, and the 493 nm laser is a TEC cooled, second harmonic generation 986 nm diode system. Both lasers are stabilized to < 20 MHz, with 10 mW of 650 nm light and 20 mW of 493 nm light, available for spectroscopy. These systems are shown schematically in fig. 5.7.

Both lasers are subject to absolute frequency drift, due to temperature variations in the room, diode aging, etc. To counteract these effects, both lasers are opto-galvanically locked to a Ba hollow cathode lamp[14], which provides a temperature independent 1 GHz resonance [48] (see fig. 5.7). The lasers are locked to the side of this resonance, which gives an absolute frequency reference good to ≤ 100 MHz, though this has not been explicitly measured and is suspected to be even better. Both lasers stay locked for ≥ 1 day as long as there are no drastic temperature excursions in the room.

The laser systems shown in fig. 5.7 reside on an 10'×4' standard optics table on air actuated vibration isolation mounts. The table is enclosed in a drape, and filtered

[14]Perkin-Elmer model xxx

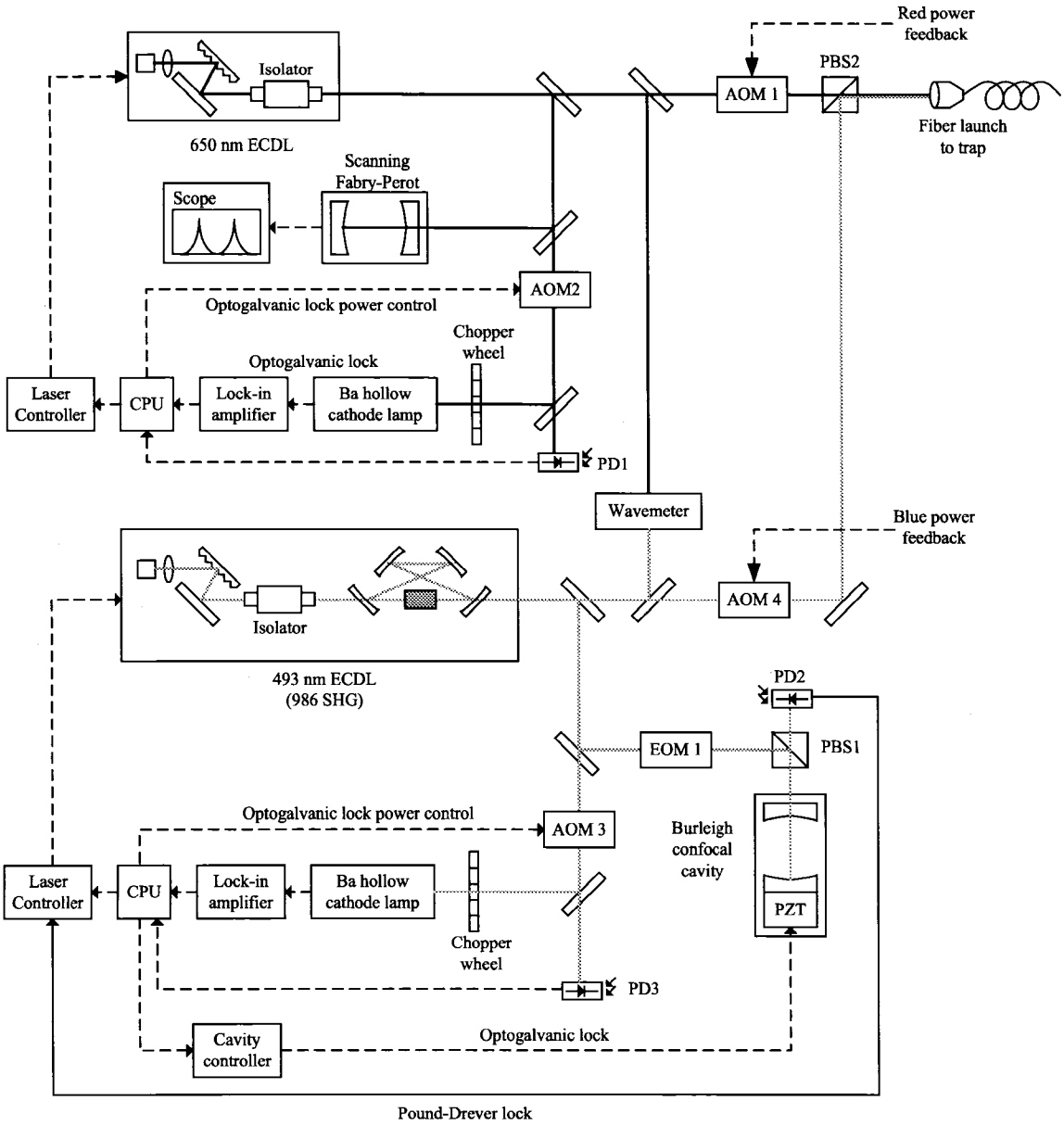

Figure 5.7: Schematic view of 493 nm and 650 nm laser systems including optogalvanic lock. Solid lines are laser paths and dashed lines are electrical paths.

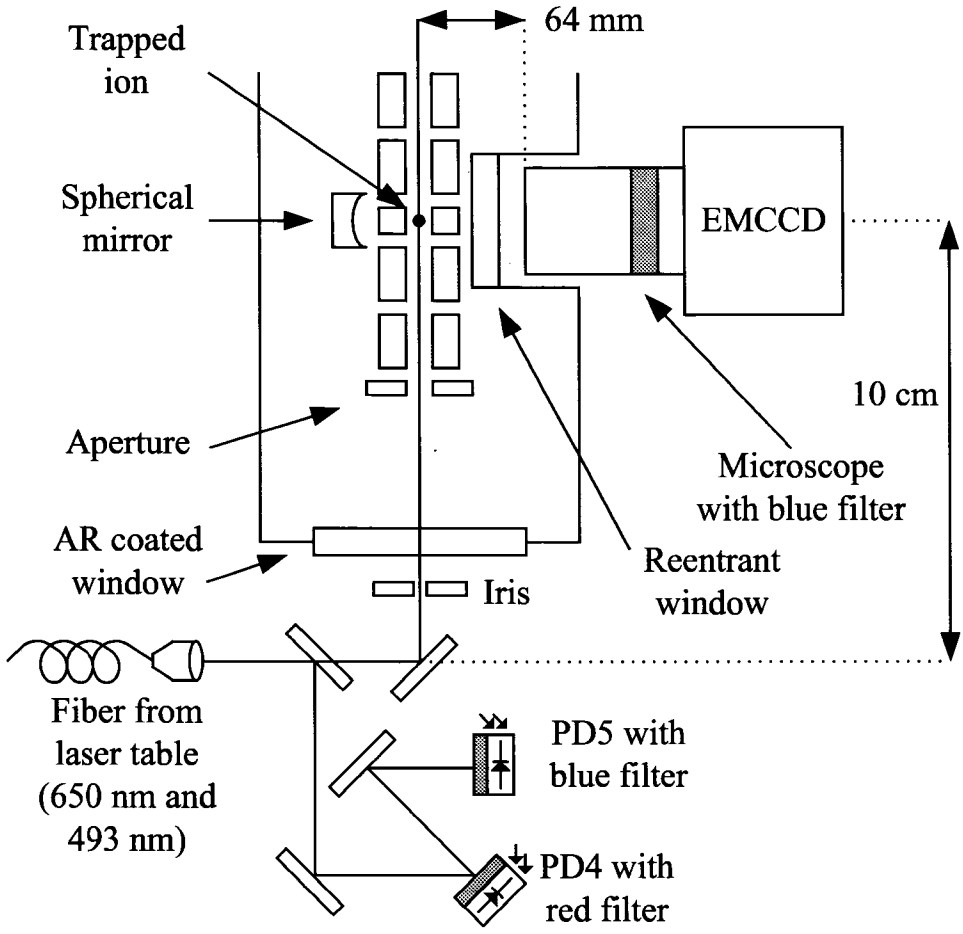

Figure 5.8: Schematic view of spectroscopy laser output optics at linear ion trap. Solid lines are laser beam paths.

air is continuously fed from above to minimize dust. The beams are combined and launched onto a single mode fiber, which completely decouples the laser and the linear ion trap systems. The beams exit the fiber on the output optics breadboard beneath the vacuum system as shown in fig. 5.8, and are focused by a microscope objective through an iris and AR coated (99.9%)[15] vacuum window on the bottom of the vacuum tank. The iris removes any beam halo or stray reflections that could enter the trap and cause an increase in scattered light. An additional aperture inside the vacuum system, at the bottom of the trap assists in beam alignment and further

[15]Standard quartz Conflat vacuum window, Super-V® AR coating by OptoSigma

scattered light reduction.

Both the red and blue lasers powers are controlled by feedback to the laser table from photodiodes at the linear ion trap. A small component of the beams is split off after the fiber launch before entering the trap, as shown in fig. 5.8. The power of each beam is read out on photodiodes PD4 and PD5, which is fed-back through a computer to acousto-optic modulators AOM1 and AOM4 (see fig. 5.7) on the optics table. The power of each laser at the trap is kept stable to a few percent.

5.1.6 Fluorescence detection and scattered light reduction

The resonance fluorescence at 493 nm and 650 nm produced by the ion at S_{14} is scattered into 4π. The fluorescence is read out by a microscope[16] whose first lens is placed 64 mm from the central plane of the trap, as shown in fig. 5.8. This is accomplished by positioning the microscope inside a reentrant vacuum window (see fig. 5.5), specially designed to be as close to S_{14} as possible. A spherical mirror, placed behind S_{14} inside the vacuum tank (see figs. 5.3 and 5.5), allows for the collection of fluorescence light by reflection that would otherwise be lost. This doubles this fluorescence rate, and improves the signal to noise ratio for single ion detection.

The microscope is outfitted with a blue filter in order to reject 650 nm light. Some background from scattered light is due to the fact that the lasers co-propagate out of the fiber through the same collimating lens, so either the blue or the red can be focused at S_{14}, but not both. If the blue is focused, the red beam causes scattered light, and vice versa. The loss of the 650 nm fluorescence signal due to this filter is more than compensated for by the reduction of scattered 493 nm laser light.

Individual ions are imaged on an electron multiplied CCD camera (EMCCD)[17] and read out by a computer. The EMCCD is mounted on an x-y-z stage for precise positioning. The camera is TEC cooled to -80 °C, with a back-illuminated CCD chip. Each pixel is 16 μm^2. The TEC cooling reduces the shot noise, while the electron multiplication effectively eliminates the read noise. This allows for single photon/pixel sensitivity, with a quantum efficiency $> 90\%$ at 493 nm. In order to further reduce

[16] Infinity Optics model xxx with a xxx objective
[17] Andor model iXon$^{EM}+$

readout noise, the pixels are binned together before digitization in 8×8 groupings. While this reduces the readout noise by a factor of 64, it also decreases the resolution by the same amount. Finally, the entire trapping region, including the electrodes, is imaged onto the EMCCD. Only a small region of interest (ROI) containing the ion is recorded, which drastically reduces the background rate when observing a single ion. The camera is read out every 5 s, during standard running conditions. The major technical efforts involved in scattered light reduction are listed here.

- AR coated fused silica vacuum window to reduce intensity of multiple 493 nm laser beam foci in the trap (from multiple reflections off of the input window and other optics faces)
- Blue filter on microscope to reduce all light except 493 nm
- Optical mounts with small lever arms for all mirrors and components on the output optics breadboard (breadboard mounted below the trap with beam focusing and power measurement, shown in fig. 5.8)
- High quality cleave on fiber face
- Iris just before quartz beam entrance window on vacuum system, to eliminate halos and back reflections
- High quality beam steering mirrors at linear ion trap

A photo of the entire system is shown in fig. 5.9.

5.2 Simulation of a single trapped ion in a buffer gas

A single Ba^+ interacting with a buffer gas in the linear trap is simulated in order to determine the optimal operating parameters, as well as the type and pressure of buffer gas needed to isolate a single ion for spectroscopy. This Monte Carlo is implemented using the software package SIMION 7.0 [49], which propagates the ion in RF and DC

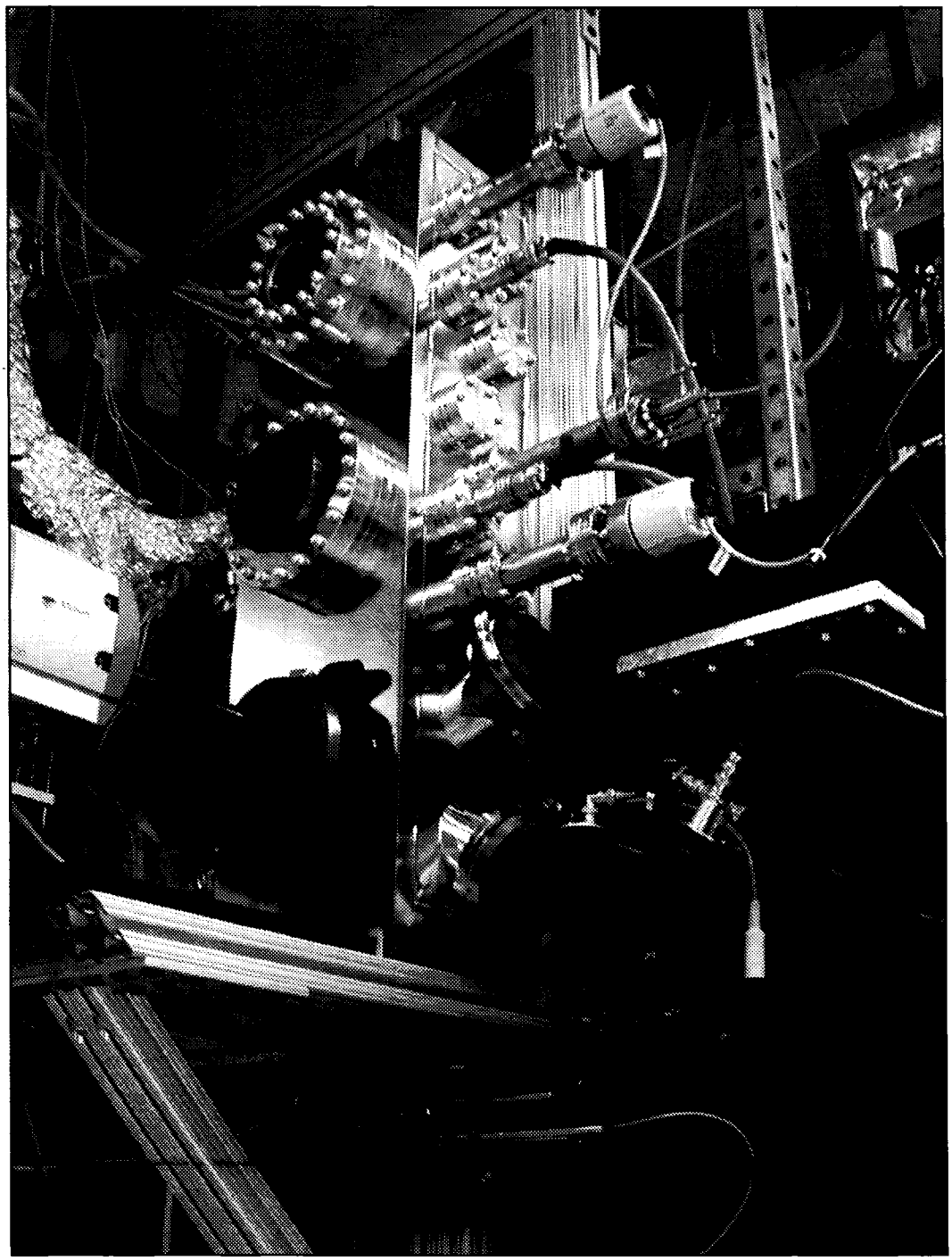

Figure 5.9: Photo of linear ion trap vacuum system.

fields created by user generated electrode geometries. The full geometry of the linear ion trap is built in SIMION, and buffer gas collisions are implemented using an HS1 model (see §4.5) [50].

Buffer gas collisions are implemented by specifying a mean free path λ, buffer gas mass m_B, and buffer gas temperature T_B. As the ion propagates through the trap, the probability that a collision occurs after a time t is given by the cumulative distribution function of an exponential distribution,

$$P(t) = 1 - e^{-vt/\lambda} \tag{5.3}$$

where v is the ion's instantaneous velocity. After each time step Δt, a random number between zero and one is chosen. This number is compared to $P(t)$, where t is the time since the last collision. If this number is greater than $P(t)$ a collision occurs, otherwise the ion trajectory is stepped forward by Δt. When a collision occurs, the ion's velocity is adjusted assuming an elastic collision between the ion and a buffer gas atom. The velocity of the buffer gas atom is chosen randomly from a Maxwell-Boltzmann distribution with temperature T_B.

The mean free path used in the simulation is calculated using the Langevin scattering model (eqn. 4.45), and is kept constant throughout the simulation. The following DC potentials, in volts, are set,

$$U_{DC} = \{+10, +10, +10, -0.4, -0.5, -0.6, ... - 1.3, -1.4, -8, -1.4, +10\} \tag{5.4}$$

where the first element corresponds to S_1, and the last element corresponds to S_{16}. The first few potentials are set to +10 V due to a constraint in the number of adjustable electrodes in SIMION. This has no effect on the cooling of an ion to the potential minimum. A single ion is created in S_4 with an initial kinetic energy of 10 eV. S_{14} is the trapping segment, and the high potentials on S_1-S_3 and S_{17} are chosen to confine the ion along the z-axis as it cools. The buffer gas temperature is 293.15 K.

In figs. 5.10-5.12, the ion trajectory is plotted as a function of time for three different buffer gases: He, Ar, and Kr. In each of these plots, the mean free path is

chosen to be 7.5 mm, corresponding to buffer gas pressures $P_{He} = 1.0 \times 10^{-2}$ torr, $P_{Ar} = 3.7 \times 10^{-3}$ torr, and $P_{Kr} = 3.0 \times 10^{-3}$ torr. In each case, (a) and (c) are time series of the ion's kinetic energy, whereas (b) and (d) are the ion's longitudinal (z) coordinate. Horizontal dotted lines are drawn at the DC walls of the trap, and at the trap minimum. In the case of He buffer gas cooling, the momentum transfer per collision is very small. The cooling is inefficient and slow ($\sim$ 10 ms for a 10 eV ion cooled to 1 eV) compared to other buffer gases, but still fast on the time scales of interest in this experiment ($\geq$ 1 sec). At this pressure of He, the ion bounces back and forth along the longitudinal axis of the trap before finally cooling into the trap minimum. Cooling collisions are visible in both 5.10a and 5.10c as downward steps in the kinetic energy.

In Ar, an ion with the same initial kinetic energy is cooled to 1 eV in $\sim$ 500 μs. The average momentum change of the ion per collision is larger than for He. This allows for more efficient cooling, as well as more RF heating than for He. Many more heating collisions are visible in fig. 5.11c, increasing the probability of unloading per collision from the trap. This is why He is most often used as a cooling gas.

In Kr, as single collision initially cools the ion from 10 eV to 1 eV. The ion subsequently traverses the trap minimum and is caught in the flat potential of a neighboring trap segment. Eventually, collisions cool the ion into the trap minimum, where a heating collision causes unloading from the trap. Whereas Kr is efficient at cooling the ion, unloading is much more likely compared to He or Ar.

In addition to these cases, Ba^+ in a Xe buffer gas is simulated. This case exhibits behavior similar to that of Ba^+ in Kr, except that the average time to unloading is much shorter. Xe alone evidently cannot be used as a cooling gas due to the large average ion-neutral momentum transfer, which causes RF heating and unloading from the trap.

The buffer gas cooling processes described here occur on time-scales $\leq$ 1 s. He is the least efficient cooling gas, but allows for long residence times due to the very small average momentum transfer per ion-neutral collision. Ar is a much more efficient cooling gas, though individual collisions perturb the ion's momentum more than in the case of He. This likely leads to a higher unloading rate when compared to He,

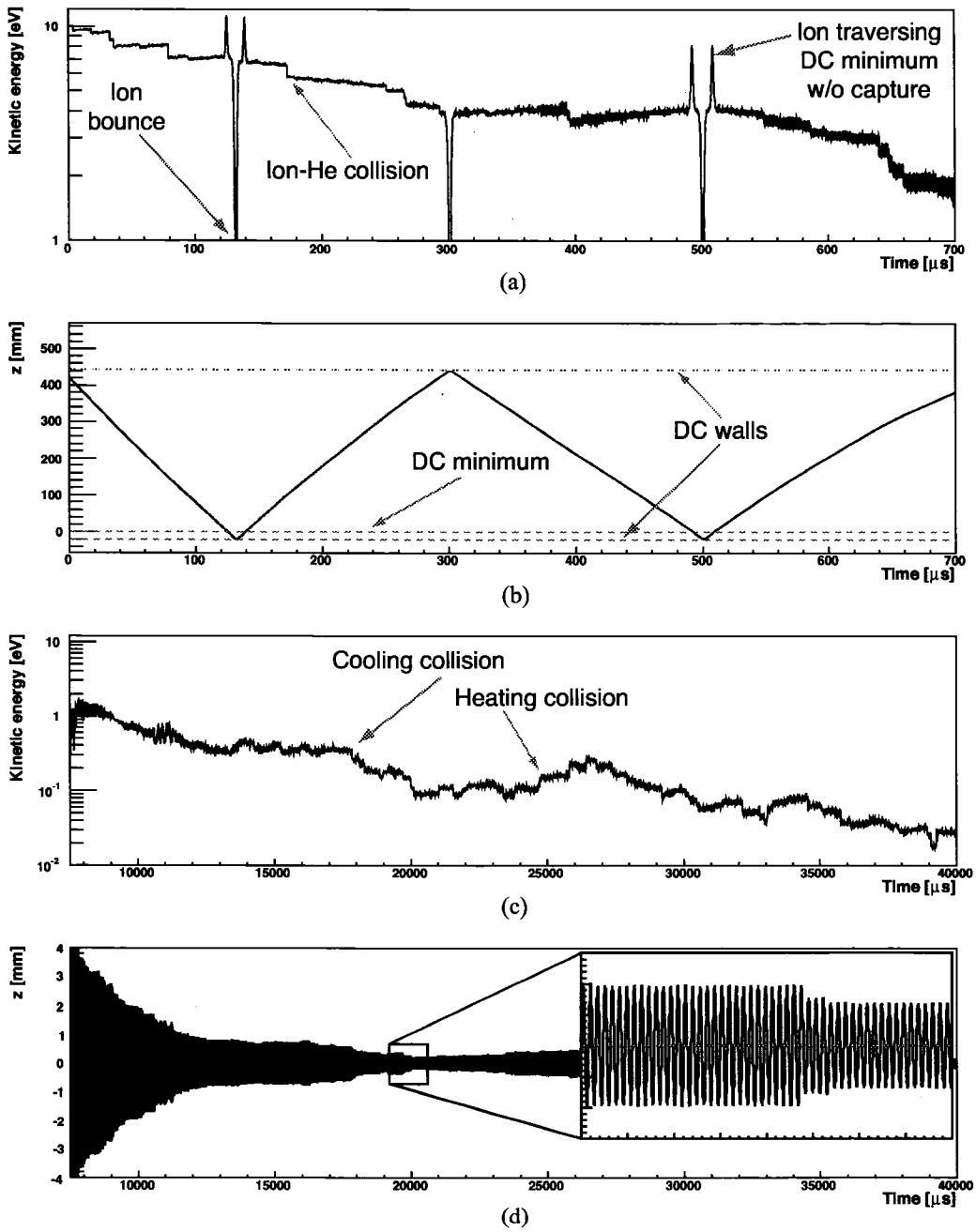

Figure 5.10: Simulation of a single $^{136}Ba^{+}$ in He ($\lambda = 7.5$ mm). The collisional cooling of the ion immediately after release is shown in (a). The z trajectory of the ion is shown in (b); this pressure of He is not high enough to cool the ion enough to be trapped at the DC minimum on the first pass, so the ion bounces longitudinally. In (c), the ion has cooled into the DC well at S_{14}, though is still cooling to the buffer gas temperature. In (d), the z trajectory of the ion trapped in S_{14} is shown.

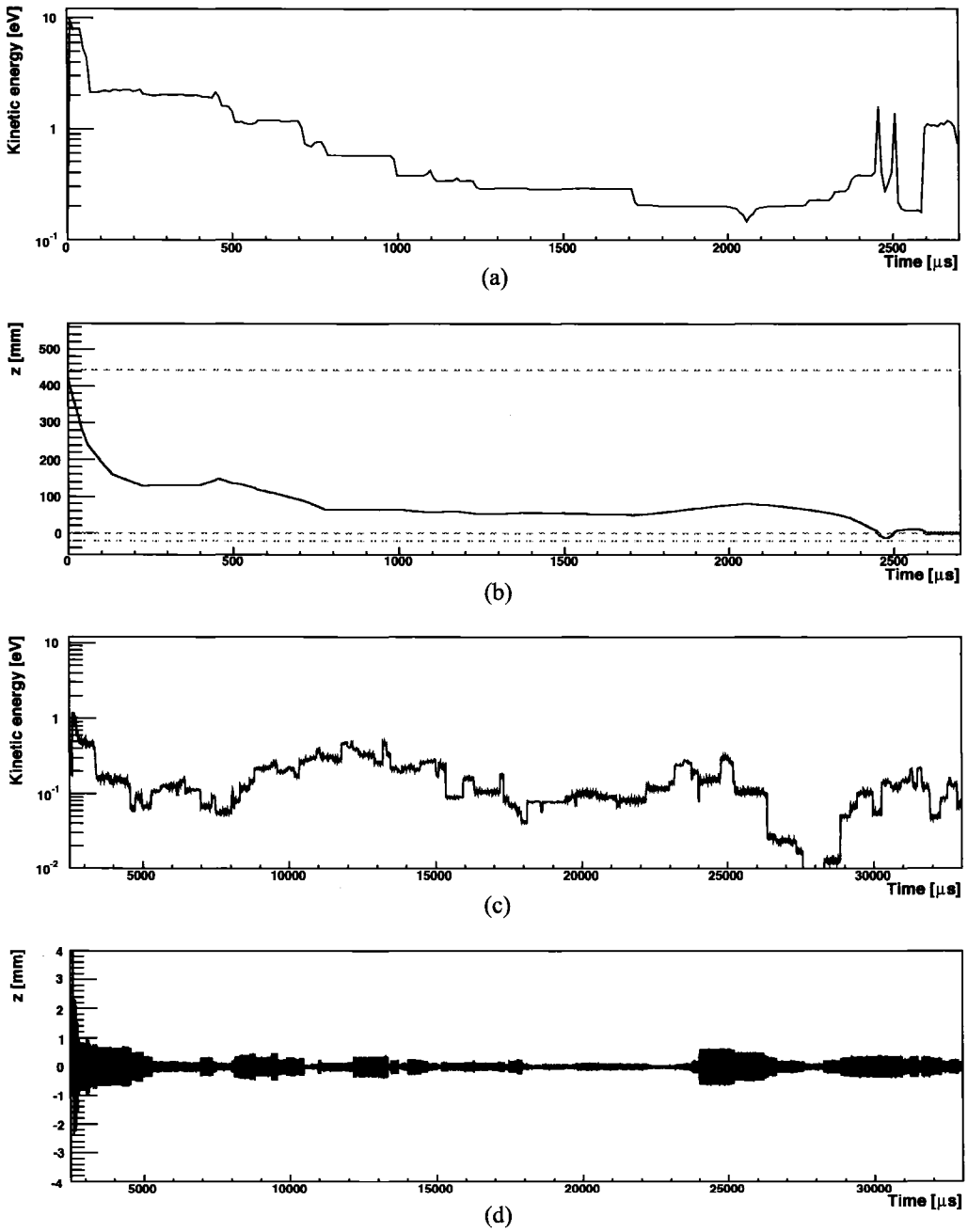

Figure 5.11: Same as figure 5.10, but for Ar ($\lambda = 7.5$ mm). The ion cools much faster into the DC well compared to He, without bouncing. The trajectory and energy excursions due to collisions are also larger.

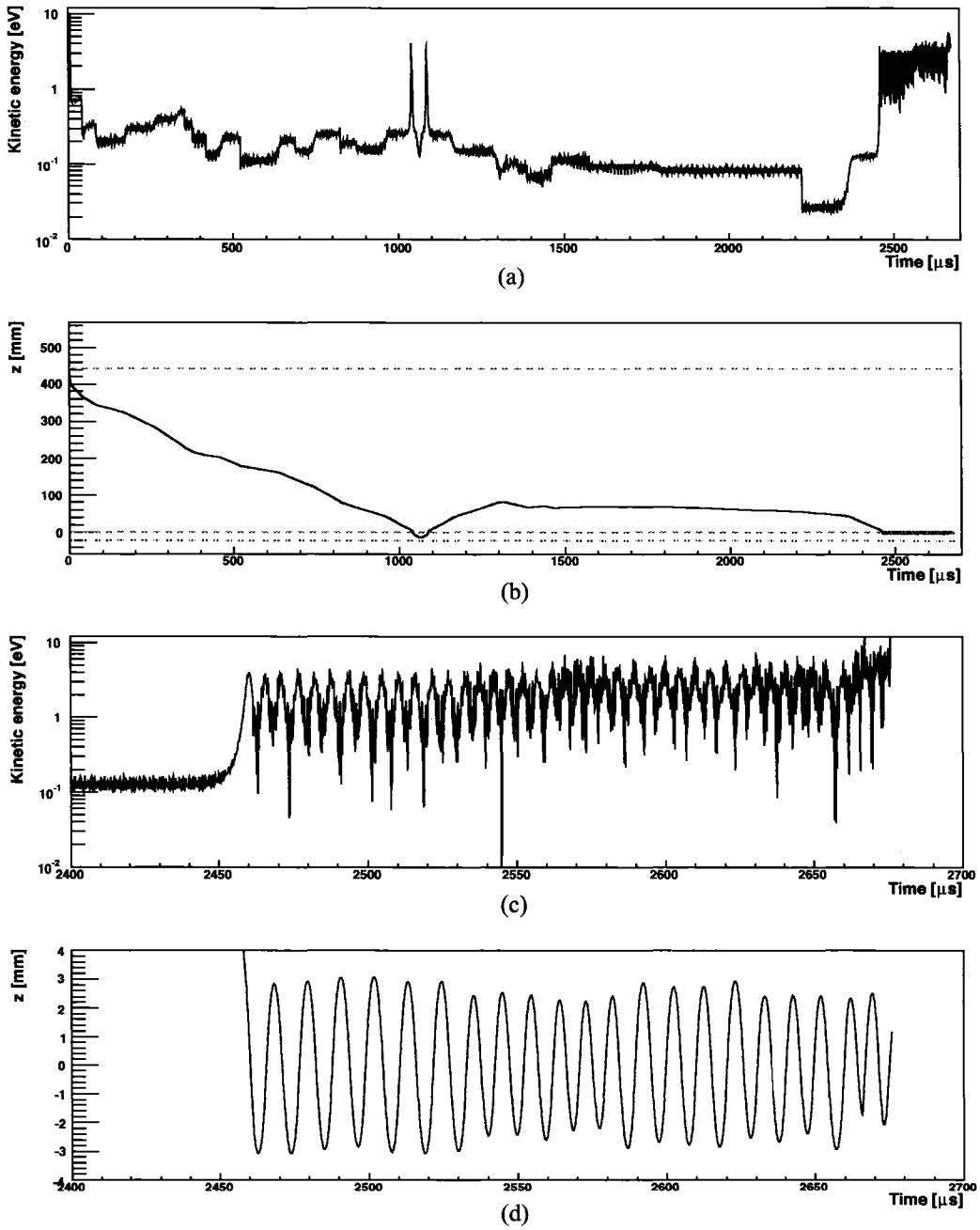

Figure 5.12: Same as figure 5.10, but for Kr ($\lambda = 7.5$ mm). The ion is initially cooled from 10 eV to 1 eV in a single collision. Eventually, the ion is heated by a collision, causing it to eject from the trap at $t = 2.675$ ms.

though computational constraints only allow for simulations of $\sim$ 1 s of real time. Unloading of the Ba^+ in He or Ar is not observed in these simulations. Kr and Xe cannot be used to trap Ba^+, though mixtures of He and Xe, at low Xe concentration, are shown to work in §5.3.

5.3 Results

Individual ions are trapped and observed via resonance fluorescence. The average lifetime of single ions in He, Ar, and He/Xe mixtures is measured as a function of pressure. A simple model describing the unloading behavior of ions in He/Xe mixtures is presented and fit to experimental data. In addition, the red laser frequency is scanned over the resonance of a single ion at different He pressures to measure the Doppler temperature of a single ion.

5.3.1 Observation of individual ions in a buffer gas

A few ions (< 10) are loaded into the trap with the methods presented in §5.1 at 4.4×10^{-3} torr He. The ions thermalize with the He at S_{14}, and their resonance fluorescence observed. The blue and red laser powers are set to 65 μW and 200 μW, respectively. A 5 s EMCCD false color image of the resonance fluorescence from one ion is shown in fig. 5.13. In this image, the brightness of each pixel is proportional to the number of incident blue photons. The ion is evident from the grouping of bright pixels in the central ROI. The bright vertical bars on either side of the image are due to scattered 493 nm laser light off the electrodes. The vertical size of the region imaged is 4 mm.

The 493 nm fluorescence signal, defined as the sum of the pixels in the ROI shown in fig. 5.13, is recorded in 5 s intervals as the ions eject from the trap over time, shown in fig. 5.14. The y-axis of the plot is fluorescence rate in arbitrary units of EMCCD counts, zero-supressed since these values change depending on the scattered light conditions due to laser alignment in a given experiment. Zero (background light level), one, two, three, and four ions are clearly visible in the time series. The

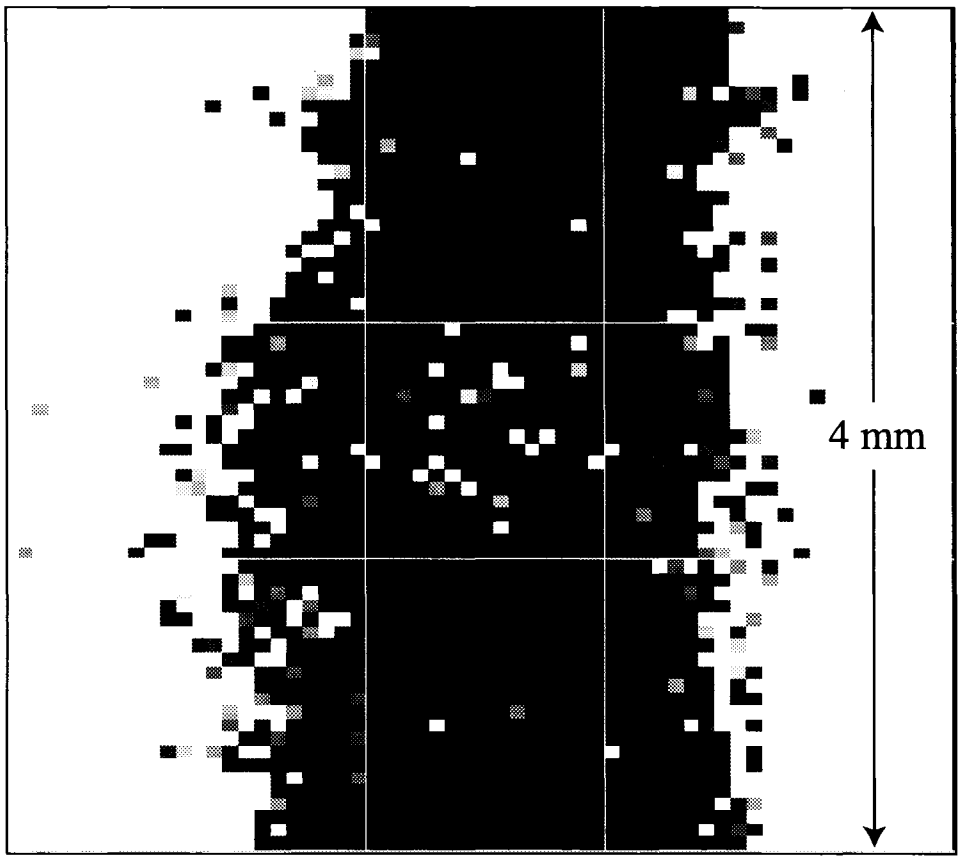

Figure 5.13: EMCCD false-color image of a single ion, taken with a 5 s integration in 4.4×10^{-3} torr He. The ion fluorescence signal is evident by the grouping of lighter pixels in the central ROI.

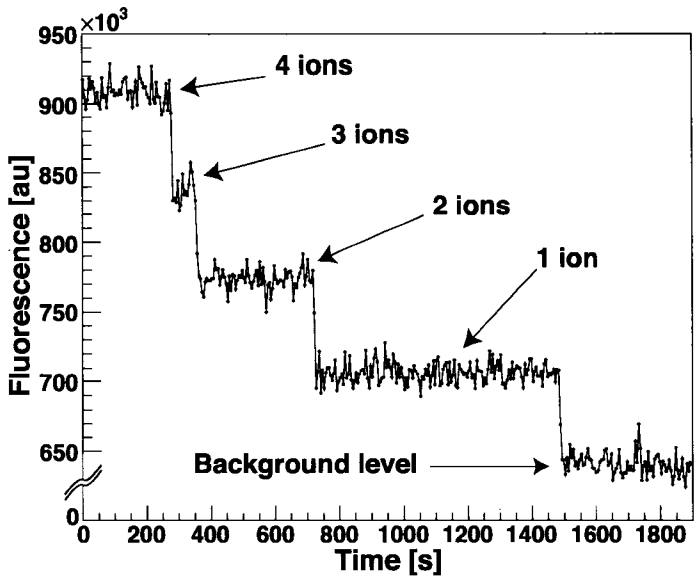

Figure 5.14: 493 nm ion fluorescence rate time series of individual ions in the trap at 4.4×10^{-3} torr He. Ions unload, causing quantized drops in the fluorescence rate. Each point represents 5 s of integration with the EMCCD.

background rate is due to scattered laser light and the camera baseline noise.

This fluorescence time series is histogrammed, and fit to a sum of four Gaussians with no fixed parameters in fig. 5.15. The three ion peak is excluded from the fit, due to lack of statistics. The χ^2/dof of the fit is 62/54, indicating the distributions are well described by Gaussian distributions. The best fit central values and statistical errors are plotted versus ion number in fig. 5.16. The errors are all smaller than the actual drawn circles in the plot. This data is fit to a line, with a $\chi^2/\text{dof} = 0.06/2$. The fluorescence is linear with the number of ions in the trap, as expected.

The single ion fluorescence signal to noise (S/N) is defined naively as

$$S/N = \frac{\langle S\rangle - \langle B\rangle}{\sigma_B} \tag{5.5}$$

where $\langle S\rangle$ is the average single ion fluorescence rate (central value of second peak in fig. 5.15), $\langle B\rangle$ is the average background rate with no ion in the trap (central value of first peak in fig. 5.15), and σ_B is the Gaussian width of the background signal.

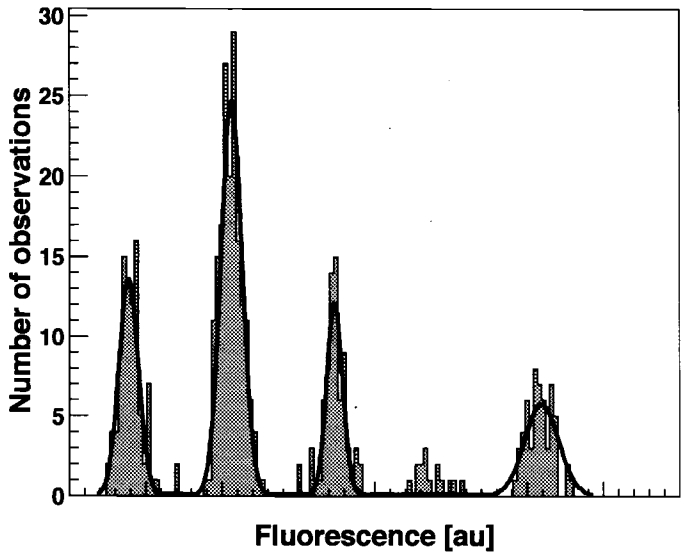

Figure 5.15: Projection of time quantized ion fluorescence time series in fig. 5.14. The spectrum is fit to four Gaussians, with a $\chi^2/\text{dof} = 62/54$. The three ion peak is not fit, due to a lack of statistics.

This quantity is found to depend heavily on the scattered light conditions during data taking, whereas the dependence upon buffer gas is a minor effect and has not been studied. The S/N for the data shown in fig. 5.14 is 10.6, for integration times of 5 s per sample. The single ion S/N in all buffer gasses, and at all pressures studied is $\gg 1$. Fluorescence quantization is also observed at pressures between 10^{-5} and 1 torr He, with no significant change in the signal to noise ratio. Similarly, quantization is observed in Ar and He/Xe mixtures.

5.3.2 Single ion unloading rates in He and Ar

Individual ions unload from the trap spontaneously, as shown in fig. 5.14. This is most likely due to a collisional process, such as RF heating or capture on an impurity (see §4.4 and §5.2). For a given set of experimental conditions (e.g. buffer gas type, pressure, etc.), unloading occurs at a uniform rate R and the probability of unloading per buffer gas collision is constant. It follows that the number of unloading events,

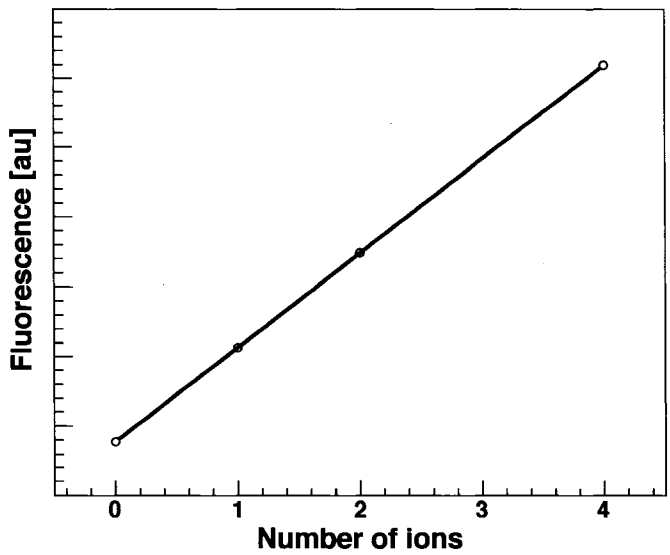

Figure 5.16: Linearity of the observed fluorescence rate for the data shown in figs. 5.14-5.15 with the number of ions stored in the trap. Statistical errors are included only, and are smaller than the data points (open circles). The data is fit to a line, with a $\chi^2/\text{dof} = 0.06/2$.

n, in a time interval t is Poisson distributed with mean Rt. The probability of n unloading events after time t is then

$$\mathcal{P}_U(t, R; n) = \frac{(Rt)^n e^{-Rt}}{n!} \tag{5.6}$$

The probability of observing $n = 0$ unloading events in a time t is

$$\mathcal{P}_U(t, R; n = 0) = e^{-Rt} \tag{5.7}$$

where R^{-1} is the exponential decay time constant. The probability of a single ion surviving in the trap therefore decreases exponentially as a function of time.

Using this model, the average unloading rate (inverse of the lifetime), of a single ion is measured in different buffer gases as a function of pressure. A few (< 10) ions are loaded into the trap, and their ejection observed in real time, as in fig. 5.14. Once a single ion is left in the trap, its residence time is measured until it unloads. This sequence is repeated multiple times for each buffer gas, at different pressures. In order to attain good fluorescence signal to noise, the EMCCD integration time is set to 5 s. This sets the minimum lifetime measurement $t_{min} = 5$ s. This lower cutoff is easily accounted for by using a log-likelihood method to determine the most probable value of R given a set of lifetime measurements, as explained in appendix B.

This analysis is performed in He, Ar, and He/Xe mixtures at different pressures. The He/Xe data is described in §5.3.3. The measured unloading rates R of a single ion in He and Ar as a function of pressure are shown in fig. 5.17. Each data point consists of approximately 25 measurements of the lifetime of one ion.

These data are fit to a linear model

$$R = C_0 P + C_1 \tag{5.8}$$

where C_0 and C_1 are coefficients, and P is the buffer gas pressure in torr. This model assumes the single ion unloading rate, R, scales linearly with pressure. This is physically motivated for the following reasons. First, if the the ion ejects due to RF heating collisions (see §4.4), the frequency of these collisions will scale with

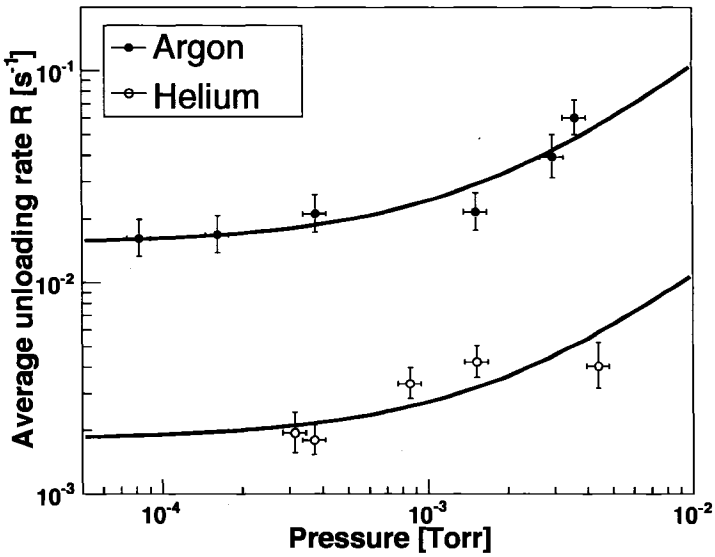

Figure 5.17: Measured average single Ba^+ unloading rates, R, in He and Ar buffer gases as a function of pressure. The data are fit to a model described in the text.

Parameter	He	Ar
χ^2/dof	7.6/3	4.1/4
C_0	0.8 ± 0.3	8 ± 2
C_1	$(1.8 \pm 0.3) \times 10^{-3}$	$(1.5 \pm 0.2) \times 10^{-2}$

Table 5.2: Fit results and χ^2/dof of linear model to He and Ar unloading rate data.

the buffer gas pressure. Second, the ion can unload due interactions with impurities (charge transfer, momentum transfer, molecule formation, etc.). If these impurities are contained within the buffer gas, the frequency of these collisions will scale with the buffer gas pressure. C_0 therefore contains information about the cross-section of these processes. It is also possible that these impurities are due to some other source (e.g. ion gauges or outgassing from the walls of the vacuum system). The unloading rate due to this source of impurities is independent of the buffer gas pressure. C_1 accounts for this second effect. The fit results for He and Ar are shown in table 5.2.

It is evident from this data that the unloading rate in He is significantly lower than in Ar ($\sim 10\times$). This is consistent with a higher probability of unloading per

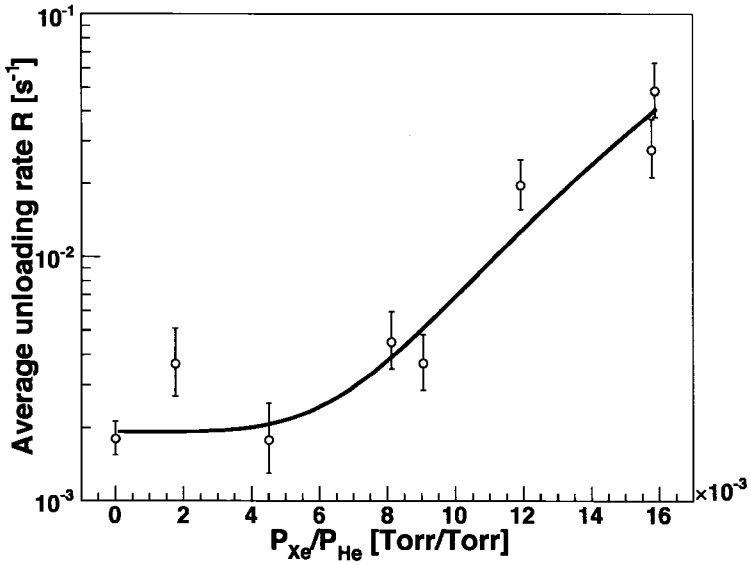

Figure 5.18: Measured average single ion unloading rates, R, in He/Xe mixtures at various Xe concentrations. The data are fit to a model, described in the text. The total pressure is 3.7×10^{-4} torr.

collision with buffer gas atoms of increasing mass.

5.3.3 Single ion unloading rates in He/Xe mixtures

The same measurement procedure described in §5.3.2 is used to measure single ion unloading rates in He/Xe mixtures, at low Xe concentrations. This is a way of investigating the destabilizing effects of Ba^+-Xe collisions, while retaining the ability to observe a single ion. The total pressure is kept constant at 3.7×10^{-4} torr, and the Xe concentration is varied. The measured unloading rates versus Xe concentration are shown in fig. 5.18. The concentration of Xe is measured by a cold cathode gauge and residual gas analyzer. The unloading rate increases with higher Xe concentrations, as expected if the unloading mechanism is RF heating, or some other kinematic effect (see §4.4). The data are fit to a model assuming the unloading is due to multiple consecutive RF heating collisions between the Ba^+ and Xe atoms.

Given a single ion in a He/Xe buffer gas mixture with partial pressures P_{He} and

P_{Xe}, the time intervals between Ba^+-He and Ba^+-Xe collisions are each exponentially distributed with collision rate constants $R_{\mathrm{He}} = C_{\mathrm{He}}P_{\mathrm{He}}$ and $R_{\mathrm{Xe}} = C_{\mathrm{Xe}}P_{\mathrm{Xe}}$, respectively. In both cases, the collision physics details are absorbed into the coefficients $C_{\mathrm{He,Xe}}$. The probability that a Ba^+ collides once with a Xe atom in a time t is then (see eqn. 5.3)

$$\mathcal{P}_C^{\mathrm{Xe}}(t) = 1 - e^{-R_{\mathrm{Xe}}t} = 1 - e^{-C_{\mathrm{Xe}}P_{\mathrm{Xe}}t} \tag{5.9}$$

The distinction is now made between the probability of any Ba^+-Xe collision occurring (eqn. 5.9), versus the probability of a Ba^+-Xe collision occurring that causes RF heating of the ion. Only a small fraction, α_{RF}, of the total Ba^+-Xe collisions are assumed to heat the ion. Therefore, the probability that a Ba^+-Xe RF heating collision occurs after a time t is

$$\mathcal{P}_{RF}^{\mathrm{Xe}}(t) = 1 - \exp\left(-\alpha_{RF}R_{\mathrm{Xe}}t\right) \tag{5.10}$$

in terms of the Xe partial pressure, this becomes

$$\mathcal{P}_{RF}^{\mathrm{Xe}}(t) = 1 - \exp\left(-\alpha_{RF}C_{\mathrm{Xe}}P_{\mathrm{Xe}}t\right) \tag{5.11}$$

As evident from the magnitude of the ejection rates in fig. 5.18, compared to the Ba^+-Xe collision frequency ($\sim$ kHz), a single Ba^+-Xe RF heating collision is not sufficient, on average, to unload an ion. Instead, unloading may require multiple consecutive Ba^+-Xe heating collisions on a timescale less than the Ba^+-He collision time, R_{He}^{-1}. The probability of n Ba^+-Xe heating collisions during a time $t \leq R_{\mathrm{He}}^{-1}$ is

$$\prod_n \mathcal{P}_{RF}^{\mathrm{Xe}}(t \leq R_{\mathrm{He}}^{-1}) = \left[1 - \exp\left(-\alpha_{RF}\frac{C_{\mathrm{Xe}}P_{\mathrm{Xe}}}{C_{\mathrm{He}}P_{\mathrm{He}}}\right)\right]^n \tag{5.12}$$

For $P_{\mathrm{Xe}} \ll P_{\mathrm{He}}$,

$$\prod_n \mathcal{P}_C^{\mathrm{Xe}}(t \leq R_{\mathrm{He}}^{-1}) \approx \left(\frac{\alpha_{RF}C_{\mathrm{He}}P_{\mathrm{Xe}}}{C_{\mathrm{Xe}}P_{\mathrm{He}}}\right)^n \tag{5.13}$$

The rate of this process occurring is proportional to the n-th power of the Xe concentration. The ejection rate data in fig. 5.18 is fit to the following three parameter

Parameter	Value
n	4.5 ± 0.6
C_0	$(1.8 \pm 0.3) \times 10^{-3}$
C_1	30 ± 4
χ^2/dof	8.6/5

Table 5.3: Fit results and χ^2/dof of collisional unloading model to He/Xe data.

function,

$$R\left(\frac{P_{\mathrm{Xe}}}{P_{\mathrm{He}}}\right) = C_0 + C_1\left(\frac{P_{\mathrm{Xe}}}{P_{\mathrm{He}}}\right)^n \tag{5.14}$$

where C_0 is the unloading rate due to He alone, C_1 represents a combination of the Ba^+-Xe and Ba^+-He RF heating collision physics, and n is the average number of RF heating collisions required to unload an ion. The fit results are listed in table 5.3.

5.3.4 Temperature measurement of a single ion

The Doppler temperature of a single ion in He is measured by scanning the red laser frequency over the Doppler broadened $6P_{1/2} \leftrightarrow 5D_{3/2}$ resonance. The 493 nm fluorescence is monitored, while the blue frequency is kept locked on resonance. This procedure is repeated at different He pressures. The ion's temperature is extracted by fitting the measured fluorescence intensity spectrum to a Voigt profile (eqn. 3.41). This fit assumes that the lineshape is a power broadened Lorentzian profile (see §3.2), convolved with a Maxwellian velocity distribution along the laser axis (see §3.4).

Before the spectra can be fit to a Voigt profile, the power broadening of the $6P_{1/2} \leftrightarrow 5D_{3/2}$ transition due to the red laser must be measured (see §3.2). This is accomplished by measuring the saturation curve of a single ion, shown in fig. 5.19 taken at 8.6×10^{-4} torr He. This curve is pressure independent. The saturation curve is measured by monitoring the 493 nm fluorescence, with both lasers locked on resonance, while sweeping the red laser power. The curve is fit to

$$I(P) = I_0\left(\frac{P/P_{sat}}{1 + P/P_{sat}}\right) + \beta \tag{5.15}$$

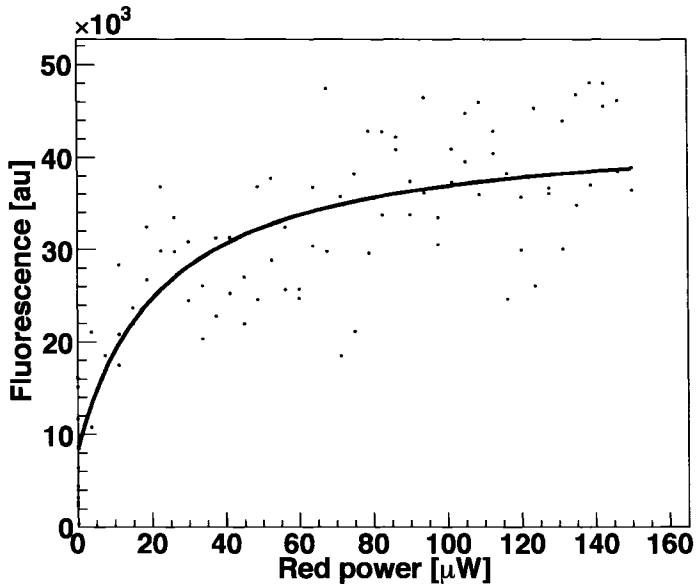

Figure 5.19: Single ion saturation curve of the $6P_{1/2} \leftrightarrow 5D_{3/2}$ transition, at 8.6×10^{-4} torr He.

where P is the red laser power in μW, P_{sat} is the fit saturation power, I_0 is an overall scaling of the observed fluorescence intensity, and β is an offset due to camera baseline noise and scattered light (see eqn. 3.34). The fit value of the saturation power is $P_{sat} = 23 \pm 8$ μW.

A few spectra and fits to Voigt profiles at different He pressures are shown in fig. 5.20. The fit Doppler temperature is plotted versus He pressure in fig. 5.21. The two data sets are temperature measurements made on different days, at different laser laser power settings. This was done to investigate any possible systematic effects, such as higher-than-expected power broadening, dependence on the lock-points of either laser, buffer gas purity, etc. No large systematic effect, compared to the statistical errors, are visible. The average temperature is found by fitting all of the data shown to a zeroth-order polynomial. This is equivalent to computing the average of all measurements, weighted by each measurement's statistical error. The average temperature is 256 ± 10 K.

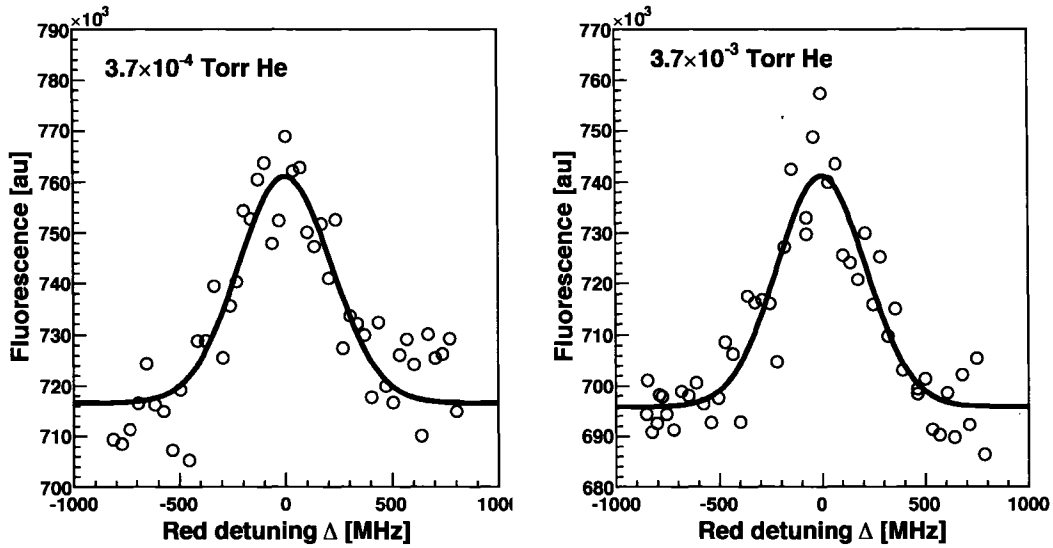

Figure 5.20: Single ion fluorescence spectra as a function of red detuning Δ_R, at 3.7×10^{-3} and 3.7×10^{-4} torr He.

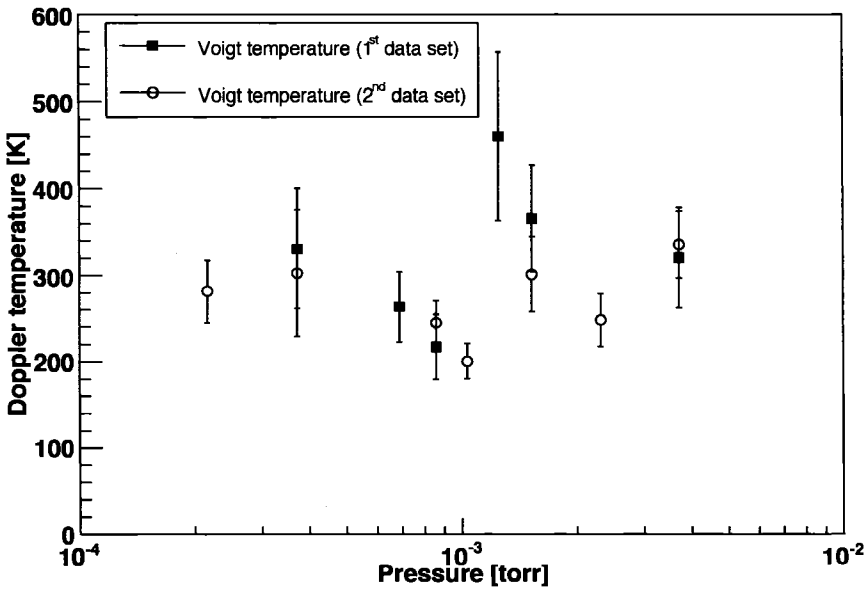

Figure 5.21: Fit ion temperatures assuming a Maxwell-Boltzman velocity distribution along the laser axis. The mean temperature is 256 ± 10 K, including only statistical errors. The two data sets are from different days, with different laser lock-points and red laser powers.

Chapter 6

Ionizing radiation in liquid Xe

Liquid Xe (LXe) was first investigated in the 1960s as a detector of ionizing radiation. This was motivated by the problem of poor spatial resolution in spark chambers and multiwire proportional counters [51]. It is useful as a detector in this manner because of it's high atomic number, density, electron mobility, and ionization/scintillation yields [52]. Xe becomes liquid at $\sim$ 170 K, at a vapor pressure of $\sim$ 1100 torr. Details of the interactions of ionizing radiation with LXe are out of the scope of this work, but much progress has been made in understanding the multiple physical processes that produce the two fundamental measurable quantities: ionization electrons and scintillation photons. Thorough theoretical and experimental discussions and can be found in [53], and references therein. An exhaustive review of the calorimetric and optical properties of LXe can be found in [54]. The basic properties of LXe relevant to the detection of ionizing radiation at the keV energy scale are discussed here.

6.1 Energy deposition

Ionizing radiation (e.g. γ, X-rays, β^-, α, etc.) with an energy in the keV range, passing through a LXe volume, deposits energy predominantly by producing electron-hole pairs and excited Xe states. Some energy is also deposited as Cerenkov radiation, phonons, etc., however at this energy scale, these effects are negligible. This process occurs as

- Incoming radiation scatters off Xe atoms, creating δ-electrons, holes (Xe^+), and excited states (Xe^*).
- δ-electrons further ionize, creating more daughter electrons, Xe^+, and Xe^*, repeating the process described in the first step. This creates a cascade of electrons with decreasing kinetic energy.
- The Xe^* and Xe^+ combine with neutral Xe and ionization electrons from the first two steps, forming excited dimer states (Xe_2^*). These states promptly de-excite ($\sim$ ns), emitting 175 nm scintillation photons and heat (infrared photons).

The scintillation process described in the last step occurs in two ways [55]. The first process (exciton de-excitation) involving Xe^* is

$$\begin{aligned} Xe^* + Xe &\rightarrow Xe_2^* \\ Xe_2^* &\rightarrow 2Xe + h\nu \end{aligned} \tag{6.1}$$

The second process (recombination), involving Xe^+ and ionization electrons from the cascade is

$$\begin{aligned} Xe^+ + Xe &\rightarrow Xe_2^+ \\ Xe_2^+ + e^- &\rightarrow Xe^{**} + Xe \\ Xe^{**} &\rightarrow Xe^* + \text{heat} \\ Xe^* + Xe &\rightarrow Xe_2^* \\ Xe_2^* &\rightarrow 2Xe + h\nu \end{aligned} \tag{6.2}$$

where *heat* is energy lost as an infrared photon, and $h\nu$ is a 175 nm scintillation photon. Ordinarily, all electrons will recombine or thermalize in the LXe. If, on the other hand, a static drift field $\mathcal{E}_D$ is applied across the LXe volume, the recombination process (eqn. 6.2) is inhibited as ionization electrons are swept out of the event region. This process is used to help spatially locate an energy deposition event in a LXe detector. In the case of an applied drift field, the quantities available for collection from these processes are ionization electrons from the cascade (those which do not

recombine), scintillation photons, and infrared photons. A drift field does not effect the excitonic scintillation component (eqn. 6.1).

The energy deposited by an ionizing particle at energy E_0, available for collection in the presence of a drift field, is then

$$E_0 = E_I + E_S + E_H \tag{6.3}$$

where E_I, E_S, and E_H are the energy contributions of ionization, scintillation, and heat. In this work, only ionization and UV scintillation processes are studied. Recent investigations have shown that the infrared photon energy channel may contribute a significant number of detectable photons [56, 57]. The deposited ionization can be collected in the form of electrons and scintillation photons, neglecting heat, so that

$$E_0 = E_I + E_S \propto N_I + N_S \tag{6.4}$$

where N_I and N_S are the numbers of ionization electrons and scintillation photons produced, respectively. It is assumed, in this case, that one scintillation photon is produced per e^--ion pair not collected as ionization. This is the ideal case; no losses such as impurities are assumed. Due to the statistical nature of energy deposition in a dense medium, the values of E_I, E_S, N_I, and N_S will fluctuate, event by event, about the average values $\langle E_I \rangle, \langle E_S \rangle, \langle N_I \rangle$, and $\langle N_S \rangle$. It follows that for multiple ionizing events of energy E_0,

$$\langle E_0 \rangle = \langle E_I \rangle + \langle E_S \rangle \propto \langle N_I \rangle + \langle N_S \rangle \tag{6.5}$$

where $\langle E_I \rangle$, $\langle E_S \rangle$ are the average energy deposited as ionization and scintillation, and $\langle N_I \rangle$, $\langle N_S \rangle$ are the average numbers of ionization electrons and scintillation photons, after recombination has occurred. E_I, E_S, N_I, N_S, and their averages, are functions of E_0, $\mathcal{E}_D$, and the type of radiation. Increasing E_0 will increase $\langle N_I \rangle$ and $\langle N_S \rangle$, whereas increasing $\mathcal{E}_D$ increases $\langle N_I \rangle$ and decreases $\langle N_S \rangle$ by inhibiting recombination. Note that as $\mathcal{E}_D \rightarrow \infty$, excitonic scintillation photons are still produced.

The deposited energy is related to to the average ionization electron and scintillation photon yields by

$$\langle E_I \rangle = W_I \langle N_I \rangle \tag{6.6}$$

$$\langle E_S \rangle = W_S \langle N_S \rangle \tag{6.7}$$

The constants of proportionality, W_I and W_S, are the average energy per ionization electron and scintillation photon produced [58, 59]. Usually, W_S is measured at $\mathcal{E}_D = 0$ where it is maximum, and is different depending on the type of ionizing radiation. In contrast, W_I is measured at high fields in order to minimize electron loss due to recombination.

6.2 Energy collection

In EXO, scintillation photons are collected by surrounding the LXe volume with photodetectors sensitive to 175 nm photons. Ionization electrons are collected by applying a static drift field, $\mathcal{E}_D$ across the detector. $\mathcal{E}_D$ drifts electrons from the energy deposition region to an anode, coupled to a charge amplifier. The time difference between the scintillation photon pulse and the collected ionization electron signal allows for the localization of an energy deposition event in the detector. The event cannot be localized with collection of scintillation photons alone.

6.2.1 Effect of a drift field on ionization and scintillation

When a drift field is applied across the LXe volume, a fraction of the ionization electrons (proportional to the magnitude of $\mathcal{E}_D$) from the initial cascade are drifted outside of the region containing Xe^+ and Xe^*. The amount of recombination and, consequently, scintillation is reduced. This is how the dependence of E_I, E_S, N_I, N_S and their averages on drift field arises. At high fields, recombination scintillation is suppressed (eqn. 6.2). At low or zero field, all of the electrons recombine or thermalize, producing a maximal scintillation photon yield. A functional form for

the dependence of ionization and scintillation yields and fluctuations on $\mathcal{E}_D$ has been investigated, but does not appear to be successful at reproducing observed values [60].

6.2.2 Effect of radiation type and energy on ionization and scintillation

The microscopic energy loss processes of ionizing radiation are described by the Bethe-Bloch model [2]. This model statistically describes energy loss via Coulomb scattering of an incoming particle on electrons in a medium (orbital e^-, in the case of Xe), but does not include scintillation processes such as electron-ion recombination. The Bethe-Bloch model is non-linear in energy, and varies according to the type of incident radiation. While conservation of energy (eqns. 6.5-6.4) must always be satisfied, the individual ionization and scintillation yields will differ according to energy and radiation type.

For example, α-particles, nuclear recoils, and fission fragments produce a very high local ionization density, enhancing recombination and producing a much larger scintillation yield than electrons or γ-rays of the same energy [61, 58]. Also, the individual ionization and scintillation yields for a 2.5 MeV electron versus two 1.25 MeV electrons will differ, though the integral of all collected energy should be the same in either case. This provides a powerful discrimination method (e.g. being able to tell the difference between a 2.5 MeV electron, and two 1.25 MeV electrons) in the search for double beta decay of ^{136}Xe. The details of these physical processes are extensive, and far beyond the scope of this work. A detailed discussion can be found in [2].

6.2.3 Ionization and scintillation time structure

If both ionization and scintillation signals are collected from an energy deposition event in the presence of a drift field, the scintillation signal is prompt, followed by the ionization signal. The scintillation photons are produced (and collected) on a timescale of the processes described in eqns. 6.1 and 6.2, whereas the ionization electrons must drift across the LXe volume for collection. It is assumed that the energy deposition time is much shorter than these processes, which is the case in a

small detector.

The scintillation processes have multiple time constants associated with them [62, 63, 64]. First, the time required for electron-ion recombination (eqn. 6.2), τ_R [65]. Second, the time constants for dimer singlet and triplet state de-excitation (both scintillation processes), denoted τ_D^1 and τ_D^3, respectively. τ_R differs according to the type of radiation, and ionization density. In general, τ_R is on the order of the energy deposition time ($\lesssim$ ns), but can be long in certain circumstances [58]. The experimentally measured dimer de-excitation time constants (found to be independent of both ionization density and drift field) in LXe are [64]

$$\tau_D^1 = 4.3 \pm 0.6 \text{ ns} \tag{6.8}$$

$$\tau_D^3 = 22 \pm 2.0 \text{ ns} \tag{6.9}$$

The scintillation is therefore produced and collected on these timescales.

The ionization collection time constant τ_I is determined by the drift time from the ionization event to the collection point. This drift time is

$$\tau_I = \frac{\Delta x}{v_d} \tag{6.10}$$

where

$$v_d = \mathcal{E}_D \mu(T, n) \tag{6.11}$$

is the electron drift velocity, $\mu(T, n)$ is the electron mobility as a function of temperature T and number density n, and Δx is the physical distance between the ionization event and the detector anode. In the case of electrons as the impinging radiation (as in double beta decay), the energy deposition can be thought of as a point source. As the resulting ionization electrons drift towards the anode, the electrons diffuse, becoming a cloud. In this case, the drift time is smeared with the diffusion time. For small detectors, the diffusion time is large compared to the drift time, so it can be neglected. Some values of μ and v_d for electrons in LXe, at 163 K and a density $n = 14.1 \times 10^{19}$ atoms/cm^3 are listed in table 6.1 [4]. The errors on these numbers are below the resolution of the plotted data in [4].

$\mathcal{E}_D$ [kV/cm]	μ [cm^2/(V · s)]	v_d [10^5 · cm/s]
1.0	241	2.41
2.0	135	2.69
4.0	72	2.87
8.0	38	3.02

Table 6.1: Experimentally measured electron mobility μ and drift velocity v_d at different drift fields [4]. These data are measured in LXe at 163 K, and $n = 14.1 \times 10^{19}$ atoms/cm^3.

For a drift field of 2 kV/cm and a drift distance $\Delta x = 5$ cm, the drift time is $\tau_I = 19$ μs. This time delay between the ionization and scintillation signals for a given event can be used to determine the position of the event with respect to the ionization collection plane.

6.3 Energy correlations and fluctuations

The physics of energy deposition and collection in LXe exhibits three distinct properties: linearity of ionization and scintillation yield with the energy of the incident radiation, a macroscopic ionization-scintillation anti-correlation, and a microscopic ionization-scintillation anti-correlation. The first two properties depend on the macroscopic parameters E_0 and $\mathcal{E}_D$, and affect the quantities $\langle N_I \rangle$ and $\langle N_S \rangle$ (i.e. the yields averaged over many energy deposition events). The third property affects the values of N_I and N_S for each energy deposition. The first two properties are used in the analysis presented in ch. 7 as energy cuts, whereas the third property leads to an enhancement in LXe energy resolution.

6.3.1 Energy linearity

According to eqn. 6.5, the sum of the average ionization and scintillation yields is proportional to the amount of energy deposited by ionizing radiation. For example, the energy deposition from a γ at energy E_0 will show up as a peak in the spectra

of N_I and N_S, with central values $\langle N_I \rangle$ and $\langle N_S \rangle$; increasing E_0 will simultaneously increase both $\langle N_I \rangle$ and $\langle N_S \rangle$. The ionization and scintillation yields, $\langle N_I \rangle$ and $\langle N_S \rangle$, are therefore positively correlated with the energy E_0 of incoming radiation. Note that different types of incident radiation (e.g. α-particles vs. γ-rays) at the same energy produce different amounts of ionization electrons and scintillation photons, due to the microscopic physics of energy deposition. This property is primarily useful as a means of making analysis cuts on energy deposition peaks.

6.3.2 Macroscopic ionization-scintillation anti-correlation

A drift field $\mathcal{E}_D$ applied across a LXe volume controls the sharing of energy (via electron-ion recombination) between ionization and scintillation, as discussed in §6.2.1. Increasing $\mathcal{E}_D$ increases the average ionization electron yield $\langle N_I \rangle$, thereby decreasing the average scintillation yield $\langle N_S \rangle$ by conservation of energy (eqns. 6.3-6.5). The ionization and scintillation yields are therefore anti-correlated as a function of the macroscopic parameter $\mathcal{E}_D$. This property has been observed and measured in LAr and LXe [66], and in this work in §7.3 and [12].

6.3.3 Microscopic ionization-scintillation anti-correlation

The values of N_I and N_S, produced by ionizing radiation at energy E_0, fluctuate about $\langle N_I \rangle$ and $\langle N_S \rangle$, respectively, in a correlated manner to keep E_0 constant. The fluctuations are due to the statistical nature of energy deposition and electron-ion recombination, whereas the correlation is due to conservation of energy (eqns. 6.3-6.5). For a given event, if $N_I > \langle N_I \rangle$ then $N_S < \langle N_S \rangle$ to conserve energy; therefore the ionization and scintillation yields, N_I and N_S, are anti-correlated with each other event-by-event.

This property suggests that an improvement in energy resolution is possible by simultaneously collecting ionization and scintillation signals, in contrast to collecting either one alone. This has been shown in LAr [67], and is shown to be the case experimentally in LXe (see §7.3 and [12]).

6.3.4 Energy fluctuations

Spectra of collected ionization electrons and/or scintillation photons (or the sum of the two) produced from multiple independent energy depositions at an energy E_0 will be peaked at the values of $\langle N_I \rangle$ or $\langle N_S \rangle$. The production of ionization electrons and scintillation photons, due to incident radiation at energy E_0, can be modeled as a Poisson process. Assuming that the yields are large,

$$\langle N_I \rangle , \langle N_S \rangle \gg 1 \tag{6.12}$$

and that all deposited energy is collected, a peak in either energy spectrum can be modeled by Gaussian distribution,

$$G(E) = \frac{A}{\sqrt{2\pi\sigma_E^2}} e^{-\frac{(E-E_0)^2}{2\sigma_E^2}} \tag{6.13}$$

where $\sigma_E = \sqrt{E}$ is the energy distribution width for a purely Poisson process. If conservation of energy is imposed as a constraint in each individual energy deposition event, the production of an ionization electron in the cascade becomes correlated to the previous electron. This correlation, first described by U. Fano [68], alters the distribution width by a factor F (the Fano factor), so that

$$\sigma_E = \sqrt{FE} \tag{6.14}$$

For LXe, $F = 0.04$ (calculated, [7]), whereas the experimental value is $\gg 1$ [12]. This indicates that there are fluctuations that are unaccounted for in this theory.

In any real system, some energy is always lost (e.g. heat, finite fiducial volume, another energy channel, etc.) and the energy quanta production process may not be purely Poissonian. This is the case for N_I and N_S, as each of these quantities is an incomplete measure of the total amount of energy deposited in a LXe volume. Regardless, the energy peaks in these channels can still be modeled using eqn. 6.13, where the constraint on the width (eqn. 6.14) becomes the theoretical lower limit.

The actual width can be written as

$$\sigma_E = \sqrt{F_{eff} E} \tag{6.15}$$

where F_{eff} is an effective Fano factor. This is an important scaling relation that has been observed experimentally in energy resolution studies in LXe [7].

The empirical width of N_I has been measured to be much larger than the Poisson limit [7, 12, 59], leading to a poor ionization energy resolution (see §6.4). The improvement in LXe energy resolution shown in this work is accomplished by collecting both ionization electrons and scintillation photons simultaneously.

6.4 Energy resolution

Energy resolution is a dimensionless metric used to determine how accurately energy deposition can be measured in a detector. The energy resolution is defined as

$$R(E_0) = \frac{\sigma}{E_0} \tag{6.16}$$

where σ is the width of an energy peak created by ionizing radiation at energy E_0 (see eqn. 6.13). Using eqn. 6.5, the energy resolution can be written as

$$R(E_0) = R(\langle N \rangle) = \frac{\sigma_N}{\langle N \rangle} \tag{6.17}$$

where $\langle N \rangle$ refers to ionization electrons, scintillation photons, or the sum of the two. The width scales with the number of ionization electrons or scintillation photons (see eqn. 6.15),

$$\sigma_N \propto \sqrt{\langle N \rangle} \tag{6.18}$$

The energy resolution therefore scales with energy E, or number of quanta N, as

$$R(E) \propto \frac{\sqrt{N}}{N} = \frac{1}{\sqrt{N}} \propto \frac{1}{\sqrt{E}} \tag{6.19}$$

This energy scaling law has two implications. First, energy resolution improves with increasing energy deposition, or number of quanta collected. Therefore, maximizing the number of collected ionization electrons and/or scintillation photons is an important detector requirement. Second, if an empirical energy resolution is measured at energy E_0, the energy resolution at E_0' can then be extrapolated to be

$$R(E_0') = R(E_0)\sqrt{\frac{E_0}{E_0'}} \tag{6.20}$$

In addition, if uncorrelated gaussian noise is present (e.g. electronic noise from a charge amplifier used to integrate the ionization signal) in the measurement of N, the noise subtracted energy resolution R_{NS} at energy E_0 is

$$R_{NS}(E_0) = \frac{\sqrt{\sigma^2 - \sigma_{\text{Noise}}^2}}{E_0} \tag{6.21}$$

where the noise fluctuations, σ_{Noise}, are subtracted off in quadrature from the measured distribution width. In ch. 7, this framework is used to analyze and evaluate the energy resolution performance of a LXe detector.

Chapter 7

Energy resolution studies in liquid Xe

The energy resolution of the EXO detector determines the sensitivity to both the $0\nu\beta\beta$ and $2\nu\beta\beta$ modes. Evidence of $0\nu\beta\beta$ will show up as a peak in the energy spectrum of events measured in the EXO detector. This peak will occur at the Q-value (2457.83 ± 0.37 keV, see [69]) of the decay, and will have a width given primarily by the energy resolution of the detector. Since current lower limits on the $0\nu\beta\beta$ half life are $\sim 10^{25}$ yr., the ability to distinguish this peak from all other backgrounds is crucial. Background elimination is accomplished in the EXO detector in two ways. First, by determining the energy of a candidate event with good energy resolution. Second, by determining the spatial location of the candidate event in the detector. The decay daughter, $^{136}Ba^{+}$, can then be extracted and tagged in real time [11].

In order to simultaneously satisfy both of these requirements, ionization and scintillation signals are collected from an energy deposition event (see ch. 6). The time delay between the ionization and scintillation signals, in addition to the spatial distribution of the drifted ionization electrons on the anode of the detector, allows for the reconstruction of the candidate decay vertex position. This technique degrades the energy resolution, compared to collecting scintillation only in the absence of an applied drift field. This is due to the detailed physics of electron-ion recombination. A method of enhancing LXe energy resolution, in the presence of a drift field, by

collecting both ionization and scintillation signals event-by-event is presented in this chapter.

7.1 Overview

The best ionization energy resolution (i.e. collecting ionization electrons only by applying a drift field across the detector, ignoring scintillation photons) reported for energy deposition by electrons from a ^{207}Bi source in LXe at 4 kV/cm drift field is $\sigma/E = 3.4$ % at 570 keV [7]. The best energy resolution reported, collecting only scintillation photons from a 122 keV ^{57}Co source, is $\sigma/E = (8.8 \pm 0.6)$ %, at zero drift field [70]. Assuming a Poisson scaling of the energy resolution (eqn. 6.19), this becomes (4.1 ± 0.3) % at 570 keV. In this work, the energy resolution is improved to 2.7 % at 4 kV/cm by combining the ionization and scintillation signals at 570 keV. This is an improvement by a factor of 1.3 with respect to the ionization alone [12]. The improvement is more dramatic at lower drift fields, where electron-ion recombination is dominant. At 0.2 kV/cm drift field, the resolution improves from 10.7 % to 4.9 %, or a factor of 2.2 from ionization alone. These numbers are dependent upon such factors as the geometry of the detector, the light collection efficiency, and the Xe purity. Optimizing a detector with respect to these factors will lead to the best energy resolution.

7.2 Experimental setup

The system used to study LXe energy resolution by simultaneously collecting ionization electrons and scintillation photons is described here. The major components of the system are the LXe cell, cryogenic system, gas handling system, high voltage system, and analog/digital data acquisition system.

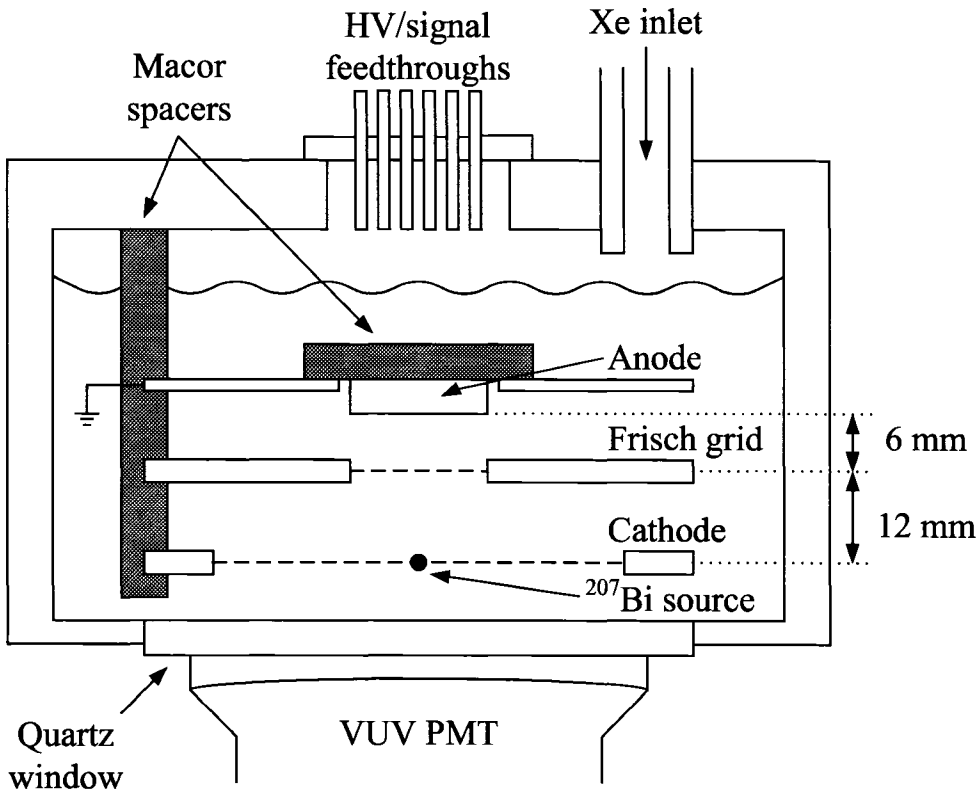

Figure 7.1: Schematic of the LXe cell used for energy resolution studies. Electrons and γs are produced by a ^{207}Bi EC source plated on the cathode. Ionization is read out on the anode, and scintillation by the PMT below the source.

7.2.1 LXe cell

The LXe cell is a 1.5 ℓ UHV grade stainless steel cylindrical chamber, shown schematically in fig. 7.1. The top of the chamber has a 1.5" diameter tube for Xe injection, as well as a SHV feedthrough for application of high voltage to the grids, and for acquiring the charge signal from the anode. A specially selected 8" diameter quartz vacuum window, with 80 % transmission at the LXe scintillation wavelength (175 nm), is mounted on the bottom of the chamber . A vacuum ultraviolet photomultiplier tube (VUV PMT[1]) with a 6" diameter face and a quantum efficiency of 20 % at 175 nm is coupled to the outer face of the the quartz cell to collect scintillation light.

[1]Model EMI 9921Q

The cathode and Frisch grid (referred to as grid) are made of a stretched, nickel electroformed mesh with 90 % optical transparency. All other components are stainless steel or macor. Ionization and scintillation are created by a ^{207}Bi EC source, deposited on the cathode (see §7.2.4). Positive high voltages are applied to the grid and cathode, while the ring surrounding the anode is kept at ground. The anode itself is coupled to a charge amplifier, and is therefore kept at virtual ground. This field configuration causes ionization electrons to drift through the LXe for collection at the anode. The grid shields the anode from the electric field of the ionization cloud as it drifts upwards, until it passes through the grid plane. The ionization is then collected as a single fast pulse, independent of the drift length below the grid. The electric field between the anode and grid is kept at a factor of two higher than the field between the cathode and the grid, in order to maximize the transfer of ionization electrons across the grid [71].

7.2.2 Cryogenic system

The cryogenic system serves two purposes. First, if liquifies the Xe in the LXe cell. Second, it keeps the LXe cold and minimizes the temperature gradient across the cell. The cell is cooled by immersion in a bath of HFE-7100[2] which in turn is cooled by a liquid nitrogen heat exchange loop (see fig. 7.2). HFE-7100 is a commercial heat transfer fluid with two convenient properties. First, it has a wide liquid range (-135°C to 61°C), which allows for convective heat transfer at LXe temperature (-104°C) and therefore good temperature uniformity over then entire chamber body. Second, it has a volume resistivity of 3.3×10^9 Ω-cm. This minimizes leakage currents at the feedthroughs and electronics immersed in the bath, though all electrical connections are potted with low temperature silicone rubber. The chamber and fluid bath are contained in a vacuum insulated dewar[3], as shown in fig. 7.2. The temperature of the system is monitored and regulated by an external PID controller, which monitors RTDs placed on the chamber and controls a liquid nitrogen valve. The chamber is kept at -104 ± 0.2 °C, and the temperature gradient across the chamber is measured

[2]Methoxy-nonafluorobutane $C_4F_9OCH_3$, produced commercially by 3M
[3]Cryofab

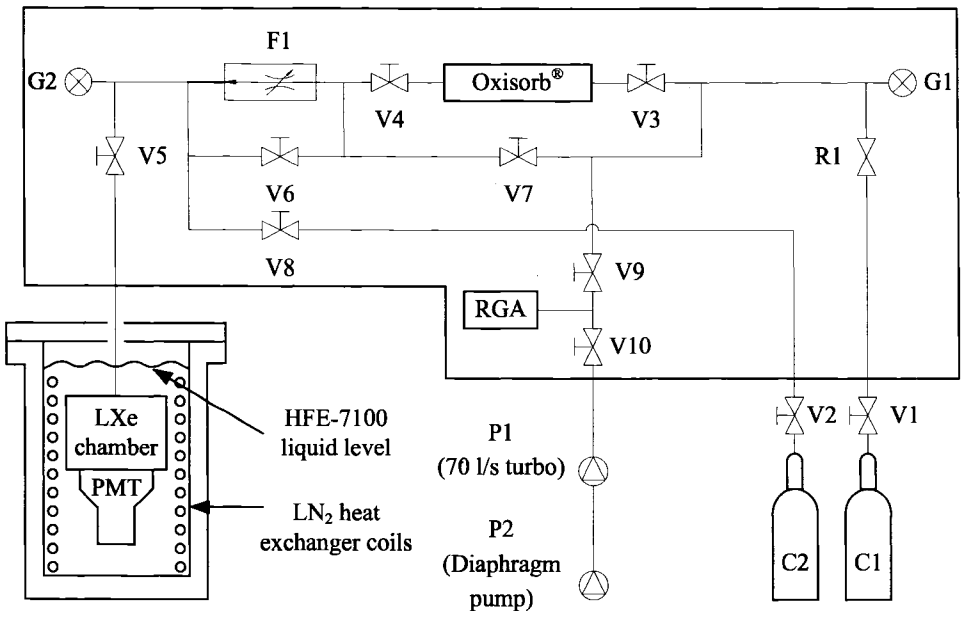

Figure 7.2: Schematic view of full LXe system, including LXe cell and gas handling system. The boxed region is enclosed in an oven for bakeout. The chamber is also bakeable, when the PMT and dewar are removed.

to be < 0.2 °C. The pressure of Xe above the liquid is kept at 990 ± 30 torr.

7.2.3 Gas handling system and liquification procedure

The xenon handling system is shown in fig. 7.2. Hardware components are all-metal UHV compliant, and are cleaned and handled according to UHV standards[4]. The boxed area in fig. 7.2 containing most of the vacuum hardware is enclosed in an oven for bakeout after the system has been opened to air. The bakeout procedure consists of a 3-4 day pump down with a 70 ℓ/s turbo pump[5] backed by a diaphragm pump, while the system is baked at 150 °C. After bakeout, the system is considered clean if the partial pressures of electronegative impurities (O_2, CO_2, etc) as measured by the residual gas analyzer[6] (RGA in fig. 7.2) are $< 10^{-9}$ torr.

During bakeout, or when the system is not in use, the Xe is stored in cylinder C1.

[4]Powderless gloves worn at all times, parts sonicated in alcohol, etc.
[5]Varian V-70LP
[6]Stanford Research Systems model SRS RGA300

Liquifaction begins by cooling the LXe cell down to -104 °C. All valves (including regulator R1 and flowmeter F1) are initially closed. V1 is opened, followed by R1 while monitoring the pressure on gauge G1. Once the Xe pressure is $\sim$ 760 torr, V3 and V4 are opened. The Xe passes through a filter[7] cartridge for purification. F1 is set to a flow rate of $\sim$ 100 torr-ℓ/s, V5 opened, and the chamber pressure monitored on gauge G2. The Xe gas is cryopumped and condensed into the chamber over a period of $\sim$ 2 hrs. Once this process is complete, F1 is closed, and the chamber pressure is monitored continuously on G2.

In order to recover the Xe at the end of a run, cylinder C1 is cooled in a LN_2 bath. All valves are closed, except for V5, V6, V7, V1, and R1. The Xe is slowly cryopumped from the LXe cell to cylinder C1, where it is frozen. Once this process is complete, V1 is closed, and any residual gaseous Xe is pumped out of the system via pumps P1 and P2. Cylinder C2 is used as an emergency "dump" bottle, in case of any failure of C1.

7.2.4 ^{207}Bi β^-/γ source

Ionization in the LXe cell is created by a ^{207}Bi EC source. The major decay channels [5] and their intensities are listed in table 7.1. In addition to these lines, there are K- and L-shell internal conversion electrons at 481, 554, 976, and 1048 keV [7]. ^{207}Bi is a standard calibration used in liquid noble gas ionization and scintillation systems, due to the large number of monoenergetic lines. It is also useful for comparing data from different sets of published results. The source is prepared as a monatomic layer, electroplated on a 3 μm diameter carbon fiber. The fiber is woven into the cathode mesh, as shown in fig. 7.3. The thin source minimizes the effects of self-shadowing of the scintillation light, and is essential to obtaining high scintillation resolution. This effect is observed in simulation, as well as experimentally by altering the source thickness.

[7]Messer Griesheim Oxisorb®

Energy (δE) [keV]	Intensity (δI) [%]
328.12 (10)	0.00067 (8)
567.702 (2)	97.74 (3)
897.80 (5)	0.121 (8)
1063.662 (4)	74.5 (2)
1442.20 (9)	0.130 (3)
1770.237 (10)	6.87 (4)

Table 7.1: Gammas from ^{207}Bi source used for energy resolution studies in LXe [5].

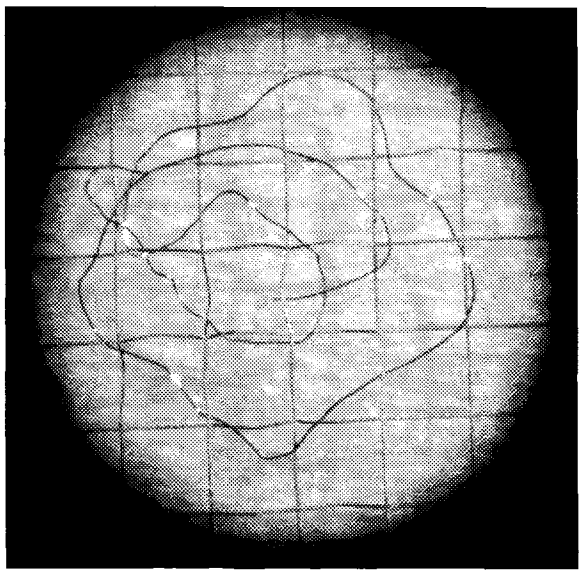

Figure 7.3: Photo of ^{207}Bi-plated carbon fiber woven into cathode grid.

7.2.5 Ionization readout

Ionization, created by the ^{207}Bi source, is collected in a cylindrical fiducial volume with a 10 mm radius and 18 mm height. This region is defined by the cathode grid and the anode plane height-wise, and radially by the grid diameter (see fig. 7.1). Drifted electrons are collected at the anode, coupled to a low-noise charge sensitive preamplifier[8] with a cooled FET[9] (see fig. 7.4). This FET is chosen to minimize electronic noise, due to the finite capacitance between the anode and ground. The FET stage is in a grounded box placed outside of the LXe chamber, but inside of the dewar so as to be kept cold. The integrated charge signal is sent through a double-output Gaussian shaper[10] with a 50 μs shaping time, and one output is recorded to disk using a waveform digitizer. The integrated signal is fit to a model assuming the ionization is a Gaussian-distributed cloud.

$$f(t) = A\left[1 + \mathrm{erf}\left(\frac{t - t_0}{\sigma_t}\right)\right] e^{-t/\tau} + \alpha \tag{7.1}$$

where $\Delta t = t - t_0$ is the signal offset, and the term $\alpha = De^{-t/\tau} + 100 + 0.019t$ accounts for pileup, digitizer offset, and a small integral nonlinearity, respectively. The amplitude A, time offset t_0, charge signal width σ_t, pileup offset D, and shaper fall-time constant τ are simultaneously fit, event by event. The fit fall time is ~ 50 μs for all the data, as expected. The full ionization readout chain is calibrated in units of electron charge by injecting a sawtooth signal into the input FET through a 2 pF calibrated capacitor. The noise of the ionization preamplifier-shaper chain, including all gains, is measured to be Gaussian with a width $\sigma_{\mathrm{Noise}} = 381$ e$^-$. The conversion factor between collected ionization electrons and digitizer channels is 196.95 ± 0.03 e$^-$ per digitizer channel.

[8] Amptek A250
[9] Sony Semiconductor 2SK152
[10] ORTEC 521

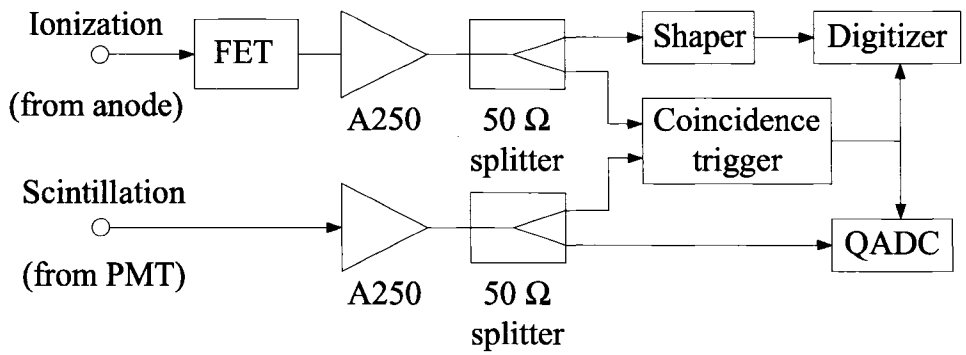

Figure 7.4: Schematic of LXe ionization and scintillation trigger and readout. Ionization and scintillation signals are sent into a coincidence trigger, which causes digitization of the ionization and scintillation signals.

7.2.6 Scintillation readout

Scintillation light produced by the LXe is read out by a PMT operated in photon-counting mode. The PMT high voltage is 1.48 kV, chosen such that the response is linear at all light levels in this study. The measured gain (at LXe temperature) is 6.6×10^6. The scintillation signal from the PMT is sent to a charge sensitive preamplifier[11], followed by a 50 Ω splitter (see fig. 7.4). The first output is sent to a charge integrating ADC[12]. The second output is used for the coincidence trigger, as described in §7.2.7. The conversion between ADC channels and single photoelectrons is calibrated using a flashing LED inside the dewar, and is 3.91 ADC channels per photoelectron. The electronic noise of the preamplifier chain is calibrated in the same fashion as the ionization channel, and is found to be negligible.

The observed number of photoelectrons, N_{pe}, is related to the actual emitted number of scintillation photons, N_S, by

$$N_S = \alpha N_{pe} \tag{7.2}$$

where,

$$\alpha = \frac{A}{\epsilon_{\mathrm{QE}}\ \epsilon_{\mathrm{SA}}\ \epsilon_{\mathrm{Quartz}}\ \epsilon_{\mathrm{Grid}}} = 188.5 \pm 19.3 \tag{7.3}$$

[11]Amptek A250
[12]LeCroy 2249A QADC

where $\epsilon_{QE} = 0.20$ is the quantum efficiency of the PMT at 175 nm, $\epsilon_{SA} = 0.1192 \pm 0.012$ is the solid angle (divided by 4π) seen by the PMT, $\epsilon_{Quartz} = 0.70$ is the transparency of the quartz at 175 nm, $\epsilon_{Grid} = 0.90$ is the optical transparency (fill factor) of the cathode grid, and $A = 2\sqrt{2}$ is an attenuation factor arising from a 50 Ω splitter between the preamplifier and charge ADC. The uncertainty in α comes primarily from the geometrical variation in solid angle (given as the error on ϵ_{SA}) along the main axis of the detector, determined from simulation.

7.2.7 Coincidence trigger

Ionization and scintillation signals are recorded when they occur in delayed coincidence. Given the size of the fiducial volume (see fig. 7.1), the ionization signal from an ionization event reaches the anode a few microseconds after the scintillation signal reaches the PMT. This is due to the drift time of the ionization cloud from the production point to the anode (τ_I in §6.2.3), and must be accounted for in the trigger system.

7.3 Results

The ionization and scintillation correlations described in ch. 5 are observed in this experiment. This analysis uses all correlations to examine the behavior of the energy resolution in LXe at different drift fields, and demonstrate an improvement in energy resolution over previous results [12].

The energy resolution (see §6.4) is determined in two separate ways from the collection of ionization electrons and scintillation photons produced at 570 keV (by the ^{207}Bi source). These quantities are simultaneously collected at drift fields, $\mathcal{E}_D$, of 0.1, 0.2, 0.5, 1.0, 2.0, and 4.0 kV/cm. In the first method (§7.3.1), separate one-dimensional ionization and scintillation energy resolutions at 570 keV are calculated. This one-dimensional analysis is performed as follows. A fiducial cut (in the 2D ionization-scintillation parameter space) is made using the energy correlation property, described in §6.3.1, to isolate the 570 keV energy peak. The one-dimensional

ionization and scintillation resolutions are each determined from this subset of events by projecting the data onto the ionization and scintillation axes, and fitting the peaks to Gaussian distribution functions. In the second method (§7.3.2), a combined two-dimensional energy resolution is calculated from the fit to the two-dimensional distribution of events found in §7.3.1. In §7.3.3, the results of these methods are compared to published results [7]. All of the analysis is presented in units of collected ionization electrons, and collected scintillation photoelectrons. The conversion from photoelectrons to photons is given by eqn. 7.2.

7.3.1 1D energy resolution analysis

A set of one-dimensional ionization and scintillation spectra from the ^{207}Bi source, at $\mathcal{E}_D = 1.0$ kV/cm are shown in fig. 7.5. The two peaks and their associated Compton shoulders in the top spectrum are from ionization electrons collected from the 570 keV and 1064 keV γ-lines. The two peaks in the bottom spectrum are from the same lines, but collected from scintillation photons. In previous works [7, 72], the detector energy resolution is determined by fitting the two ionization peaks to gaussians plus a background function (either a first-order polynomial, or an exponential). At higher $\mathcal{E}_D$, the 976 keV electron peak becomes discernible from the 1064 keV peak. In this case, these peaks are fit to two gaussians. The choice of fitting range varies from paper to paper, though the energy resolution results are consistent with each other (see fig. 7.16). In the analyses presented here, only the 570 keV peak is considered, due to the widening of the 1064 keV peak by the lower energy 976 keV and 1048 keV lines.

In fig. 7.6, the ionization yield is plotted against the scintillation yield, event by event at 1.0 kV/cm. The two islands correspond to the 570 keV and 1064 keV γ-lines. The linearity of ionization electron and scintillation photon yields (see §6.3.1) is evident in the discrete islands visible along the diagonal axis passing through the origin. The microscopic anti-correlation (§6.3.3) is evident in the negative diagonal tilt of each peak. For a given energy, events with a higher ionization yield tend to have lower scintillation yield, and vice versa.

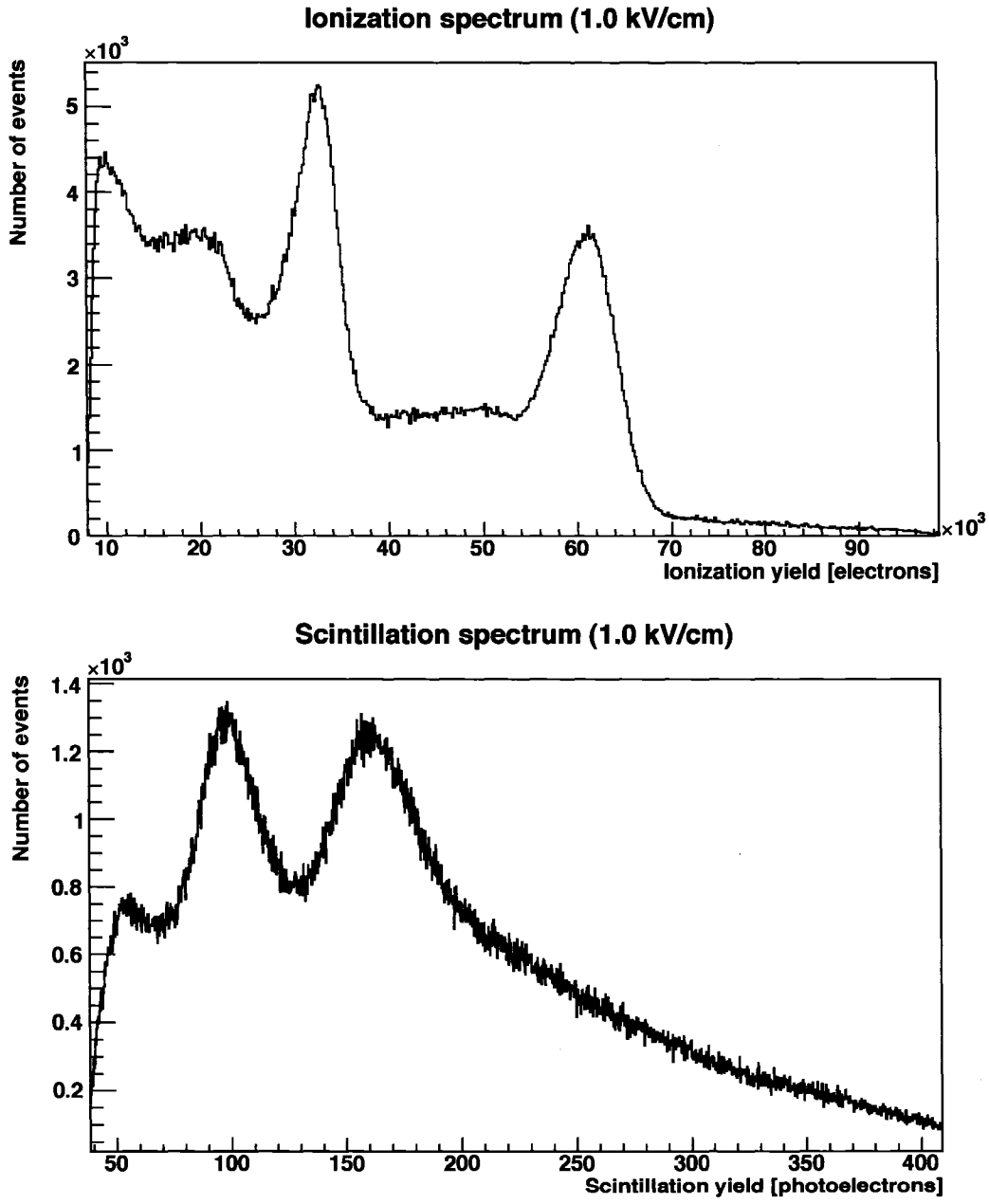

Figure 7.5: Ionization and scintillation spectra at $\mathcal{E}_D = 1.0$ kV/cm. The two peaks are from the ^{207}Bi 570 keV and 1064 keV γ-lines.

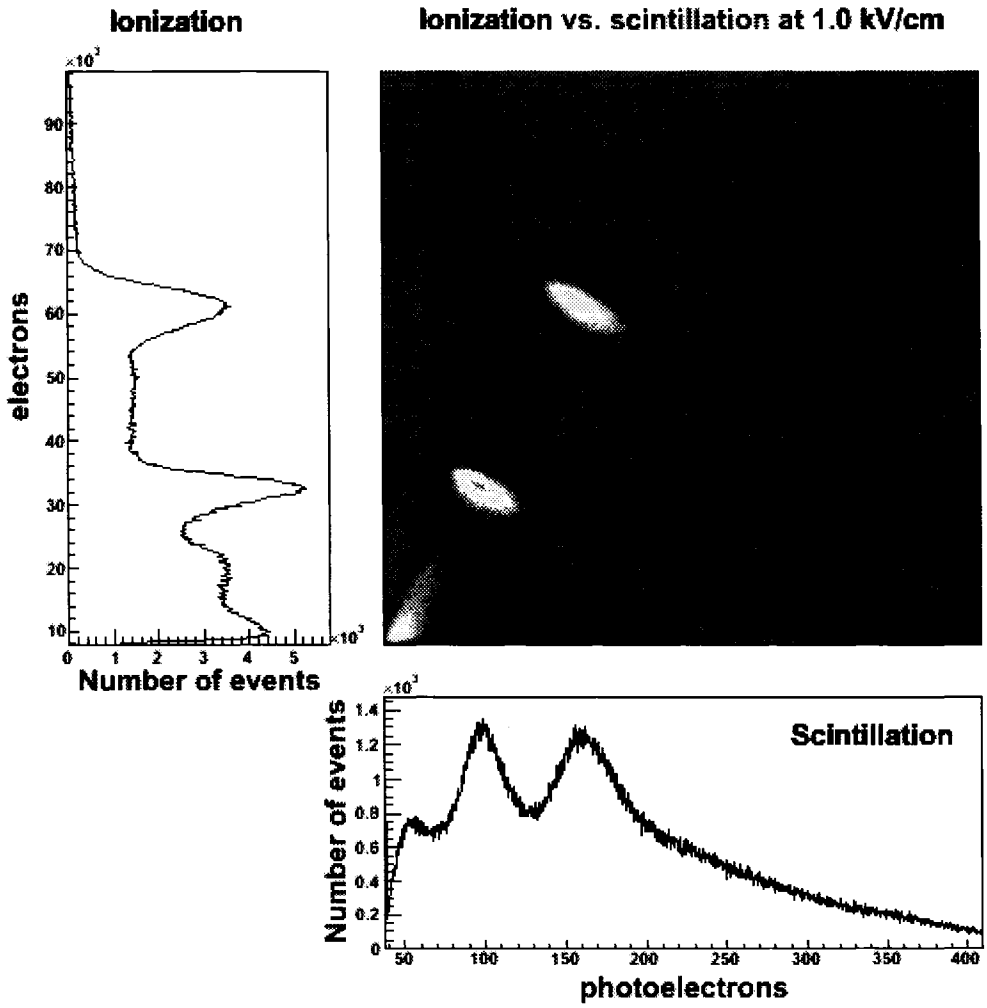

Figure 7.6: Ionization (vertical) plotted against scintillation (horizontal) at $\mathcal{E}_D$ = 1.0 kV/cm. The two islands correspond to the 570 keV and 1064 keV γ-lines.

In order to calculate ionization and scintillation energy resolutions at 570 keV, events are selected from the spectrum in a three step process. In the first step, the peak is isolated with independent cuts along the ionization and scintillation axes, as shown at 1.0 kV/cm in the top row of fig. 7.7. This subset of events is then fit to a two-dimensional gaussian

$$G_{2D}\left(N_e, N_{pe}\right) = \frac{A}{2\pi\sigma_e\sigma_{pe}\sqrt{1-\rho^2}} e^{-\frac{1}{2(1-\rho^2)}\left(\frac{\Delta N_e^2}{\sigma_e^2}+\frac{\Delta N_{pe}^2}{\sigma_{pe}^2}-\frac{2\rho\Delta N_e\Delta N_{ep}}{\sigma_e\sigma_{pe}}\right)} \tag{7.4}$$

where N_e is the number of ionization electrons collected, N_{pe} is the number scintillation photoelectrons collected, σ_e is the width of the ionization electron distribution, σ_{pe} is the width of the scintillation photoelectron distribution, and ρ is the correlation coefficient that that describes the strength of the correlation between the two channels[13]. Further, $\Delta N_e = N_e - \langle N_e \rangle$, and $\Delta N_{pe} = N_{pe} - \langle N_{pe} \rangle$, where $\langle N_e \rangle$ and $\langle N_{pe} \rangle$ are the average numbers of electrons and photoelectrons in the peak. A is an overall scaling to account for the actual peak height, such that

$$\frac{1}{A}\iint G_{2D}\left(N_e, N_{pe}\right) dN_e dN_{pe} = 1 \tag{7.5}$$

This model describes both the widths of each channel (the first two terms in the exponential), as well as the anti-correlated energy sharing between the two channels (the third term in the exponential). The contours of this surface are ellipses, given by

$$\frac{\Delta N_e^2}{\sigma_e^2} + \frac{\Delta N_{pe}^2}{\sigma_{pe}^2} - \frac{2\rho\Delta N_e\Delta N_{ep}}{\sigma_e\sigma_{pe}} = \alpha \tag{7.6}$$

In the second step, events lying inside of the ellipse with α = -ln(0.5) are selected. This choice of α corresponds to the ellipse at the FWHM of the two-dimensional gaussian. This subset of events are refit to a new gaussian, giving a new FWHM ellipse. This selection and refit are repeated again, giving a third FWHM ellipse. The second and third rows of fig. 7.7 show the final selection of events in the 570 keV peak, and the fit value of $G_{2D}\left(N_e, N_{pe}\right)$, respectively.

[13]"Channel" is used to describe either the collected ionization or scintillation signals.

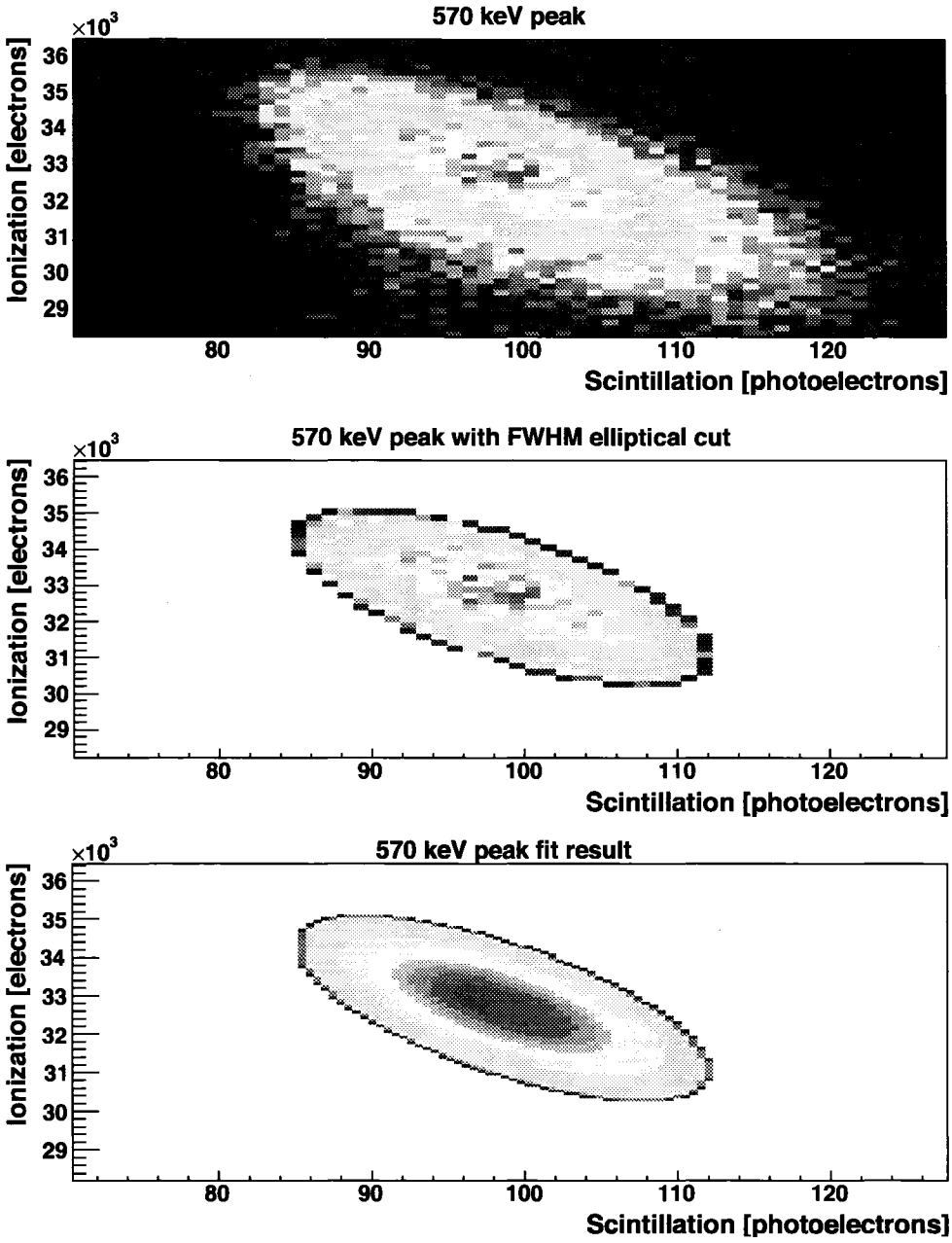

Figure 7.7: The 570 keV γ-line at 1 kV/cm. Top row: before any cuts. Middle row: after two iterations of fitting and cutting (see text for details). Bottom row: two-dimensional fit to data with elliptical cut.

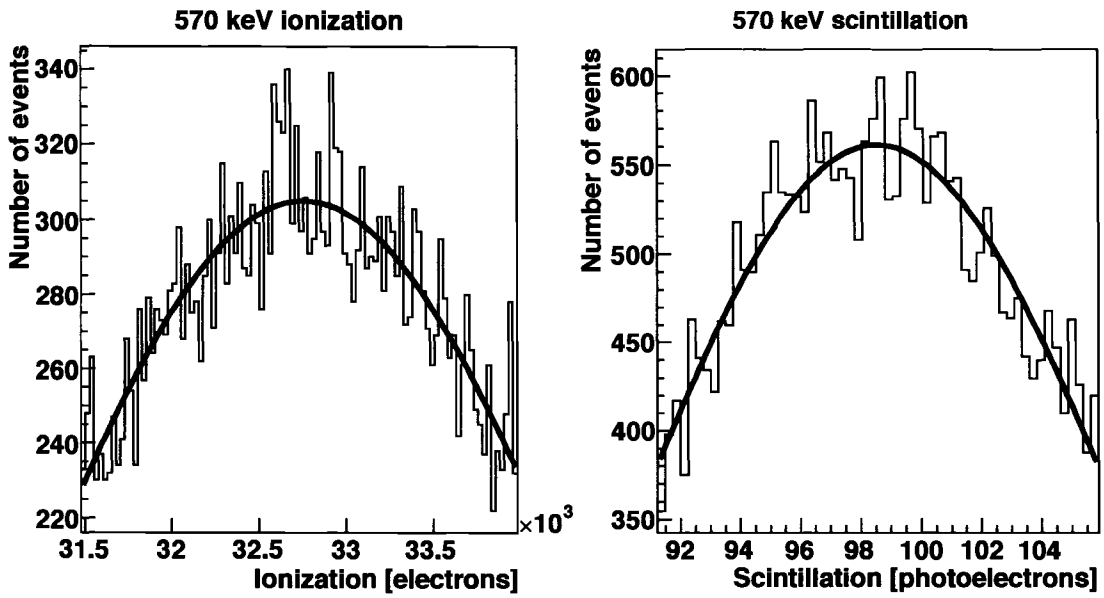

Figure 7.8: One-dimensional projections of the 570 keV γ-line at $\mathcal{E}_D = 1.0$ kV/cm after multiple two-dimensional elliptical cuts. Gaussian fits to the data are overlaid, used to compute the one-dimensional ionization and scintillation energy resolutions.

In the third step, events in this final ellipse are used to determine one-dimensional ionization and scintillation energy resolutions. The data are projected onto the ionization and scintillation axes, as shown for 1.0 kV/cm in fig. 7.8. Each peak is fit to a one-dimensional gaussian

$$G_{1D}(N) = \frac{A}{\sqrt{2\pi\sigma_N^2}} \exp\left(-\frac{(N - \langle N\rangle)^2}{2\sigma_N^2}\right) \tag{7.7}$$

where N is the number of ionization electrons or scintillation photoelectrons (N_e or N_{pe}), $\langle N\rangle$ is the average number of ionization electrons or scintillation photoelectrons ($\langle N_e\rangle$ or $\langle N_{pe}\rangle$), σ_N is the width of the distribution (σ_e or σ_{pe}), and A is an overall scaling factor. The χ^2/dof of these fits at 1.0 kV/cm are 73.85/97 and 70.39/55 for the ionization and scintillation channels, respectively. The ionization and scintillation energy resolutions, R_I and R_S (see eqn. 6.17), are calculated using the fit values of $\langle N\rangle$ and σ_N from eqn. 7.7. The electronic noise (see §7.2.5) on the ionization channel

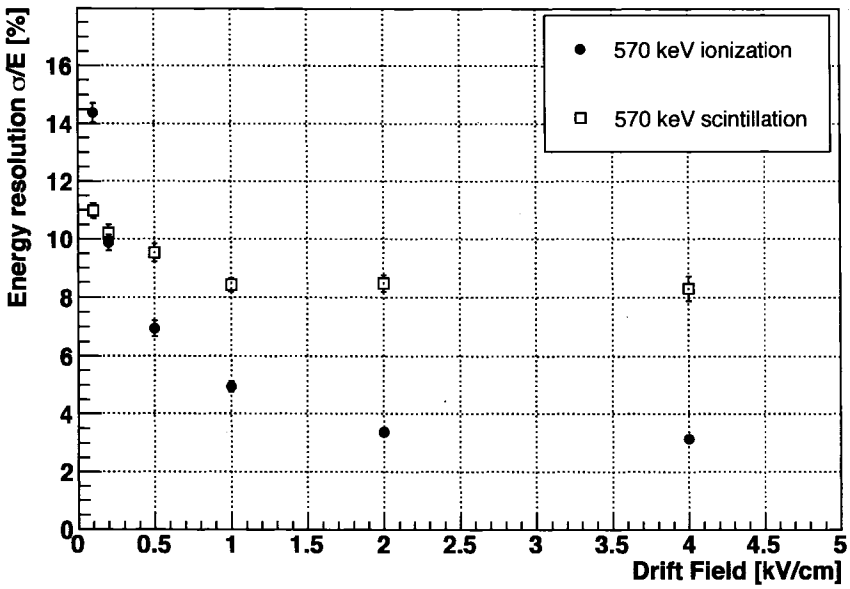

Figure 7.9: Ionization and scintillation energy resolutions vs. $\mathcal{E}_D$ for the 570 keV γ-line.

is subtracted off in quadrature from the measured width, σ_e, in calculating the energy resolution. The noise subtracted width is

$$\sigma'_e = \sqrt{\sigma_e^2 - \sigma_{\text{Noise}}^2} \tag{7.8}$$

The electronic noise on the scintillation channel is negligible. This analysis is repeated at all drift fields, $\mathcal{E}_D$, and plotted as a function of $\mathcal{E}_D$ in fig. 7.9. These data are also tabulated in table 7.2. In general, all quantities presented from here on are noise subtracted in this manner.

As $\mathcal{E}_D$ increases, electron-ion recombination is suppressed (see chapter 6), and more ionization electrons are available for collection. In this analysis, a high collection efficiency of the available ionization electrons (after scintillation processes have occurred) is assumed, as there are no solid angle issues as with the collection of scintillation photons. Therefore, the fit values of $\langle N_e \rangle$ in eqn. 7.7 and σ'_e in eqn. 7.8

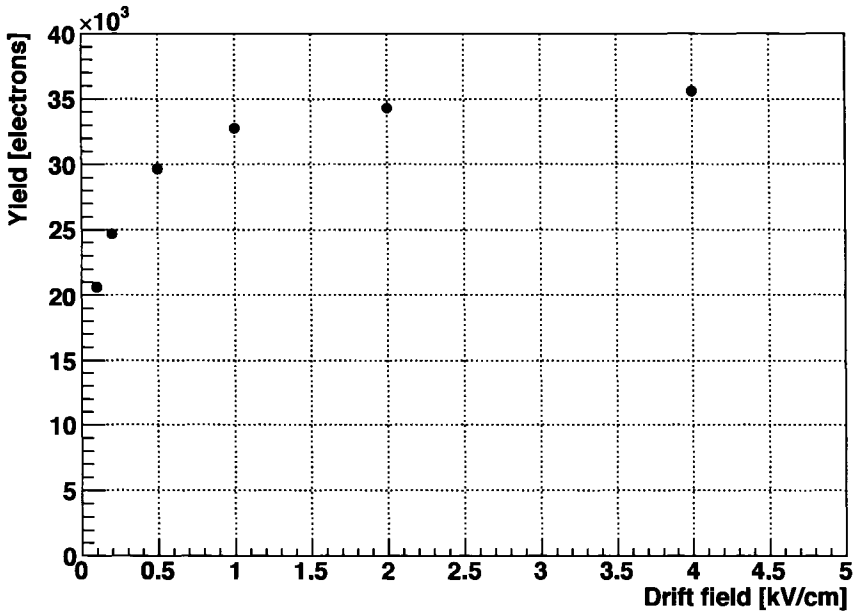

Figure 7.10: Ionization electron yield (from eqn. 6.13) vs. $\mathcal{E}_D$ for the 570 keV peak. The statistical errors are smaller than the markers.

represent the actual yields and fluctuations of ionization electrons available for collection. As more electrons are collected, the resolution improves, as expected (see eqn. 6.19).

In the case of scintillation, on the other hand, the number of collected photoelectrons corresponds to a small fraction of the total number of photons produced (see eqn. 7.2). The relatively poor scintillation resolution in fig. 7.9 is likely due to the very low solid angle coverage (and quantum efficiency, etc.) of this detector, since this decreases the number of scintillation photons collected (see eqn. 6.19).

The fit ionization electron and scintillation photoelectron yields, $\langle N_I \rangle$ and $\langle N_S \rangle$ from eqn. 7.7, are plotted as a function of $\mathcal{E}_D$ in figs. 7.10 and 7.11. As $\mathcal{E}_D$ increases the ionization electron yield increases whereas the scintillation photoelectron yield decreases, as expected (see §6.3.1).

In figs. 7.12 and 7.13, the factor $\sigma^2/\langle N \rangle$ is plotted versus $\mathcal{E}_D$, for the ionization and scintillation channels, respectively. This factor is a measure of how well the electron and photoelectron distributions match a Poisson distribution ($\sigma^2/\langle N \rangle =$

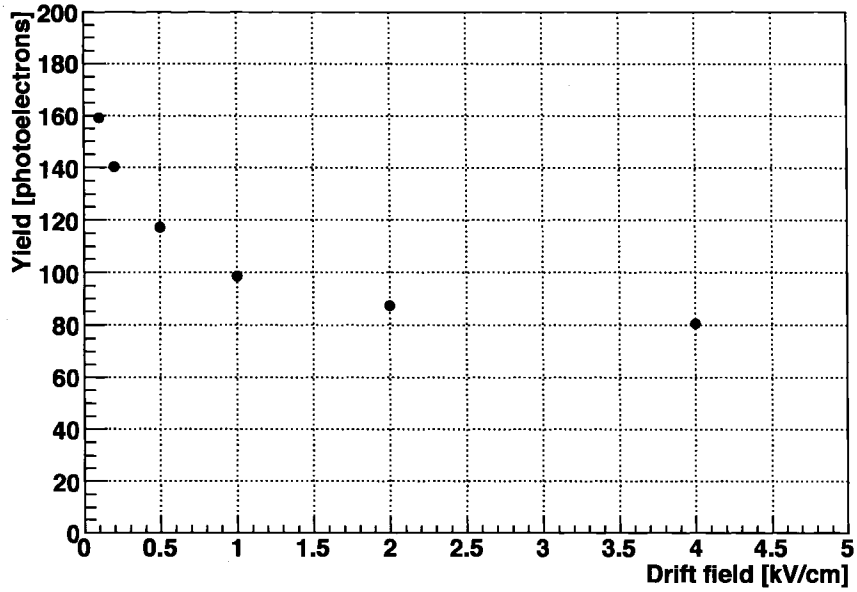

Figure 7.11: Scintillation photoelectron yield (from eqn. 6.13) vs. $\mathcal{E}_D$ for the 570 keV peak.

1 for Poisson fluctuations). In the case of ionization, the fluctuations are highly non-Poisson at all drift fields. At high $\mathcal{E}_D$, a large fraction of the deposited energy is collected as ionization electrons, with the remaining going into the scintillation processes and heat. In this case, the process(es) governing electron production in LXe are primarily responsible for the fluctuations in the yield. At low $\mathcal{E}_D$, the statistics of electron-ion recombination dominate. Evidently, recombination statistics are a highly non-Poisson process. In the case of scintillation, this Poisson factor is close to one for all $\mathcal{E}_D$. Scintillation photoelectron production (and hence photon production) is nearly a Poisson process. The deviation of this factor from one at low $\mathcal{E}_D$ may be due to the fluctuations of electron-ion recombination, which are large in this region. Additionally, it should be noted that the actual number of collected scintillation photoelectrons is small compared with the number of collected ionization electrons at all drift fields.

The fit value of the correlation coefficient, ρ, in eqn. 7.4 for the 570 keV γ-line is plotted versus $\mathcal{E}_D$ in fig. 7.14. ρ measures the strength of the correlation between

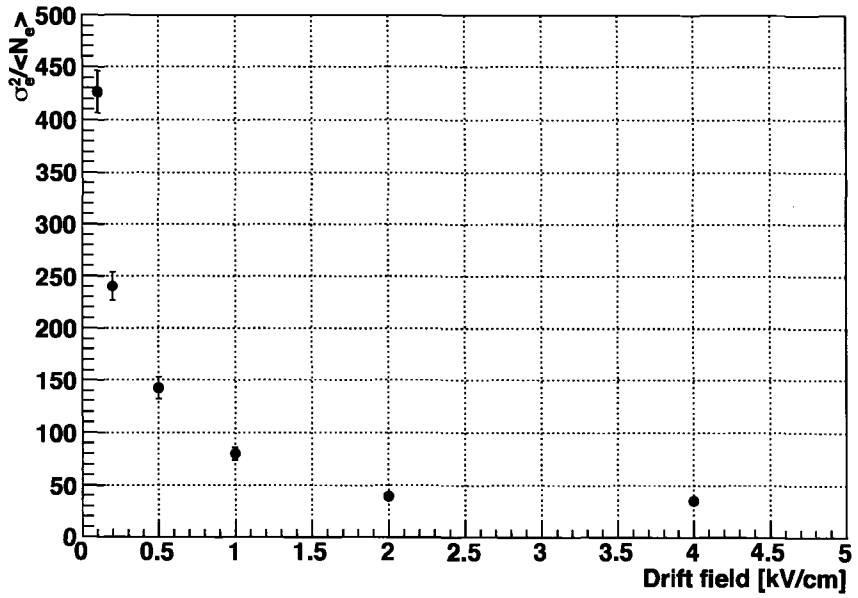

Figure 7.12: $\sigma_e'^2 / \langle N_e \rangle$ vs. $\mathcal{E}_D$ for the 570 keV γ-line. The distribution of ionization electrons is non-Poisson, evident by the deviation of this parameter from 1.

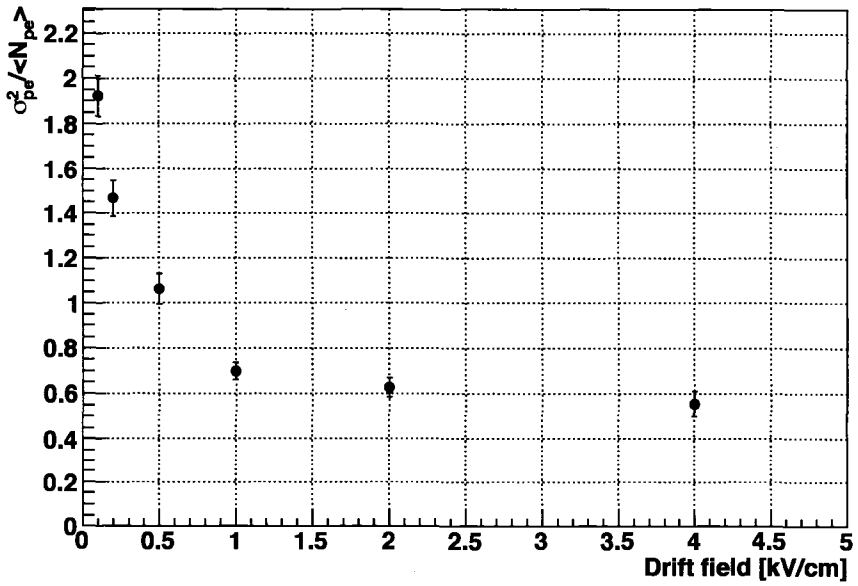

Figure 7.13: $\sigma_{pe}^2 / \langle N_{pe} \rangle$ vs. $\mathcal{E}_D$ for the 570 keV γ-line.

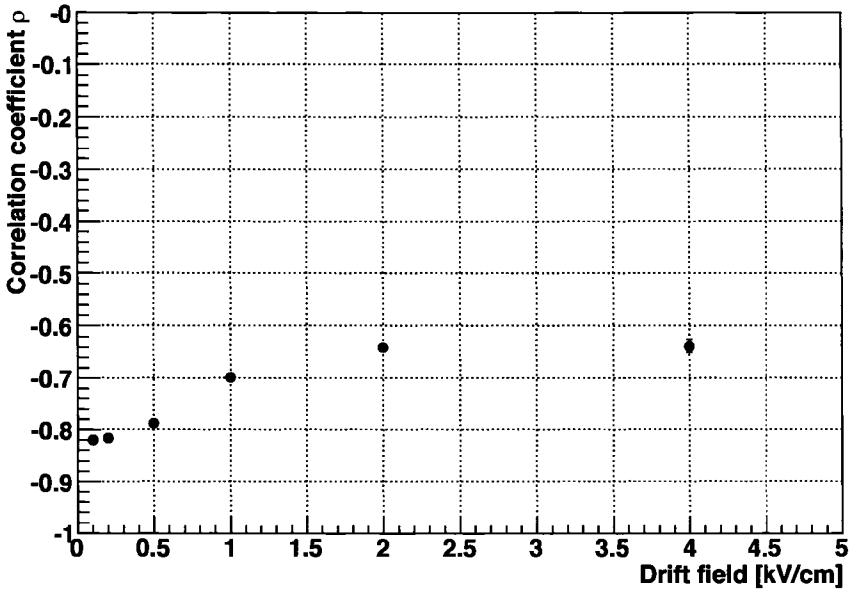

Figure 7.14: Correlation coefficient (dimensionless) ρ versus $\mathcal{E}_D$ for the 570 keV γ-line. The correlation coefficient is negative, which means that the ionization and scintillation channels are anticorrelated.

ionization and scintillation, which has to do with the microscopic physics involved in the energy sharing between the two channels. Note that the highly non-Poissonian behavior of the ionization yield may affect the value of ρ as well. The behavior of ρ with respect $\mathcal{E}_D$ is not well understood.

7.3.2 2D energy resolution analysis

The ionization and scintillation energy resolutions calculated in §7.3.1 are derived from the projections of the 570 keV γ-line onto the ionization and scintillation axes. This does not take advantage of the microscopic anticorrelation between the two signals, as described in §6.3.3. Instead, a single energy resolution using both ionization and scintillation simultaneously can be calculated directly from the fit values of eqn. 7.4. This is done by taking the width of the two-dimensional Gaussian along its minor axis.

The distribution widths along the major and minor axes of a rotated two-dimensional

Gaussian given by eqn. 7.4 are

$$\sigma_v = \sqrt{\frac{\sigma_e'^2 \cos^2\theta - \sigma_{pe}^2 \sin^2\theta}{\cos^2\theta - \sin^2\theta}} \tag{7.9}$$

$$\sigma_u = \sqrt{\frac{\sigma_{pe}^2 \cos^2\theta - \sigma_e'^2 \sin^2\theta}{\cos^2\theta - \sin^2\theta}} \tag{7.10}$$

where

$$\theta = \frac{1}{2}\arctan\left(\frac{2\rho\sigma_{pe}\sigma_e'}{\sigma_{pe}^2 - \sigma_e'^2}\right) \tag{7.11}$$

is the rotation angle of the elliptical contours of the Gaussian [2]. In this analysis, σ_e' and σ_{pe} have different units (electrons and photoelectrons, respectively), so unit-wise σ_u and σ_v are not useful quantities. On the other hand, the rotated energy resolution is unit-less,

$$R_v = \sqrt{\frac{R_I^2 \cos^2\theta' - R_S^2 \sin^2\theta'}{\cos^2\theta' - \sin^2\theta'}} \tag{7.12}$$

$$R_u = \sqrt{\frac{R_S^2 \cos^2\theta' - R_I^2 \sin^2\theta'}{\cos^2\theta' - \sin^2\theta'}} \tag{7.13}$$

where

$$\theta' = \frac{1}{2}\arctan\left(\frac{2\rho R_S R_I}{R_S^2 - R_I^2}\right) \tag{7.14}$$

and R_I and R_S are the noise subtracted one-dimensional ionization and scintillation energy resolutions. R_u and R_v are calculated from the fit results in §7.3.1, and plotted versus $\mathcal{E}_D$ in fig. 7.15. R_u is not useful as an energy resolution, since this corresponds to the width of the peaks along the major axis of the 1σ ellipse. R_v is the resolution computed along the minor axis of the 1σ ellipse, and constitutes an improvement over one-dimensional ionization and scintillation resolutions. These results are tabulated in table 7.2.

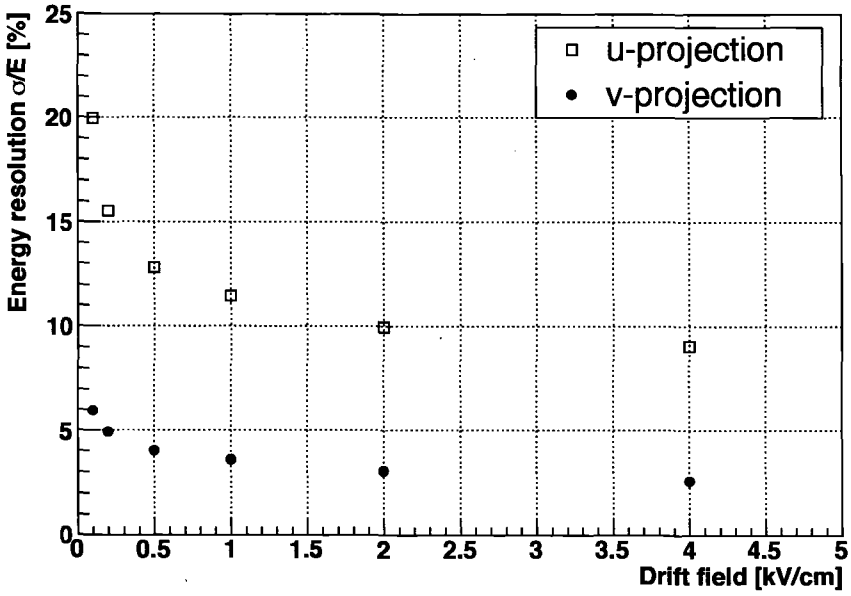

Figure 7.15: Two-dimensional resolutions R_u and R_v, derived from the fit values of eqn. 7.4. R_u and R_v are the energy resolutions along the major and minor axes of the 2D Gaussian, respectively.

E_D [kV/cm]	R_v [%]	R_I [%]	R_S [%]
0.1	5.97 ± 0.07	14.4 ± 0.3	11.0 ± 0.3
0.2	4.92 ± 0.08	9.9 ± 0.3	10.2 ± 0.3
0.5	4.03 ± 0.07	6.9 ± 0.3	9.5 ± 0.3
1.0	3.61 ± 0.06	4.9 ± 0.2	8.4 ± 0.2
2.0	3.07 ± 0.06	3.4 ± 0.1	8.5 ± 0.3
4.0	2.61 ± 0.06	3.1 ± 0.2	8.3 ± 0.4

Table 7.2: Noise subtracted one (R_I and R_S) and two (R_v) dimensional energy resolution results for the 570 keV γ-line, including statistical errors, at different drift fields.

7.3.3 Energy resolution comparison

In §7.3.1 the one-dimensional ionization and scintillation energy resolutions are computed by isolating the 570 keV γ-line in two dimensions, projecting the peak onto the ionization and scintillation axes, and fitting the distributions to Gaussians. This two-dimensional event isolation constitutes an energy cut on 570 keV events. The method used by previous authors (fitting the ionization peaks to Gaussians plus a polynomial background) is not explicitly carried out in this work, though this analysis has been carried out on this data and published in [12]. The results of this one-dimensional plus background ionization analysis are consistent with previous authors' published values [7].

In §7.3.2, a two-dimensional energy resolution is computed from the results of fitting eqn. 7.4 to the 570 keV γ-line in §7.3.1. These results are published in [12]. In the writing of this work, it was found that the results presented therein are erroneous, in that the energy resolutions quoted in [12] are not noise subtracted. This was an oversight by the authors. The energy resolution presented here is $\sim$ 10 % better than the values published in [12]. All data in this work is noise subtracted, and should be considered a correction to the results in [12].

The one- and two-dimensional energy resolution results are plotted in fig. 7.16, along with results from other authors for comparison [7]. The results from other authors use ionization only, computed by fitting peaks to Gaussians plus background functions (see §7.3.1). The data shown here are all scaled to 570 keV assuming an energy scaling given by eqn. 6.20, and when necessary, converted from a FWHM resolution to the σ/E standard used in this work. The two-dimensional resolution shows a significant improvement over all other methods, especially at lower drift field where a larger fraction of the deposited energy goes into scintillation photons. This is the first use of simultaneous ionization and scintillation signals to improve energy resolution in LXe, published in [12]. This result has since been verified for γ-rays and nuclear recoils by other authors [73].

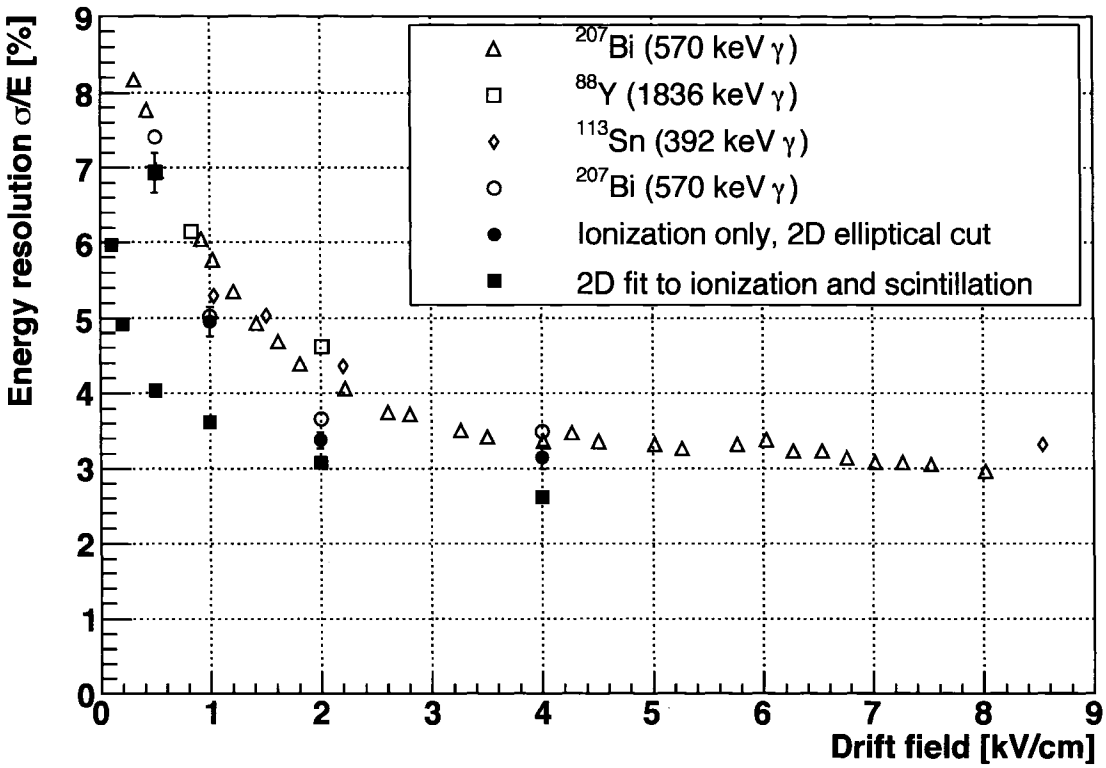

Figure 7.16: Comparison of energy resolutions from other authors [7], as well as those computed in this work. The two-dimensional energy resolutions computed in §7.3.2 show significant improvement over all other methods. All resolutions are noise subtracted, and scaled to 570 keV.

Appendix A

Alternate derivation of RF trap depth

The RF trap depth, derived using physically motivated approximations in §4.2, can also be derived from the properties of the Mathieu equation for small β and q. From [37], the characteristic numbers of the Mathieu equation, $a(q,\beta)$, can be expressed as a series expansion

$$a(q,\beta) = \beta^2 + \frac{1}{2\left(\beta^2-1\right)}q^2 + \mathcal{O}\left(q^4\right) \tag{A.1}$$

Expanding the first two terms for small β, this becomes

$$a \approx -\frac{q^2}{2} + \left(1-\frac{q^2}{2}\right)\beta^2 + \mathcal{O}\left(\beta^4\right) \tag{A.2}$$

Rearranging terms,

$$\beta^2\left(1+\frac{q^2}{2}\right) = a + \frac{q^2}{2} \tag{A.3}$$

If q is small compared to 1 (though not necessarily small compared to a),

$$\beta \approx \sqrt{a+\frac{q^2}{2}} \tag{A.4}$$

Taking the lowest frequency ($n = 0$) component of the ion's oscillation (eqn. 4.14), eqn. A.4 becomes

$$\beta \approx \sqrt{\left(a + \frac{q^2}{2}\right)\frac{\Omega^2}{4}} \tag{A.5}$$

which is the same as equation 4.26. The trapping can therefore be qualitatively understood as simple harmonic motion with frequency ω_0, for small values of β and q.

Appendix B

Determining ion unloading rate

The average unloading rate, $\hat{R}$, is determined by maximizing the following log-likelihood function [2]

$$\mathcal{M}(R) = \log \mathcal{L}(R) = \log \left(\prod_{i=1}^{N} P_i(t_i; R) \right) \tag{B.1}$$

where N is the number of measurements, t_i is a single unloading time measurement and $P_i(t_i, R)$ is the probability that an ion unloads in time t_i given an unloading rate constant R,

$$P_i(t_i; R) = A_i e^{-Rt_i} \tag{B.2}$$

The minimum measurement time $t_{min} = 5$ s, is due to the integration time of the EMCCD. In order to account for this, eqn. B.2 is normalized

$$\int_{t_{min}}^{\infty} P_i(t_i; R) dt_i = 1 \tag{B.3}$$

so that

$$A_i = R e^{Rt_{min}} \tag{B.4}$$

In this case, the log-likelihood function becomes

$$\mathcal{M}(R) = NRt_{min} + N\log R - R\sum_{i=1}^{N} t_i \tag{B.5}$$

The value of R that maximizes eqn. B.5, $\hat{R}$, is easily found by solving $\partial\mathcal{M}/\partial R = 0$, yielding

$$\hat{R} = \left[-t_{min} + \frac{1}{N}\sum_{i=1}^{N} t_i\right]^{-1} \tag{B.6}$$

The errors (68.27% CL) on $\hat{R}$ are found by numerically solving for the values of R that change $\mathcal{M}(R)$ by 0.5 with respect to it's maximum value $\mathcal{M}(\hat{R})$ [2]. This factor of 0.5 is discussed in [2], and is dependent upon the desired CL and number of parameters in P_i. These errors are therefore given by the two solutions for R in the following equation

$$\mathcal{M}(R) = \mathcal{M}(\hat{R}) - 0.5 \tag{B.7}$$

Since $\mathcal{M}(R)$ is log-normal, the upper error on $\hat{R}$ will in general be larger than the lower error.

Bibliography

[1] S. Elliot and P. Vogel, Annu. Rev. Nucl. Part. Sci. **52**, 11551 (2002).

[2] W. Yao *et al.*, J. Phys. G **33**, 1+ (2006).

[3] S. Waldman, *Single ion trapping for the Enriched Xenon Observatory*, PhD thesis, Stanford University, 2005.

[4] S. Huang *et al.*, J. Chem. Phys. **68**, 1355 (1978).

[5] L. Ekström and R. Firestone, WWW table of radioactive isotopes, database version 2/28/99, http://ie.lbl.gov/toi/index.htm.

[6] G. Gioumousis and D. Stevenson, J. Chem. Phys. **29**, 294 (1958).

[7] E. Aprile, R. Mukherjee, and M. Suzuki, Nucl. Instr. Meth. A **302**, 177 (1991).

[8] Super-Kamiokande Collaboration, Y. Ashie *et al.*, Phys. Rev. Lett. **93**, 101801 (2004).

[9] SNO Collaboration, S. N. Ahmed *et al.*, Phys. Rev. Lett. **92**, 181301 (2004).

[10] K. Eguchi *et al.*, Phys. Rev. Lett. **90**, 021802 (2003).

[11] M. Moe, Nucl. Phys. B. (Proc. Suppl.) **19** (1991).

[12] E. Conti *et al.*, Phys. Rev. B **68**, 054201 (2003).

[13] R. Mohapatra and A. Smirnov, Ann. Rev. Nucl. Part. Sci. **56**, 569 (2006).

[14] C. Weinheimer, arXiv:hep-ex, 0210050v2 (2002).

[15] A. Osipowicz *et al.*, hep-ex/0109033 (2001).

[16] U. Seljak, A. Slosar, and P. McDonald, astro-ph/0604335 .

[17] H. Klapdor-Kleingrothaus *et al.*, Eur. Phys. J. A **12** (2001).

[18] D. Caldwell and R. Mohapatra, Phys. Rev. D **48** (1993).

[19] F. Vissani, JHEP **6** (1999).

[20] A. Corney, *Atomic & Laser Spectroscopy* (Oxford University Press, 1978).

[21] G. Janik, W. Nagourney, and H. Dehmelt, J. Opt. Soc. Am. B **2**, 1251 (1985).

[22] H. Metcalf and P. Straten, *Laser Cooling and Trapping* (Springer, 1999).

[23] W. Demtröder, *Laser Spectroscopy, Basic Concepts and Instrumentation*, 3rd ed. (Springer, 2003).

[24] W. Paul and H. Steinwedel, Z. Nat. Tiel A **8**, 448 (1953).

[25] R. Post, University of California Radiation Laboratory Report No. UCRL 2209, 1953 (unpublished).

[26] W. Paul, Rev. Mod. Phys. **62**, 531 (1990).

[27] R. Wuerker, H. Shelton, and R. Langmuir, J. App. Phys. **30**, 342 (1959).

[28] H. Dehmelt, Advan. At. Mol. Phys. **3**, 53 (1967).

[29] W. Neuhauser *et al.*, Phys. Rev. A **22**, 1137 (1980).

[30] D. Wineland *et al.*, Phys. Lett. A **82**, 75 (1981).

[31] M. Nielsen and I. Chuang, *Quantum Computation and Quantum Information* (Cambridge Univ. Press, 2000).

[32] D. Douglas *et al.*, Mass Spectr. Rev. **24**, 1 (2005).

[33] W. Oskay *et al.*, Phys. Rev. Lett. **97**, 020801 (2006).

[34] J. Cirac and P. Zoller, Phys. Rev. Lett. **74**, 4091 (1995).

[35] F. Herfurth *et al.*, Nucl. Instrum. Meth. A **469**, 254 (2001), nucl-ex/0011021.

[36] G. Werth, App. Phys. B **59** (1994).

[37] N. McLachlan, *Theory and Application of Mathieu Functions* (Dover, 1964).

[38] F. G. Major and H. G. Dehmelt, Phys. Rev. **170**, 91 (1968).

[39] R. Blatt, P. Zoller, G. Holzmuller, and I. Siemers, Z. Phys. D. **4**, 121 (1986).

[40] R. Devoe, To be published .

[41] K. Taeman, *Buffer gas cooling of ions in a radiofrequency quadrupole ion gude: A study of the cooling process and cooled beam properties*, PhD thesis, McGill University, 1997.

[42] F. Vedel, J. André, M. Vedel, and G. Brincourt, Phys. Rev. A **27**, 2321 (1983).

[43] P. Dawson, J. Mass Spectrom. Ion Phys. **24** (1977).

[44] F. Londry, R. Alfred, and R. Mach, J. Am. Soc. Mass Spec. **4** (1993).

[45] P. Langevin, Ann. Chim. et Phys. **5** (1905).

[46] E. McDaniel *et al.*, *Ion-Molecule Reactions* (John Wiley & Sons, 1970).

[47] D. Denison, J. Vac. Sci. Tech. **8**, 266 (1971).

[48] E. Badareu, Br. J. Appl. Phys. **15** (1964).

[49] SIMION 7.0, Scientific Instruments Inc.

[50] D. Manura, 2005; http://www.simion.com/info/Collision_Model_HS1.

[51] R. Muller *et al.*, Phys. Rev. Lett. **27**, 532 (1971).

[52] T. Doke, Nucl. Instrum. Meth. **196**, 87 (1982).

[53] Y. Suzuki *et al.*, *The International Workshop on Technique and Application of Xenon Detectors* (World Scientific, 2002).

[54] A. Baldini *et al.*, IEEE Trans. Dielec. Elect. Insul. **13**, 547 (2006).

[55] T. Doke, Port. Phys. **12** (1981).

[56] S. Belogurov *et al.*, Nucl. Instr. Meth. A **452**, 167 (2000).

[57] G. Bressi *et al.*, Nucl. Instr. Meth. A **440**, 254 (2000).

[58] T. Doke *et al.*, Jpn. J. Appl. Phys **41**, 1538 (2002).

[59] T. Takahashi *et al.*, Phys. Rev. A **12**, 1771 (1975).

[60] J. Thomas and D. A. Imel, Phys. Rev. A **36**, 614 (1987).

[61] E. Aprile *et al.*, Phys. Rev. D **72**, 072006 (2005).

[62] J. Jortner, L. Meyer, S. Rice, and E. Wilson, J. Chem. Phys. **42**, 4250 (1965).

[63] E. Morikawa, R. Reininger, P. Gurtler, V. Saile, and P. Laporte, J. Chem. Phys. **91**, 1469 (1989).

[64] A. Hitachi *et al.*, Phys. Rev. B **27**, 5279 (1983).

[65] A. Mozumder, J. Chem. Phys. **12**, 10388 (1994).

[66] S. Kubota *et al.*, Phys. Rev. B **17**, 2762 (1978).

[67] H. Crawford *et al.*, Nucl. Instr. Meth. A **256**, 47 (1987).

[68] U. Fano, Phys. Rev. Lett. **72**, 26 (1947).

[69] M. Redshaw, E. Myers, J. McDaniel, and E. Wingfield, Phys. Rev. Lett. **98** (2007).

[70] K. Ni *et al.*, arXiv:physics/0608034v1 (2006).

[71] O. Bunemann, T. Cranshaw, and J. Harvey, Can. J. Res. A **27** (1949).

[72] D. Imel and J. Thomas, Nucl. Instr. Meth. A **273**, 291 (1988).

[73] E. Aprile *et al.*, Phys. Rev. Lett. **97**, 081302 (2006).